

# 1 **Chemical characterization of long-range transport biomass burning** 2 **emissions to the Himalayas: insights from high-resolution aerosol** 3 **mass spectrometry**

4 **Xinghua Zhang<sup>1,2,3</sup>, Jianzhong Xu<sup>1</sup>, Shichang Kang<sup>1</sup>, Yanmei Liu<sup>1,3</sup>, Qi Zhang<sup>4</sup>**

5 <sup>1</sup>State Key Laboratory of Cryospheric Sciences, Northwest Institute of Eco-Environment and  
6 Resources, Chinese Academy of Sciences, Lanzhou 730000, China

7 <sup>2</sup>Key Laboratory of Arid Climatic Change and Reducing Disaster of Gansu Province, Key  
8 Laboratory of Arid Climatic Change and Disaster Reduction of CMA, Institute of Arid  
9 Meteorology, China Meteorological Administration, Lanzhou 730020, China

10 <sup>3</sup>University of Chinese Academy of Sciences, Beijing 100049, China

11 <sup>4</sup>Department of Environmental Toxicology, University of California, Davis, CA 95616, USA

12 *Correspondence to:* Jianzhong Xu (jzxu@lzb.ac.cn)

## 13 **Abstract**

14 An intensive field measurement was conducted at a remote, background, and high-altitude site  
15 (Qomolangma station, QOMS, 4276 m a.s.l.) in the northern Himalayas, using an Aerodyne high-  
16 resolution time-of-flight aerosol mass spectrometer (HR-ToF-AMS) along with other collocated  
17 instruments. The field measurement was performed from April 12 to May 12, 2016 to chemically  
18 characterize the high time-resolved submicron particulate matter (PM<sub>1</sub>) and obtain the dynamic  
19 processes (emissions, transport, and chemical evolution) of biomass burning (BB), frequently  
20 transported from South Asia to the Himalayas during pre-monsoon season. Overall, the average ( $\pm$   
21  $1\sigma$ ) PM<sub>1</sub> mass concentration was 4.44 ( $\pm$ 4.54)  $\mu\text{g m}^{-3}$  for the entire study, comparable with those  
22 observed at other remote sites worldwide. Organic aerosol (OA) was the dominant PM<sub>1</sub> species  
23 (accounting for 54.3% of total PM<sub>1</sub> on average) followed by black carbon (BC) (25.0%), sulfate  
24 (9.3%), ammonium (5.8%), nitrate (5.1%), and chloride (0.4%). The average size distributions of  
25 PM<sub>1</sub> species all peaked at an overlapping accumulation mode ( $\sim$  500 nm), suggesting that aerosol  
26 particles were internally well-mixed and aged during long-range transport. Positive matrix  
27 factorization (PMF) analysis on the high-resolution organic mass spectra identified three distinct  
28 OA factors, including a BB-related OA (BBOA, 43.7%), a nitrogen-containing OA (NOA, 13.9%)  
29 and a more-oxidized oxygenated OA (MO-OOA, 42.4%). Two polluted episodes with enhanced  
30 PM<sub>1</sub> mass loadings and elevated BBOA contributions from the west and southwest of QOMS  
31 during the study were observed. A typical BB plume was investigated in detail to illustrate the  
32 chemical evolution of aerosol characteristics under distinct air mass origins, meteorological  
33 conditions and atmospheric oxidation processes.

## 34 **1 Introduction**

35 The Tibetan Plateau and Himalayas (TPH), generally called the “third pole”, is the highest  
36 (average altitude of more than 4000 m a.s.l.) and largest ( $\sim$  2 500 000 km<sup>2</sup>) plateau in the world.  
37 This region has been recognized as one of the most pristine region in the world due to its high  
38 altitude, sparse population and minor influence of anthropogenic activities (Yao et al., 2012a).

39 Consideration on the intense dynamical and thermal forcing effects, the TPH not only plays a key  
40 role in the formation of Asian monsoon systems, but also impacts the large-scale atmospheric  
41 circulation, hydrological cycle, as well as global climate (Duan and Wu, 2005; Wu et al., 2007).  
42 Over the past decades, more attentions have been paid to the environment and climate change in  
43 the TPH since this region is very susceptibility to the global climate change such as fast air  
44 temperature rise and dramatic glacier shrinkage (Xu et al., 2009; Kang et al., 2010; Yao et al.,  
45 2012b; Yang et al., 2014). Atmospheric environment in the TPH, albeit which is one of the most  
46 pristine region in the world, has been thought to be influenced variably due to the worse air  
47 pollution in its surrounding countries (Hou et al., 2003; Lau et al., 2008). For example, polluted air  
48 mass, particularly from South and Southeast Asia regions, had been observed frequently to  
49 transport to the Himalayas (Bonasoni et al., 2010; Cong et al., 2015), heat the aloft air masses over  
50 the TPH (Lau et al., 2006; Ramanathan and Carmichael, 2008) and decline the surface albedo after  
51 its deposition onto snow and glacier (Xu et al., 2009). As a consequence, characterizing the  
52 aerosol physicochemical properties in the TPH, including mass loading, chemical composition,  
53 size distribution and source, are of great importance to better understand the aerosol chemistry,  
54 estimate the aerosol radiative forcing, and finally evaluate the effect of polluted air mass on the  
55 ecology and environment in the TPH region.

56 Numerous aerosol measurements have been conducted in the TPH region in past decades to  
57 characterize the physicochemical properties, sources and transport pathways of ambient aerosol  
58 (Liu et al., 2008; Decesari et al., 2010; Marcq et al., 2010; Marinoni et al., 2013; Putero et al.,  
59 2014; Xu et al., 2017; Zhang et al., 2017a). South and Southeast Asia are two major **polluted**  
60 regions due to their intense biomass burning (BB) activities from natural forest fires and  
61 traditional human burning activities for residential heating and cooking (Engling et al., 2011;  
62 Yadav et al., 2017). The polluted feature of South and Southeast Asia during April 12 to May 12,  
63 2016 can be further revealed by the distribution of average aerosol optical depth in Fig. 1. During  
64 the pre-monsoon period, atmospheric pollutants associated with BB emissions in South Asia are  
65 generally advected by regional and long-range transport (e.g., westerlies and South Asian  
66 monsoon system) to Himalayas and built up in the southern foothills, then pollutants are lifted up  
67 to high altitude by the Himalayan topography and the typical valley wind circulation (Zhao et al.,  
68 2013; Cong et al., 2015; Liu et al., 2017). However, the chemical properties of aerosol particles  
69 are still not well understood and limited in the Himalayas region due to its remote and harsh  
70 environments, challenging weather conditions and logistic difficulties. In addition, most of the  
71 available studies are mainly based on the off-line filter sampling of ambient aerosol or snow/ice  
72 samples following by laboratory analyses (Decesari et al., 2010; Ram et al., 2010; Li et al., 2016;  
73 Wan et al., 2017). These studies usually had a relatively low-time resolution (days to weeks).  
74 Therefore, real-time consecutive field measurement, especially focusing on the high-resolution  
75 size-resolved chemical characteristics of aerosol particles, is of great importance and necessary to  
76 give insight into the sources and the dynamic chemical evolution of ambient aerosol.

77 Online real-time instrument such as Aerodyne aerosol mass spectrometer (AMS), which can  
78 be used to characterize the chemical properties and sources of submicron aerosol particles with  
79 high time resolution and sensitivity, has been greatly developed and widely implemented  
80 worldwide (Canagaratna et al., 2007; Zhang et al., 2007a; Jimenez et al., 2009; Li et al., 2017).  
81 Although the deployments of the AMS in China have started since 2006, most of these studies in

82 China are conducted in urban areas, including Beijing–Tianjin–Hebei (Sun et al., 2013; Sun et al.,  
83 2016), Yangtze River Delta (Wang et al., 2016a; Wang et al., 2016b), Pearl River Delta regions  
84 (Huang et al., 2011), and Lanzhou (Xu et al., 2014; Xu et al., 2016; Zhang et al., 2017b) as shown  
85 in Fig. S1, whereas just few studies deployed in remote sites so far, such as Menyuan (Du et al.,  
86 2015), Mt. Yulong (Zheng et al., 2017), and Nam Co (Xu et al., 2017; Wang et al., 2017). In this  
87 paper, an Aerodyne high-resolution time-of-flight mass spectrometer (HR-ToF-AMS) was  
88 deployed at the Qomolangma Station for Atmospheric and Environmental Observation and  
89 Research (QOMS) in the north slope of the Himalayas to fill the vacancy of real-time mass  
90 spectrometer measurement at high elevation site and evaluate the significant impacts of BBs from  
91 polluted areas in the South Asia on the TPH aerosol properties during the pre-monsoon season.  
92 Here, we report an overview of the 5-min real-time chemical and physical characteristics of  
93 submicron aerosols ( $PM_{10}$ ), including mass loading, composition, size distribution, acidity as well  
94 as temporal and diurnal variations. The sources of organic aerosols (OA) are also investigated  
95 using positive matrix factorization analysis on the high-resolution OA mass spectrum. BB  
96 influence and chemical evolution of aerosols in polluted plume are examined via combining back  
97 trajectory analysis of air masses and fire hotspots information, respectively.

## 98 **2 Experimental methods**

### 99 **2.1 Sampling site**

100 The QOMS (28.36°N, 86.95°E, 4276 m a.s.l.; Fig. 1), which is located in the northern slope of  
101 Mt. Everest (~ 30 km away), was established for atmospheric and environmental observation since  
102 2005 (Ma et al., 2008). The geomorphic and climate features around the QOMS are typical alpine  
103 cold and arid areas covered by sandy soil with sparse vegetation. The QOMS is located in a long  
104 river valley and isolated from residential areas due to its harsh environment with a small village  
105 (with a population of ~ 300) to the south (~ 10 km). The closest town, Dingri County, is ~ 100 km  
106 south from the QOMS. A freeway is located at the front of the QOMS for tourism with increased  
107 tourist during summer. The measurements were conducted from April 12 to May 12, 2016. Since  
108 this period was within the typical pre-monsoon season of the TPH, the large-scale atmospheric  
109 circulation pattern was dominated by westerly or southwesterly winds with limited precipitation.  
110 Owing to a distinct thermal forcing from the southern mountains and glaciers, the QOMS was  
111 locally dominated by strongly mountain-valley circulation with down-slope wind prevailing  
112 during the daytime, especially in the afternoon (Fig. 1c and S2) (Zou et al., 2008), which would  
113 make the valley as an efficient channel for the down transport of air mass from high-altitude  
114 troposphere.

### 115 **2.2 Instrumentation**

116 A suite of real-time instruments were co-located to measure the physiochemical properties of fine  
117 particles at the QOMS, including an Aerodyne HR-ToF-AMS (Aerodyne Research Inc., Billerica,  
118 MA, USA) for 5-min size-resolved chemical compositions (organics, sulfate, nitrate, ammonium,  
119 and chloride) of non-refractory submicron particulate matter (NR- $PM_{10}$ ), a scanning mobility  
120 particle sizer (SMPS, model 3936, TSI Inc., Shoreview, MN, USA) for 5-min particle number  
121 concentration and size distribution between 14.6 and 661.2 nm in mobility diameter ( $D_m$ ), and a  
122 photoacoustic extinctionsimeter (PAX, DMT Inc., Boulder, CO, USA) for particle light absorption

123 and scattering coefficient ( $b_{\text{abs}}$  and  $b_{\text{scat}}$ ) at 405 nm and further deriving black carbon (BC) mass  
124 concentration. All instruments were placed in an air-conditioned room with temperature  
125 maintaining at  $\sim 20$  °C. Ambient aerosol particles were introduced through a 0.5 inch copper tube  
126 which stemmed out of the rooftop by about 1.5 m. A  $\text{PM}_{2.5}$  cyclone (model URG-2000-30EH,  
127 URG Corp., Chapel Hill, NC, USA) was used in front of the sampling inlet for removing coarse  
128 particles with size cutoffs of 2.5  $\mu\text{m}$  in aerodynamic diameter ( $D_{\text{va}}$ ). A diffusion dryer was placed  
129 following the cyclone to dry the ambient air and eliminate potential humidity effect on particles.  
130 The total length of the sampling line was about 5 m and the retention time of particles was less  
131 than 2.5 s in the whole inlet. The total air flow rate from the sampling inlet was about  $10 \text{ L min}^{-1}$ ,  
132 with part of flow shared by the HR-ToF-AMS and the SMPS while the remaining flow exhausted  
133 by an external pump. The meteorology data including wind speed (WS), wind direction (WD),  
134 relative humidity (RH), temperature ( $T$ ), and solar radiation (SR) during this study were obtained  
135 from a Vantage Pro2 weather station (Davis Instruments Corp., Hayward, CA, USA). Note that all  
136 the date and time used in this study are reported in Beijing Time (BJT: UTC + 8 h).

## 137 **2.3 HR-ToF-AMS operation and data analysis**

### 138 **2.3.1 HR-ToF-AMS operation**

139 A detailed instrumental description of the Aerodyne HR-ToF-AMS can be found elsewhere  
140 (DeCarlo et al., 2006) and only a brief summary is provided here. Briefly, the HR-ToF-AMS  
141 consists of three main parts: an aerosol sampling inlet, a particle sizing vacuum chamber, and a  
142 particle composition detection section (Jimenez et al., 2003). Ambient particles are sampled into  
143 the instrument through a critical orifice (130  $\mu\text{m}$  in this study for enhancing the transmission  
144 efficiency at the high-altitude area) and focus into a concentrated and narrow beam through an  
145 aerodynamic lens. Then particles are accelerated into the sizing vacuum chamber and obtain  
146 different velocities for particles with different sizes due to the supersonic expansion induced by  
147 different pressure between the two chambers. Meanwhile, a mechanical chopper with two radial  
148 slits located  $180^\circ$  apart is used to intercept the focused particle, and then the time of flight (P-ToF)  
149 from the chopper to the vaporizer is measured to obtain the aerodynamic size of particles. After  
150 passing through the sizing chamber, particles are directed onto a resistively heated surface ( $\sim$   
151  $600$  °C) under a high vacuum and ionized by a 70 eV electron impact, and finally detect by the  
152 high-resolution time-of-flight mass spectrometer. In this study, the HR-ToF-AMS was only  
153 toggled under the high sensitive V-mode (detection limits  $\sim 10 \text{ ng m}^{-3}$ ). Under the V-mode  
154 operation, the instrument also switched between the mass spectrum (MS) mode and the particle P-  
155 ToF mode every 15 s, spending 6 and 9 s on each, to obtain the mass concentrations and size  
156 distributions of the non-refractory species, respectively.

157 The HR-ToF-AMS was calibrated for ionization efficiency (IE) and particle sizing at the  
158 beginning, in the middle, and at the end of this study according to the standard protocols (Jayne et  
159 al., 2000). Both the calibrations of IE and particle sizing were performed using mono-dispersed  
160 ammonium nitrate particles with nominal diameters of 70–300 nm. Default relative ionization  
161 efficiency (RIE) values were assumed in this study as 1.1 for nitrate, 1.3 for chloride, and 1.4 for  
162 organics. The RIE values of 3.9 and 4.2 were used for ammonium based on the results of two IE  
163 calibrations at the beginning and in the middle of this study, while RIE values of 1.6 and 1.4 were  
164 determined similarly for sulfate by using mono-dispersed ammonium sulfate particles,

165 respectively.

### 166 **2.3.2 HR-ToF-AMS data analysis**

167 The mass concentrations and size distributions of NR-PM<sub>1</sub> species and the ion-speciated mass  
168 spectra, composition and elemental composition of organics were determined from the HR-ToF-  
169 AMS data by using the standard ToF-AMS analysis toolkit SQUIRREL (v1.56) and PIKA (v1.15c)  
170 modules written in Igor Pro (Wavemetrics Inc., Lake Oswego, OR, USA). An empirical particle  
171 collection efficiency (CE) of 0.5 was used to compensate for the incomplete transmission and  
172 detection of particles due to particle bouncing at the vaporizer and partial transmission through the  
173 aerodynamic lens, which has been widely used in field studies employing AMS with a dryer  
174 installed in front of the inlet (Xu et al., 2014; Xu et al., 2016). The elemental ratios of oxygen-to-  
175 carbon (O/C), hydrogen-to-carbon (H/C), nitrogen-to-carbon (N/C), and organic mass-to-organic  
176 carbon (OM/OC) for this study were determined using the “improved-ambient” method (referred  
177 as I-A method) (Canagaratna et al., 2015), which increased O/C on average by 34%, H/C on  
178 average by 15%, and OM/OC on average by 17% (Fig. S3) compared with those determined from  
179 the “Aiken ambient” method (referred as A-A method) (Aiken et al., 2008).

180 Positive matrix factorization (PMF) analysis using the PMF2.exe algorithm (v4.2) (Paatero  
181 and Tapper, 1994) in robust mode was conducted on the high resolution mass spectra (HRMS) to  
182 determine distinct OA components in this study. The analysis was performed using an Igor Pro-  
183 based PMF Evaluation Tool (PET, v2.03) (Ulbrich et al., 2009), downloaded from the webpage  
184 ([http://cires.colorado.edu/jimenez-group/wiki/index.php/PMF-AMS\\_Analysis\\_Guide](http://cires.colorado.edu/jimenez-group/wiki/index.php/PMF-AMS_Analysis_Guide)). The data  
185 and error matrices input into the PMF analysis were generated from analyzing the V-mode data via  
186 PIKA fitting. Detailed PMF analysis was thoroughly evaluated following the procedures  
187 summarized in Table 1 of Zhang et al. (2011). Isotopic ions were generally excluded and the four  
188 ions of O<sup>+</sup>, HO<sup>+</sup>, H<sub>2</sub>O<sup>+</sup>, and CO<sup>+</sup> were downweighted in PMF analysis, because they were  
189 determined according to the relationship with CO<sub>2</sub><sup>+</sup> signal (Ulbrich et al., 2009). The “bad” ions  
190 with *S/N* less than 0.2 were removed from the HRMS data and error matrices before PMF analysis,  
191 and “weak” ions with *S/N* between 0.2 and 2 were downweighted by increasing their errors. In  
192 addition, some runs with huge mass loading spikes were also removed from the data and error  
193 matrices. The detailed matrix preparation and data pretreatment can also refer to Xu et al. (2014).

194 A summary of key diagnostic plots of the PMF results for this study is presented in Fig. S4.  
195 Overall, the PMF solutions were investigated for 1 to 8 factors and for the rotational parameter  
196 (fPeak) varying from -1 to 1 with a step of 0.1. Besides examining the model residuals, scaled  
197 residuals, and the Q/Q<sub>exp</sub> contributions for each *m/z* and time following procedures detailed in  
198 Table 1 of Zhang et al. (2011), the optimum solution can also be evaluated via comparing the mass  
199 spectra of individual factors with reference spectra from specific sources or other ambient AMS  
200 measurements, comparing the time series of individual factors with the known external tracers,  
201 and analyzing the diurnal variations of individual factors. Finally, the 3-factor solution with fPeak  
202 = 0 was chosen in this work. The direct comparisons of the mass spectra, time series, and diurnal  
203 variations for 2-factor and 4-factor solution were also shown in Fig. S5 and S6, respectively. The  
204 2-factor solution does not resolve the small, yet distinct nitrogen-containing OA, while the 4-  
205 factor solution shows a splitting factor from the BB OA resolved in the 3-factor solution and  
206 seems just like a simple separation of the two BB polluted episodes.

## 207 **2.4 Other relevant data**

208 The Hybrid Single Particle Lagrangian Integrated Trajectory (HYSPLIT4) model developed by  
209 the National Oceanic and Atmospheric Administration (NOAA) (Draxler and Rolph, 2003) was  
210 used to investigate the origins of air masses in this study, using the meteorological data from the  
211 NOAA Global Data Assimilation System (GDAS). The back trajectories were calculated every 6 h  
212 at an ending height of 500 m above ground level at the QOMS during the entire campaign, and  
213 then clustered them according to their similarity in spatial distribution. Finally, a four-cluster  
214 solution was adopted according to its small total spatial variance.

215 Aerosol optical depth (AOD) at 550 nm was derived from the observations made by National  
216 Aeronautics and Space Administration (NASA) Moderate Resolution Imaging Spectroradiometer  
217 (MODIS) onboard the Terra satellite. The distribution of average aerosol optical depth (AOD) in a  
218 large range areas (20 °–45 °N, 60 °–110 °E) around the TPH during the entire period of this study is  
219 given in Fig. 1d.

220 Various active fire hotspots were detected over South and Southeast Asia by the Fire  
221 Information for Resource Management System (FIRMS) provided by MODIS satellite  
222 (<https://firms.modaps.eosdis.nasa.gov>), demonstrating the possibility that active wildfires or BBs  
223 from South and Southeast Asia may have significant impacts on the air conditions in the TPH  
224 region.

225 The aerosol liquid water content (ALWC) was estimated with the Extended AIM (E-AIM)  
226 Aerosol Thermodynamics Model (<http://www.aim.env.uea.ac.uk/aim/aim.php>). The input data  
227 included the concentrations of sulfate, nitrate, ammonium, and chloride measured by the HR-ToF-  
228 AMS as well as the relative humidity (RH) and temperature of ambient air.

## 229 **3 Results and discussion**

### 230 **3.1 Overview of the study**

#### 231 **3.1.1 Meteorological conditions**

232 The measurement period in our study was within the typical pre-monsoon season of the TPH. The  
233 meteorological conditions were therefore characterized by a relatively cold, dry and windy  
234 weather, and the westerlies dominated the large-scale atmospheric circulation patterns with little  
235 precipitation, as displayed in Fig. 2. During the study, the averaged diurnal air temperature ranged  
236 from  $-2.0$  to  $12.5$  °C with an average ( $\pm 1\sigma$ ) of  $5.7$  ( $\pm 5.0$ ) °C, and the RH ranged from 15.3 to  
237 67.5% with an average of  $39.8 \pm 18.8\%$ . Only two light precipitation events (1 and 0.5 mm  $d^{-1}$ )  
238 occurred on 1 and 8 May, respectively. The WDs at QOMS were predominantly by southwesterly,  
239 which were mainly associated with the thermally driven mountain-valley winds and glacier winds  
240 (Zou et al., 2008). For the diurnal variation of wind conditions, a nearly calm wind period (hourly  
241 average WS less than  $2$  m  $s^{-1}$ ) was observed in the early morning time; after sunrise to noon time,  
242 there was a weak up-slope wind period (from the north); the diurnal wind cycles in the rest time  
243 were dominated by the down-slope wind (from the southwest) with the maximum value of hourly  
244 average WS up to  $7$  m  $s^{-1}$  (Fig. 2b and S2).

#### 245 **3.1.2 Inter-comparisons between different instruments**

246 An inter-comparison of the total PM<sub>1</sub> (NR-PM<sub>1</sub> + BC) mass concentrations measured by the HR-  
247 ToF-AMS (CE = 0.5) and the PAX with particle volumes (assuming spherical particles)  
248 determined from the SMPS is shown in Fig. S7. Overall, the PM<sub>1</sub> mass is closely correlated ( $R^2 =$   
249 0.97) with that of SMPS particle volume during the entire campaign, with a linear regression slope  
250 of 2.86. This slope is significantly higher than the estimated average PM<sub>1</sub> density of 1.44 g cm<sup>-3</sup>,  
251 which is calculated based on the measured particle compositions in this study and the assumed  
252 particle densities of 1.2 for organics, 1.78 for (NH<sub>4</sub>)<sub>2</sub>SO<sub>4</sub>, 1.72 for NH<sub>4</sub>NO<sub>3</sub>, 1.52 for NH<sub>4</sub>Cl and  
253 1.8 g cm<sup>-3</sup> for BC (Zhang et al., 2005b; Xu et al., 2016). This discrepancy is likely introduced by  
254 various factors, including different transmission sizes between HR-ToF-AMS and SMPS (up to ~  
255 1.0 μm in  $D_{va}$  for AMS vs. limited size range of 14.6–661.2 nm in  $D_m$  for SMPS), rough  
256 calculation of PM<sub>1</sub> density using assumed composition densities and spherical shape without  
257 consideration the particle porosity, as well as the using of empirical and constant CE value of 0.5  
258 in this study. This phenomenon was also observed at other sites in previous studies (Ge et al., 2012;  
259 Huang et al., 2012; Xu et al., 2014; Du et al., 2015).

### 260 3.1.3 Mass concentration and chemical composition of PM<sub>1</sub>

261 As shown in Fig. 2, the mass concentrations of PM<sub>1</sub> and all PM<sub>1</sub> species, as well as their mass  
262 fractions in PM<sub>1</sub> varied dynamically throughout this study. Two polluted periods (PP1 and PP2)  
263 were identified according to their high PM<sub>1</sub> mass concentrations (daily average PM<sub>1</sub> mass is larger  
264 than 5 μg m<sup>-3</sup>), high contributions from BBOA and unique back trajectories. The rest periods  
265 characterized by low PM<sub>1</sub> mass concentrations were considered as clear periods (CP1 and CP2).  
266 The 5-min total PM<sub>1</sub> mass concentration ranged from 0.18 to 27.97 μg m<sup>-3</sup> for the study, with an  
267 average ( $\pm 1\sigma$ ) value of 4.44 ± 4.54 μg m<sup>-3</sup>. This average value was more than two times lower  
268 than most of the PM<sub>1</sub> mass concentrations measured with Aerodyne AMS or aerosol chemical  
269 speciation monitor (ACSM) instruments at various urban, suburban, rural or background sites in  
270 China (10.9–138.8 μg m<sup>-3</sup>) (Fig. S1), except slightly lower than that at Mt. Yulong (5.7 μg m<sup>-3</sup>)  
271 located at the southeastern edge of the TPH, whereas higher than that at Nam Co Station (2.0 μg  
272 m<sup>-3</sup>) located in the central of the TPH. Moreover, as shown in table S1, the PM<sub>1</sub> mass  
273 concentration in this study was also lower than those measured at the three remote island sites in  
274 Asia which were frequently influenced by outflow from China, Korea and Japan (i.e., 7.9 μg m<sup>-3</sup>  
275 for Okinawa island, 12.0 μg m<sup>-3</sup> for Fukue island in Japan, and 10.7 μg m<sup>-3</sup> for Jeju island in  
276 Korea) (Takami et al., 2005; Jimenez et al., 2009), as well as the PM<sub>1</sub> mass concentration (15.1 μg  
277 m<sup>-3</sup>) obtained at the Bachelor mountain in United States which was heavily impacted by wildfire  
278 smoke plumes (Zhou et al., 2017). However, it was higher than those reported at other coastal,  
279 high elevation, forest or remote background sites in North America and Europe (0.55–2.91 μg m<sup>-3</sup>)  
280 (Zhang et al., 2007a; Sun et al., 2009; Fröhlich et al., 2015). Although these measurements  
281 mentioned above were conducted at various sites worldwide during different seasons, these  
282 comparisons further demonstrate that QOMS is a typical high elevation and remote background  
283 site in Asia.

284 Overall, organics and BC were the two dominant PM<sub>1</sub> species (averagely contributed 54.3%  
285 and 25.0% to the total PM<sub>1</sub> mass, respectively) followed by sulfate (9.3%), ammonium (5.8%),  
286 nitrate (5.1%), and chloride (0.4%) (Fig. 3a). The high contributions of organics and BC at QOMS  
287 were significantly associated with the active BB emissions by long-range transport from polluted

288 areas in South Asia. Organic compounds and BC have been revealed as two dominant components  
289 of BB aerosols and generally used to identify BB events in previous studies (Bond et al., 2004;  
290 Bougiatioti et al., 2014). In addition, biomass burning at high elevation regions of Himalayas and  
291 south Asia was more incomplete burning and could emit amount of BC. This conclusion can be  
292 further revealed by their enhanced mass concentrations and contributions, especially for organics,  
293 during the two distinct polluted episodes influenced by active BB plumes. Figure 3b showed the  
294 mass contributions of PM<sub>1</sub> species as a function of total PM<sub>1</sub> mass concentrations. The PM<sub>1</sub> mass  
295 loadings in this study were mostly below 6 μg m<sup>-3</sup> (accounted for ~ 77%); The mass contribution  
296 of organics increased significantly with the increase of total PM<sub>1</sub> mass loading whereas the rest  
297 species showed relatively stable or decrease trends, suggesting the dominant contributions of  
298 organics in the polluted episodes at QOMS.

### 299 **3.1.4 Acidity and size distributions of submicron aerosols**

300 To evaluate the bulk acidity of NR-PM<sub>1</sub> in this study, we calculated the NH<sub>4</sub><sup>+</sup> concentration  
301 (NH<sub>4</sub><sup>+</sup><sub>calc</sub>) based on the mass concentrations of sulfate, nitrate and chloride measured by the HR-  
302 ToF-AMS and assumed full neutralization of these anions by ammonium (Zhang et al., 2007b).  
303 The scatter plot of the measured NH<sub>4</sub><sup>+</sup> (NH<sub>4</sub><sup>+</sup><sub>meas</sub>) concentration versus the NH<sub>4</sub><sup>+</sup><sub>calc</sub> concentration  
304 for the entire campaign was shown in Fig. S7. A tight correlation ( $R^2 = 0.97$ ) existed between  
305 NH<sub>4</sub><sup>+</sup><sub>meas</sub> and NH<sub>4</sub><sup>+</sup><sub>calc</sub> with a linear regression slope of 1.2, indicating that there were excess of  
306 ammonium in the submicron particle. This slightly high NH<sub>4</sub><sup>+</sup><sub>meas</sub>/NH<sub>4</sub><sup>+</sup><sub>calc</sub> ratio was quite different  
307 with those results from various urban and rural sites in China, where bulk aerosols were overall  
308 neutralized or acidic due to the enrich gaseous precursors of SO<sub>2</sub> and NO<sub>x</sub> that could be further  
309 oxidized to sulfate and nitrate (Sun et al., 2013; Xu et al., 2014; Du et al., 2015; Zhang et al.,  
310 2017b). The excess ammonium at QOMS might relate to the important contributions of organic  
311 acids in this area (Cong et al., 2015), which could underestimate the NH<sub>4</sub><sup>+</sup><sub>calc</sub> due to the neglect of  
312 organic acids in the ion-balance calculation, and the non-negligible contributions of nitrogen-  
313 containing organic compounds to NH<sub>x</sub><sup>+</sup> which finally overestimated the NH<sub>4</sub><sup>+</sup><sub>meas</sub> (Sun et al., 2009;  
314 Ge et al., 2012). As mentioned above, atmospheric aerosols in the TPH region were significantly  
315 influenced by BB emissions from South Asia during the sampling periods. BBs would emit large  
316 amounts of nitrogen-containing organic compounds (Fleming et al., 2017; Zhou et al., 2017) and  
317 as discussed in section 3.2.

318 Figure 4 shows the average size distributions of NR-PM<sub>1</sub> species and their mass contributions  
319 as the function of size distribution. Overall, all chemical species showed a nearly consistent but  
320 narrow accumulation mode peaking at ~ 500 nm in  $D_{va}$ , indicating the well internal-mixed and  
321 aged aerosol particles at QOMS. Ultrafine particles (particles with diameter less than 100 nm)  
322 were dominated by organics (more than 70%), while the mass contributions of chemical species at  
323 the major peak (~ 500 nm) were organics (~ 65%), sulfate (~ 13%), nitrate (~ 11%), ammonium  
324 (~ 10%), and chloride (~ 1%). The contribution of organics decreased with the increase of size  
325 mode, while the contributions of three major inorganic species (sulfate, nitrate and ammonium)  
326 slightly increased with the increasing sizes (Fig. 4b).

### 327 **3.1.5 Diurnal variations of chemical species**

328 The average diurnal cycles of meteorological parameters as well as the PM<sub>1</sub> species and their mass  
329 fractions for the entire campaign were shown in Fig. 5. All PM<sub>1</sub> species presented a similar diurnal



330 pattern with lower concentrations in the daytime whereas higher concentrations in the nighttime.  
331 The mass concentrations reached the minimum values at around 15:00. This pattern was  
332 accompanied with the enhanced wind speed and the increased air temperature in the afternoon  
333 which could related with the dynamics of planetary boundary layer (PBL). After that, the mass  
334 concentrations began to build up and reached to high levels in the nighttime. Note that the mass  
335 concentrations of chloride and BC also existed a slight peak during the early morning, which  
336 corresponded with the calm wind conditions and the lowest air temperature of the day and could  
337 associated with the enhanced local emissions at QOMS in the morning. The diurnal cycles of mass  
338 contributions of each PM<sub>1</sub> species were relatively stable for the entire campaign, besides the slight  
339 increase of BC from 24% at ~ 08:00 to 30% at ~ 10:00. Overall, organics dominated PM<sub>1</sub>  
340 throughout the day (49–57%), followed by BC (23–30%), sulfate (9–10%), ammonium (5–6%),  
341 nitrate (4–6%), and chloride (0.3–0.8%).

### 342 3.2 Bulk characteristics of OA

343 Figure 6a and b showed the average mass contributions of the four elements and the six ion  
344 categories to total organics, respectively. The organic mass was on average composed of 36.8%  
345 carbon, 57.9% oxygen, 4.0% hydrogen, and 1.3% nitrogen. For ionic categories, C<sub>x</sub>H<sub>y</sub>O<sub>1</sub><sup>+</sup> ions  
346 dominated the total OA accounting for 41.3%, followed by C<sub>x</sub>H<sub>y</sub>O<sub>2</sub><sup>+</sup> (24.9%), C<sub>x</sub>H<sub>y</sub><sup>+</sup> (23.9%),  
347 H<sub>y</sub>O<sub>1</sub><sup>+</sup> (6.1%), C<sub>x</sub>H<sub>y</sub>N<sub>p</sub><sup>+</sup> (2.9%) and C<sub>x</sub>H<sub>y</sub>O<sub>z</sub>N<sub>p</sub><sup>+</sup> (0.9%). The contributions of oxygen and the two  
348 major oxygenated ion fragments (C<sub>x</sub>H<sub>y</sub>O<sub>z</sub><sup>+</sup> = C<sub>x</sub>H<sub>y</sub>O<sub>1</sub><sup>+</sup>+C<sub>x</sub>H<sub>y</sub>O<sub>2</sub><sup>+</sup>) at QOMS were quite higher than  
349 those obtained at other urban or rural sites in China, whereas carbon and C<sub>x</sub>H<sub>y</sub><sup>+</sup> ions had relative  
350 lower contributions, e.g., 38% of C<sub>x</sub>H<sub>y</sub>O<sub>z</sub><sup>+</sup> and 21% of oxygen versus 56% of C<sub>x</sub>H<sub>y</sub><sup>+</sup> and 70% of  
351 carbon in urban Lanzhou (Xu et al., 2014), and 37.4% of C<sub>x</sub>H<sub>y</sub>O<sub>z</sub><sup>+</sup> versus 51.2% of C<sub>x</sub>H<sub>y</sub><sup>+</sup> in urban  
352 Nanjing (Wang et al., 2016a), suggesting that OA at QOMS were highly aged. Correspondingly,  
353 the average high-resolution OA mass spectrum (Fig. 6c) also showed significantly high  
354 contribution (~ 25%) at *m/z* 44 signal (one of the most reliable marker of oxygenated OA)  
355 compared with other ion fragments, e.g., 5% at *m/z* 43 (indicator for less oxidized compounds),  
356 1.7% at *m/z* 55 (important COA fragment), and 0.4% at *m/z* 57 (tracer for traffic-related emission)  
357 (Alfarra et al., 2004; Zhang et al., 2005a). The average O/C ratio was 1.07 during this study, which  
358 was much higher than those observed at various urban and rural sites in China using the I-A  
359 method, e.g., 0.37 in Beijing (Sun et al., 2016), 0.36 in Lanzhou (Xu et al., 2016), 0.35 in Nanjing  
360 (Wang et al., 2016a), and 0.65 in Ziyang (Hu et al., 2016)). Moreover, the average O/C ratio was  
361 even higher than that of 0.98 at the background site of Mt. Wuzhi in southern China (Zhu et al.,  
362 2016), indicating that OA at QOMS was more oxidized and aged during long-range transport. The  
363 average H/C, N/C and OM/OC ratios were on average 1.29, 0.026 and 2.55 in this study,  
364 determined a nominal chemical formula of OA as C<sub>1</sub>H<sub>1.29</sub>O<sub>1.07</sub>N<sub>0.026</sub>.

365 For the diurnal cycles, O/C ratio had two peaks in the early morning and late afternoon, likely  
366 related to the production of secondary organic aerosol (SOA) via aqueous-phase reactions or  
367 photochemical oxidation processes during these two periods. H/C and N/C ratios yet showed  
368 inverse diurnal cycles with that of O/C, namely peaked at around 08:00–10:00 in the morning.  
369 The Van Krevelen diagram (H/C versus O/C), which had been used widely to probe the oxidation  
370 reaction mechanisms for bulk OA (Heald et al., 2010), showed an apparent anticorrelation ( $R^2 =$   
371 0.57) with a slope of –0.48 at QOMS (Fig. S8). Ng et al. (2011b) have suggested that a slope of –

372 0.5 indicate a net change in chemical composition from the addition of both acid and  
373 alcohol/peroxide functional groups without fragmentation, and/or carboxylic acid groups with  
374 fragmentation.

### 375 **3.3 Organic aerosol source apportionment**

376 Source apportionment via PMF analysis on the high-resolution OA mass spectrum identified three  
377 distinct factors in this campaign according to their unique temporary variations, mass spectrum  
378 (MS) profiles, element ratios, correlations with tracers, and diurnal patterns, i.e., a BB-related OA  
379 (BBOA), a nitrogen-containing OA (NOA) and a more-oxidized oxygenated OA (MO-OOA).  
380 Detailed discussion on each factor is given in the following subsections.

#### 381 **3.3.1 BBOA**

382 Although significant high contribution at  $m/z$  44 (mostly  $\text{CO}_2^+$ ) was found in all of the three OA  
383 components, the BBOA MS was also characterized by contributions at  $m/z$  60 (mainly  $\text{C}_2\text{H}_4\text{O}_2^+$ )  
384 and tiny  $m/z$  73 (mainly  $\text{C}_3\text{H}_5\text{O}_2^+$ ) (Fig. 7g), which were generally regarded as well-known tracers  
385 for BB emissions (Alfarra et al., 2007). The average fraction of the signal at  $m/z$  60 (referred as  $f_{60}$ )  
386 in the BBOA mass spectrum was 0.61%, which was higher than the typical value of  $\sim 0.3\%$  in the  
387 absence of BB impacts (Cubison et al., 2011). The time series of BBOA correlated tightly with  
388 those of  $\text{C}_2\text{H}_4\text{O}_2^+$  ( $R^2 = 0.91$ ) and  $\text{C}_3\text{H}_5\text{O}_2^+$  ( $R^2 = 0.87$ ) as well as BC ( $R^2 = 0.72$ ) and nitrate ( $R^2 =$   
389  $0.75$ ) (Fig. 7a and Table S2). If ignoring the influence of high contribution at  $m/z$  44, the BBOA  
390 mass spectrum in this study correlated well ( $R^2 = 0.5\text{--}0.9$ ) with those BBOA mass spectrum  
391 identified at other sites worldwide (Ng et al., 2011a; Mohr et al., 2012; Saarikoski et al., 2012;  
392 Crippa et al., 2013; Crippa et al., 2014; Xu et al., 2016), as shown in Fig. S9. The average mass  
393 concentration of BBOA was  $1.05 \mu\text{g m}^{-3}$  for the entire study and contributed a large fraction  
394 (43.7%) of the total OA mass on average (Fig. 8a), indicating that BBOA was an important  
395 components of OA during the pre-monsoon season at the QOMS. The diurnal cycle of BBOA  
396 showed high concentrations during nighttime whereas relatively low concentrations during  
397 daytime (Fig. 7d). Correspondingly, the mass contributions of BBOA to total OA mass decreased  
398 distinctly from  $\sim 55\%$  at 00:00 to 28% at 15:00 (Fig. 8b). In addition, higher mass concentrations  
399 and contributions of BBOA were found during the two polluted episodes (PP1 and PP2) than those  
400 during the clear periods, further indicating the important contribution of BBOA to OA in this  
401 region. Figure 8c showed the mass fractions of the three OA components as a function of total OA  
402 mass during the entire campaign. A continuously increased trend was found for the BBOA  
403 contributions with the increasing OA mass, which contributed  $\sim 15\%$  when the total OA mass was  
404 less than  $0.3 \mu\text{g m}^{-3}$ , whereas it reached up to more than 75% with the OA mass increased to  $9 \mu\text{g}$   
405  $\text{m}^{-3}$ . This dominant contribution of BBOA during the polluted periods was consistent with those  
406 results in previous studies that BB emission were an important source of aerosol to the southern  
407 TPH (Engling et al., 2011; Xia et al., 2011; Putero et al., 2014; Cong et al., 2015). The O/C ratio  
408 (0.85) of BBOA in this study was quite higher than those BBOA factors identified at other  
409 urban/rural sites in previous studies (Aiken et al., 2009; Huang et al., 2011; Mohr et al., 2012; Sun  
410 et al., 2016; Xu et al., 2016), suggesting its long-range transport feature. This aged BBOA feature  
411 was similar with those obtained at other remote sites worldwide, such as a remote forest site in  
412 Finland (Raatikainen et al., 2010), a remote background site in Greece (Bougiatioti et al., 2014),

413 and a national air quality background sites in southern China (Zhu et al., 2016), where OA were  
414 generally highly oxidized.

### 415 3.3.2 NOA

416 Besides the two highest signals at  $m/z$  43.99 ( $\text{CO}_2^+$ ) and 27.995 ( $\text{CO}^+$ ) which together contributed  
417 half of the total NOA signal due to the highly aged OA nature at QOMS, the NOA MS was also  
418 characterized by some nitrogen-containing fragments, such as  $m/z$  27.011 ( $\text{CHN}^+$ ), 41.027  
419 ( $\text{C}_2\text{H}_3\text{N}^+$ ), and 43.006 ( $\text{CHON}^+$ ). In total, these three fragments could comprise nearly half of the  
420 nitrogen-containing signals in the NOA factor and finally contributed 5% of the total NOA signal.  
421 The average O/C ratio of NOA for the entire campaign was 1.10 with the highest N/C ratio (0.068)  
422 among the three OA components. This high N/C ratio at QOMS was comparable with those  
423 nitrogen-containing OA factor identified in previous studies, such as 0.06 in Mexico City (Aiken  
424 et al., 2009), 0.078 in Po Valley, Italy (Saarikoski et al., 2012), and 0.053 in New York (Sun et al.,  
425 2012). The time series of NOA showed tightly correlation ( $R^2 = 0.62$ ) with that of estimated  
426 organic nitrates, whereas relatively weak correlations with  $\text{PM}_{10}$  species and OA ions (Table S2). In  
427 addition, the  $f_{60}$  value ( $\sim 0.37\%$ ) was also slightly higher than the background  $f_{60}$  (0.3%) of BB  
428 aerosols (Fig. 7h). These results together suggested that this oxygenated OA factor was likely a  
429 nitrogen-containing OA and might be related to the aged BB emissions, consistent with the results  
430 in previous studies that large amounts of nitrogen-containing organic compounds were found from  
431 BB aerosols (Laskin et al., 2009; Gautam et al., 2016; Wang et al., 2017). In recently, Fleming et  
432 al. (2017) found dung burning, a very popular activities in Himalayas and India for residential  
433 cooking and heating, could emit much more nitrogen-containing OA than wood burning. Our filter  
434 samples during high BBOA period analyzed by Fourier Transform Ion Cyclotron Resonance Mass  
435 Spectrometry (FTICR-MS) also found amount of ON molecular (in preparation). As shown in Fig.  
436 7e and 8b, both the diurnal cycles of mass concentrations and fractions of NOA had distinct  
437 increase in the morning, similar with the diurnal patterns of chloride, element ratios of H/C and  
438 N/C, and the estimated organic nitrates. This diurnal feature of NOA at QOMS was quite  
439 consistent with those NOA factors identified in Po Valley, Italy (Saarikoski et al., 2012) and in  
440 Mexico City (Aiken et al., 2009), or less-oxidized oxygenated OA (LO-OOA) in southeastern  
441 USA (Xu et al., 2015) where have active BB emissions. NOA contributed  $\sim 14\%$  of the total OA  
442 mass on average, with an average mass concentration of  $0.34 \mu\text{g m}^{-3}$  for the entire study (Fig. 8a).

### 443 3.3.3 MO-OOA

444 An obvious more oxygenated OA factor was also identified in this study according to its  
445 significant high signal at  $m/z$  44 ( $\sim 25\%$ ) and the high average O/C ratio of 1.34 (Fig. 7i). The time  
446 series of MO-OOA correlated closely ( $R^2 = 0.7$ ) with sulfate and nitrate (Fig. 7c and Table S2).  
447 Moreover, the mass spectrum of MO-OOA in this study resembled tightly to those more aged and  
448 low-volatility oxygenated OA (LV-OOA) observed using AMS instruments at various sites  
449 worldwide (Fig. S9), e.g., with  $R^2$  of 0.89 and 0.97 to those in Lanzhou, China (Xu et al., 2014;  
450 Zhang et al., 2017b), 0.96 to that in Paris, France (Crippa et al., 2013), 0.95 to that in Barcelona,  
451 Spain (Mohr et al., 2012), as well as 0.70 and 0.71 to the standard LV-OOA mass spectrums  
452 obtained from abundant AMS data sets by Ng et al. (2011a) and Crippa et al. (2014). The diurnal  
453 variation of MO-OOA was mainly driven by the dynamic of PBL height, with high concentrations  
454 during the nighttime yet relatively low concentrations during the daytime (Fig. 7f). This pattern

455 was quite different with those observed in previous studies that LV-OOA generally showed  
456 elevated concentrations during the afternoon in accordance with strong photochemical activities,  
457 suggesting that SOA at QOMS were mainly oxidized and aged during the long-range transport. On  
458 average, MO-OOA contributed by 42.4% of the total OA mass, with an average mass  
459 concentration of  $1.02 \mu\text{g m}^{-3}$  for the entire study (Fig. 8a). As shown in Fig. 2f and 8c, MO-OOA  
460 also displayed enhanced mass contributions during the clear periods, especially for period after  
461 May 2 when the average mass fraction of MO-OOA increased up to  $\sim 68\%$  of the total OA mass.

### 462 **3.4 Impact of BB emissions on aerosol characteristics**

#### 463 **3.4.1 Sources of BB aerosols**

464 In order to understand the transport pathways and the potential source areas of aerosol, 3-day back  
465 trajectories of air mass were calculated at an ending height of 500 m above ground level every 6 h  
466 at the QOMS from April 12 to May 12, 2016. A four-cluster solution and the wildfire hotspots  
467 around the QOMS during the entire measurement period were presented in Fig. 9. Cluster 1 and 2  
468 (C1 and C2), which originated from the west of the QOMS and passed over many hotspot areas  
469 (e.g., Indo-Gangetic Plain and Nepal), represented two polluted clusters. On the contrary, C3 and  
470 C4, which accounted for half of the total back trajectories, were identified as clear clusters. C3  
471 traveled a short distance from the southwest of the QOMS, whereas C4 was from the north of the  
472 QOMS and passed over the inland of the TPH. The average  $\text{PM}_{10}$  mass concentrations for C1 and  
473 C2 were  $5.17$  and  $6.61 \mu\text{g m}^{-3}$ , respectively, which were 2–3 times higher than those for the two  
474 clear clusters ( $2.74$  and  $2.21 \mu\text{g m}^{-3}$ ). The mass contributions of OA and BBOA during C1 and C2  
475 were up to more than 55% and 25% of the total  $\text{PM}_{10}$  mass on average, whereas weak contributions  
476 were found for the clear clusters (C3 and C4), indicating the significant impacts of BB emissions  
477 from South Asia on aerosol loadings at QOMS.

#### 478 **3.4.2 Comparison of aerosol characteristics and air mass origins during different episodes**

479 As shown in Fig. 2, the mass concentrations and compositions of  $\text{PM}_{10}$  varied dynamically during  
480 the entire sampling period. Two polluted periods (PP1 and PP2) and two clear periods (CP1 and  
481 CP2) were identified. The comparisons of average mass concentrations and other indicators for the  
482 four different episodes were presented in box plots in Fig. 10, whereas the corresponding back  
483 trajectories of air masses and MODIS fire hotspots belong to each episode period were given in  
484 Fig. 11, respectively.

485 During the two polluted periods,  $\text{PM}_{10}$  mass concentrations were much higher than those in  
486 clear periods ( $8.06$  and  $7.87 \mu\text{g m}^{-3}$  for PP1 and PP2 vs.  $2.76$  and  $1.82 \mu\text{g m}^{-3}$  for CP1 and CP2;  
487 similarly hereinafter), with higher contributions from OA (60.1% and 57.5% vs. 48.1% and 43.9%)  
488 and BBOA (38.3% and 36.6% vs. 14.3% and 7.5%) (Fig. 10 and 11). In addition,  $f_{60}$  were also  
489 higher during polluted periods than those for clear periods (0.34% and 0.34% vs. 0.26% and 0.22%  
490 on average) (Fig. 10). Air masses during PP1 and PP2 generally originated from long-range  
491 transport to the west of the QOMS, which would pass through intense wildfires areas in South  
492 Asia (e.g., Indo-Gangetic Plain and Nepal where showed high AOD values in Fig. 1d and active  
493 fire hotspots in Fig. 9 and 11). The fire hotspot number around the air mass trajectories during PP2  
494 was more than three times higher than those during other periods. Although the hotspot number  
495 around the air mass trajectories during PP1 was not as abundant as that during PP2 and even

496 slightly lower than that during CP1, it was just collected within 3 days for PP1 whereas 8-10 days  
497 for another periods. Hence, the BB activities were also more frequent and intense during the short  
498 PP1 and finally resulted in the highest average PM<sub>1</sub> mass concentration among these periods.  
499 Back trajectories in CP1 also originated from the west of QOMS and passed over the northern  
500 India and Nepal, however, both the intensity of fire hotspot number (1089 hotspots in ~ 8 days)  
501 and average FRP (19.6) were obvious lower than that in PP2. CP2 was the most clear period, of  
502 which average PM<sub>1</sub> mass concentration was more than four times lower than those in polluted  
503 periods. Back trajectories during CP2 period were from either the north of QOMS which passed  
504 over inland areas of the TPH or the south of QOMS with quite short distance and low WS. These  
505 results together suggested the significant roles of air mass sources and BB emissions to aerosol  
506 characteristics at QOMS.

### 507 **3.4.3 Case study on the chemical evolution of BB emission aerosols**

508 In order to examine how atmospheric aging affects the aerosol chemistry characteristics at QOMS,  
509 a typical evolution process of BB aerosol plume (referred as BB evolution case) was analyzed  
510 from April 30 at 15:00 when a fresh BB plume occurred to May 1 at 18:00 when the BB plume  
511 was highly aged after undergoing various atmospheric oxidation processes. The temporal  
512 variations of meteorological parameters, mass concentrations and mass contributions of each PM<sub>1</sub>  
513 species and OA components as well as other chemistry parameters before and during this BB  
514 evolution case were all shown in Fig. 12.

515 Before the BB evolution case, all the mass concentrations decreased slowly and synchronously  
516 from 00:00 to 10:00 on April 30, which were consistent with the nearly stable trends of mass  
517 contributions and other chemistry parameters, indicating the relatively unified air mass sources  
518 and stable atmospheric conditions. After that, the wind circulations changed from the thermally-  
519 driven down-slope winds (mostly southwest) to the weak up-slope winds (northeast). In this  
520 period, BBOA and  $f_{60}$  values kept relatively stable in contrast to other species likely due to the  
521 weak of air dilution and local sources. All the species reached the minimum at around 15:00 due to  
522 the lift of PBL.

523 The BB evolution case in this study was further divided into three different situations (as  
524 marked with arrows in Fig. 12 and 13), including the arriving of the fresh BBOA plume (from  
525 15:00 to 24:00 on April 30), followed by the aqueous-phase oxidation in the nighttime (from 2:30  
526 to 7:10 on May 1) and photochemical oxidation in the daytime (from 10:00 to 18:00 on May 1).  
527 All the mass concentrations began to increase from 15:00 and finally reached the maximum PM<sub>1</sub>  
528 mass loading of 18.4  $\mu\text{g m}^{-3}$  at 24:00, which was about four times higher than the average PM<sub>1</sub>  
529 mass during the entire campaign. Thus continuous increase was mainly dominated by the dramatic  
530 increase of BBOA, which reached up to 10.8  $\mu\text{g m}^{-3}$  and contributed 88% of the total OA mass  
531 and 50% of the total PM<sub>1</sub> at 24:00 (Fig. 13a), suggesting a distinct presence of BB emissions  
532 during this period. In contrast, the total OA mass was comprised by 78% of MO-OOA and 12% of  
533 BBOA at 15:00. Similar continuous increase trend could also be found for the mass concentration  
534 of calculated organic nitrate in this stage. In addition, nine aerosol chemistry parameters were  
535 presented as a function of BBOA mass concentrations during this period (Fig. 13b). The mass  
536 contributions of OA to PM<sub>1</sub> ( $f_{\text{org}}$ ) and BBOA to total OA ( $f_{\text{BBOA}}$ ),  $f_{60}$ , and H/C ratio were all  
537 increased with the increasing BBOA mass, whereas the mass contribution of MO-OOA to total

538 OA ( $f_{\text{MO-OOA}}$ ), O/C ratio, carbon oxidation state ( $\text{OS}_c = 2 \times \text{O/C} - \text{H/C}$ ) of OA, and aerosol single  
539 scattering albedo (SSA) were decreased obviously, indicating the fresh nature of this BB plume.  
540 The significant impacts of fresh BB plume during this period was mainly associated with the  
541 unique wind circulation and the long-range transport of air masses. As displayed in Fig. 12b, the  
542 wind circulation changed from the weak up-slope winds to the strong down-slope glacier winds on  
543 April 30 at 15:00, with the WS increased from  $\sim 2$  to  $8 \text{ m s}^{-1}$ . Meanwhile, the back trajectories in  
544 this period also presented that the long-range transport of air masses passed over the northern  
545 India and Nepal where active wildfires occurred, then air masses would accumulate and uplift to  
546 cross the Himalayas and finally downward to QOMS with the strong glacier winds.

547 A distinct aqueous-phase oxidation process was found in the nighttime from 02:30 to 07:10 on  
548 May 1. Although the total  $\text{PM}_1$  and its species showed nearly stable mass concentrations during  
549 this period, the BBOA mass decreased gradually (from 82% to 70%) whereas MO-OOA increased  
550 constantly (from 14% to 20%) with the significant increase of RH (up to 91%) and aerosol liquid  
551 water content (ALWC) (Fig. 12). The scattering plots of the aerosol chemistry parameters versus  
552 the logarithmic values of cumulative ALWC, which could be used for the aqueous-phase oxidation  
553 during transport, also showed apparent increase trends for  $f_{\text{MO-OOA}}$ , O/C ratio,  $\text{OS}_c$ , and SSA that  
554 generally indicated the aerosol aging extent. All of these together suggested a distinct aqueous-  
555 phase oxidation of BBOA in the nighttime.

556 Since sunrise, all the mass concentrations decreased gradually, mainly related to the increasing  
557 PBL height and the clear air mass dilution. The back trajectories indicated that air masses during  
558 this period firstly went into the inland of the north of QOMS where had rare wildfires. Moreover,  
559 the BB plume would further undergo strong photochemical oxidation in the daytime due to the  
560 strong solar radiation. MO-OOA just contributed 26% of the total OA mass at 10:00, but it could  
561 increase to 74% at 18:00 after long-time photochemical oxidation. In contrast, BBOA mass  
562 contribution decreased from 49% to 20%. The cumulative solar radiation, which denoted the total  
563 amount of solar radiation that the plumes were exposed to during transport, could be used as an  
564 indicator for the extent of photochemical aging in the daytime (Zhou et al., 2017). Clear increased  
565 trend were found for  $f_{\text{MO-OOA}}$ , O/C ratio,  $\text{OS}_c$ , and SSA values with the increasing of cumulative  
566 solar radiation, whereas decreased trend in  $f_{\text{BBOA}}$ ,  $f_{\text{NOA}}$ , H/C ratio, and  $f_{60}$  values, suggesting a  
567 possible oxidation mechanism that the relatively fresh BBOA and NOA oxidized to aged MO-  
568 OOA in the daytime. Another interesting phenomenon was the continuous increase of SSA during  
569 both the aqueous-phase and photochemical oxidation periods on May 1 (Fig. 12e and 13b),  
570 indicating the potential influence of atmospheric aging to aerosol optical property at QOMS.

## 571 **4 Conclusions**

572 A comprehensive characterization of submicron aerosol chemical compositions and sources was  
573 investigated at the QOMS during the pre-monsoon season in 2016. The average mass  
574 concentration of  $\text{PM}_1$  (NR- $\text{PM}_1$  + BC) was  $4.44 (\pm 4.54) \mu\text{g m}^{-3}$  for the entire study, which was  
575 much lower than those observed in various sites in China. OA was the dominant  $\text{PM}_1$  species  
576 (accounted for 54.3% of the total mass on average) and its contributions increased with the  
577 increase  $\text{PM}_1$  mass loading. The average size distributions of all  $\text{PM}_1$  species displayed an  
578 overlapping and narrow accumulation mode at  $\sim 500 \text{ nm}$ , indicating the internally well-mixed and  
579 aged aerosol particles at QOMS. All species presented similar diurnal cycles, with lower

580 concentrations in the daytime whereas higher concentrations at the nighttime, mainly attributed to  
581 the dynamic variations of PBL height. Three OA factors were identified by PMF analysis on the  
582 high-resolution OA mass spectrum, including a relatively fresh BB-related OA (BBOA), a  
583 nitrogen-containing OA (NOA) and a more-oxidized oxygenated OA (MO-OOA). BBOA and  
584 MO-OOA could respectively account for 43.7% and 42.4% of OA mass on average, however,  
585 their contributions to OA showed completely opposite variation trends with the increase of OA  
586 mass. A continuously increased trend could be found for BBOA with the increasing OA,  
587 suggesting the key role of BBOA during polluted periods when frequent and intense wildfires  
588 were observed in South Asia. The significant impact of BB emissions on aerosol characteristics at  
589 QOMS have been also illustrated for different air mass origins and periods, respectively. Elevated  
590 PM<sub>1</sub> mass concentrations and high contributions of BBOA were found for both polluted clusters  
591 and polluted periods. A case study of typical evolution process of BB aerosol plume was  
592 investigated in detail to illustrate the chemical evolution of aerosol characteristics at QOMS. The  
593 fresh BB plume occurred in the afternoon on April 30 and finally resulted in highly PM<sub>1</sub> mass  
594 loading of 18.4 μg m<sup>-3</sup>, which was about four times higher than the average PM<sub>1</sub> mass during the  
595 entire campaign. Obvious aqueous-phase oxidation and photochemical oxidation processes were  
596 analyzed in the nighttime and daytime on May 1, respectively, both suggesting the oxidation  
597 mechanism that fresh BBOA to aged MO-OOA. The continuous increase of SSA during the two  
598 oxidation periods suggested the potential influence of atmospheric aging to aerosol optical  
599 property at QOMS.

600 *Acknowledgements.* This research was supported by grants from the National Natural Science Foundation of China  
601 (41771079, 41421061), the Key Laboratory of Cryospheric Sciences Scientific Research Foundation (SKLCS-ZZ-  
602 2017-01), and the Chinese Academy of Sciences Hundred Talents Program. The authors thank the colleagues for  
603 continuing support and discussion, and thank the NOAA Air Resources Laboratory, NASA MODIS and FIRMS  
604 teams for providing the HYSPLIT trajectory model, AOD and fire hotspots datasets.

## 605 **References**

- 606 Aiken, A. C., DeCarlo, P. F., Kroll, J. H., Worsnop, D. R., Huffman, J. A., Docherty, K. S., Ulbrich, I. M., Mohr, C., Kimmel, J.  
607 R., Sueper, D., Sun, Y., Zhang, Q., Trimborn, A., Northway, M., Ziemann, P. J., Canagaratna, M. R., Onasch, T. B., Alfarra, M.  
608 R., Prevot, A. S. H., Dommen, J., Duplissy, J., Metzger, A., Baltensperger, U., and Jimenez, J. L.: O/C and OM/OC ratios of  
609 primary, secondary, and ambient organic aerosols with high-resolution time-of-flight aerosol mass spectrometry, *Environ. Sci.*  
610 *Technol.*, 42, 4478-4485, doi:10.1021/es703009q, 2008.
- 611 Aiken, A. C., Salcedo, D., Cubison, M. J., Huffman, J. A., DeCarlo, P. F., Ulbrich, I. M., Docherty, K. S., Sueper, D., Kimmel, J.  
612 R., Worsnop, D. R., Trimborn, A., Northway, M., Stone, E. A., Schauer, J. J., Volkamer, R. M., Fortner, E., de Foy, B., Wang, J.,  
613 Laskin, A., Shutthanandan, V., Zheng, J., Zhang, R., Gaffney, J., Marley, N. A., Paredes-Miranda, G., Arnott, W. P., Molina, L.  
614 T., Sosa, G., and Jimenez, J. L.: Mexico City aerosol analysis during MILAGRO using high resolution aerosol mass  
615 spectrometry at the urban supersite (T0)–Part 1: Fine particle composition and organic source apportionment, *Atmos. Chem.*  
616 *Phys.*, 9, 6633-6653, doi:10.5194/acp-9-6633-2009, 2009.
- 617 Alfarra, M. R., Coe, H., Allan, J. D., Bower, K. N., Boudries, H., Canagaratna, M. R., Jimenez, J. L., Jayne, J. T., Garforth, A. A.,  
618 Li, S.-M., and Worsnop, D. R.: Characterization of urban and rural organic particulate in the Lower Fraser Valley using two  
619 Aerodyne Aerosol Mass Spectrometers, *Atmos. Environ.*, 38, 5745-5758, doi:10.1016/j.atmosenv.2004.01.054, 2004.
- 620 Alfarra, M. R., Prevot, A. S. H., Szidat, S., Sandradewi, J., Weimer, S., Lanz, V. A., Schreiber, D., Mohr, M., and Baltensperger,  
621 U.: Identification of the Mass Spectral Signature of Organic Aerosols from Wood Burning Emissions, *Environ. Sci. Technol.*,  
622 41, 5770-5777, doi:10.1021/es062289b, 2007.
- 623 Bonasoni, P., Laj, P., Marinoni, A., Sprenger, M., Angelini, F., Arduini, J., Bonafè U., Calzolari, F., Colombo, T., Decesari, S., Di  
624 Biagio, C., di Sarra, A. G., Evangelisti, F., Duchi, R., Facchini, M. C., Fuzzi, S., Gobbi, G. P., Maione, M., Panday, A., Roccatò,  
625 F., Sellegri, K., Venzac, H., Verza, G. P., Villani, P., Vuilleumoz, E., and Cristofanelli, P.: Atmospheric Brown Clouds in the

626 Himalayas: first two years of continuous observations at the Nepal Climate Observatory-Pyramid (5079 m), *Atmos. Chem.*  
627 *Phys.*, 10, 7515-7531, doi:10.5194/acp-10-7515-2010, 2010.

628 Bond, T. C., Streets, D. G., Yarber, K. F., Nelson, S. M., Woo, J.-H., and Klimont, Z.: A technology-based global inventory of  
629 black and organic carbon emissions from combustion, *J. Geophys. Res.*, 109, doi:10.1029/2003jd003697, 2004.

630 Bougiatioti, A., Stavroulas, I., Kostenidou, E., Zarpas, P., Theodosi, C., Kouvarakis, G., Canonaco, F., Prévôt, A. S. H., Nenes,  
631 A., Pandis, S. N., and Mihalopoulos, N.: Processing of biomass-burning aerosol in the eastern Mediterranean during  
632 summertime, *Atmos. Chem. Phys.*, 14, 4793-4807, doi:10.5194/acp-14-4793-2014, 2014.

633 Canagaratna, M. R., Jayne, J. T., Jimenez, J. L., Allan, J. D., Alfarra, M. R., Zhang, Q., Onasch, T. B., Drewnick, F., Coe, H.,  
634 Middlebrook, A., Delia, A., Williams, L. R., Trimborn, A. M., Northway, M. J., DeCarlo, P. F., Kolb, C. E., Davidovits, P., and  
635 Worsnop, D. R.: Chemical and microphysical characterization of ambient aerosols with the aerodyne aerosol mass  
636 spectrometer, *Mass Spectrom. Rev.*, 26, 185-222, doi:10.1002/mas.20115, 2007.

637 Canagaratna, M. R., Jimenez, J. L., Kroll, J. H., Chen, Q., Kessler, S. H., Massoli, P., Hildebrandt Ruiz, L., Fortner, E., Williams,  
638 L. R., Wilson, K. R., Surratt, J. D., Donahue, N. M., Jayne, J. T., and Worsnop, D. R.: Elemental ratio measurements of organic  
639 compounds using aerosol mass spectrometry: characterization, improved calibration, and implications, *Atmos. Chem. Phys.*,  
640 15, 253-272, doi:10.5194/acp-15-253-2015, 2015.

641 Cong, Z., Kang, S., Kawamura, K., Liu, B., Wan, X., Wang, Z., Gao, S., and Fu, P.: Carbonaceous aerosols on the south edge of  
642 the Tibetan Plateau: concentrations, seasonality and sources, *Atmos. Chem. Phys.*, 15, 1573-1584, doi:10.5194/acp-15-1573-  
643 2015, 2015.

644 Crippa, M., DeCarlo, P. F., Slowik, J. G., Mohr, C., Heringa, M. F., Chirico, R., Poulain, L., Freutel, F., Sciare, J., Cozic, J., Di  
645 Marco, C. F., Elsasser, M., Nicolas, J. B., Marchand, N., Abidi, E., Wiedensohler, A., Drewnick, F., Schneider, J., Borrmann, S.,  
646 Nemitz, E., Zimmermann, R., Jaffrezo, J. L., Prévôt, A. S. H., and Baltensperger, U.: Wintertime aerosol chemical composition  
647 and source apportionment of the organic fraction in the metropolitan area of Paris, *Atmos. Chem. Phys.*, 13, 961-981,  
648 doi:10.5194/acp-13-961-2013, 2013.

649 Crippa, M., Canonaco, F., Lanz, V. A., Äijä M., Allan, J. D., Carbone, S., Capes, G., Ceburnis, D., Dall'Osto, M., Day, D. A.,  
650 DeCarlo, P. F., Ehn, M., Eriksson, A., Freney, E., Hildebrandt Ruiz, L., Hillamo, R., Jimenez, J. L., Junninen, H., Kiendler-  
651 Scharr, A., Kortelainen, A. M., Kulmala, M., Laaksonen, A., Mensah, A. A., Mohr, C., Nemitz, E., O'Dowd, C., Ovadnevaite,  
652 J., Pandis, S. N., Petäjä T., Poulain, L., Saarikoski, S., Sellegri, K., Swietlicki, E., Tiitta, P., Worsnop, D. R., Baltensperger, U.,  
653 and Prévôt, A. S. H.: Organic aerosol components derived from 25 AMS data sets across Europe using a consistent ME-2  
654 based source apportionment approach, *Atmos. Chem. Phys.*, 14, 6159-6176, doi:10.5194/acp-14-6159-2014, 2014.

655 Cubison, M. J., Ortega, A. M., Hayes, P. L., Farmer, D. K., Day, D., Lechner, M. J., Brune, W. H., Apel, E., Diskin, G. S., Fisher,  
656 J. A., Fuelberg, H. E., Hecobian, A., Knapp, D. J., Mikoviny, T., Riemer, D., Sachse, G. W., Sessions, W., Weber, R. J.,  
657 Weinheimer, A. J., Wisthaler, A., and Jimenez, J. L.: Effects of aging on organic aerosol from open biomass burning smoke in  
658 aircraft and laboratory studies, *Atmos. Chem. Phys.*, 11, 12049-12064, doi:10.5194/acp-11-12049-2011, 2011.

659 DeCarlo, P. F., Kimmel, J. R., Trimborn, A., Northway, M. J., Jayne, J. T., Aiken, A. C., Gonin, M., Fuhrer, K., Horvath, T.,  
660 Docherty, K. S., Worsnop, D. R., and Jimenez, J. L.: Field-Deployable, High-Resolution, Time-of-Flight Aerosol Mass  
661 Spectrometer, *Anal. Chem.*, 78, 8281-8289, doi:10.1021/ac061249n, 2006.

662 Decesari, S., Facchini, M. C., Carbone, C., Giulianelli, L., Rinaldi, M., Finessi, E., Fuzzi, S., Marinoni, A., Cristofanelli, P.,  
663 Duchi, R., Bonasoni, P., Vuillermoz, E., Cozic, J., Jaffrezo, J. L., and Laj, P.: Chemical composition of PM10 and PM1 at the  
664 high-altitude Himalayan station Nepal Climate Observatory-Pyramid (NCO-P) (5079 m a.s.l.), *Atmos. Chem. Phys.*, 10, 4583-  
665 4596, doi:10.5194/acp-10-4583-2010, 2010.

666 Draxler, R. R., and Rolph, G. D.: HYSPLIT (HYbrid Single-Particle Lagrangian Integrated Trajectory) model access via NOAA  
667 ARL READY website (<http://www.arl.noaa.gov/ready/hysplit4.html>). NOAA Air Resources Laboratory, Silver Spring, MD,  
668 USA, 2003.

669 Du, W., Sun, Y. L., Xu, Y. S., Jiang, Q., Wang, Q. Q., Yang, W., Wang, F., Bai, Z. P., Zhao, X. D., and Yang, Y. C.: Chemical  
670 characterization of submicron aerosol and particle growth events at a national background site (3295 m a.s.l.) on the Tibetan  
671 Plateau, *Atmos. Chem. Phys.*, 15, 10811-10824, doi:10.5194/acp-15-10811-2015, 2015.

672 Duan, A. M., and Wu, G. X.: Role of the Tibetan Plateau thermal forcing in the summer climate patterns over subtropical Asia,  
673 *Climate Dynamics*, 24, 793-807, doi:10.1007/s00382-004-0488-8, 2005.

674 Engling, G., Zhang, Y. N., Chan, C. Y., Sang, X. F., Lin, M., Ho, K. F., Li, Y. S., Lin, C. Y., and Lee, J. J.: Characterization and  
675 sources of aerosol particles over the southeastern Tibetan Plateau during the Southeast Asia biomass-burning season, *Tellus B*,  
676 63, 117-128, doi:10.1111/j.1600-0889.2010.00512.x, 2011.

677 Fleming, L. T., Lin, P., Laskin, A., Laskin, J., Weltman, R., Edwards, R. D., Arora, N. K., Yadav, A., Meinardi, S., Blake, D. R.,  
678 Pillarisetti, A., Smith, K. R., and Nizkorodov, S. A.: Molecular Composition of Particulate Matter Emissions from Dung and  
679 Brushwood Burning Household Cookstoves in Haryana, India, *Atmos. Chem. Phys. Discuss.*, 1-35, doi:10.5194/acp-2017-784,  
680 2017.

681 Fröhlich, R., Cubison, M. J., Slowik, J. G., Bukowiecki, N., Canonaco, F., Croteau, P. L., Gysel, M., Henne, S., Herrmann, E.,  
682 Jayne, J. T., Steinbacher, M., Worsnop, D. R., Baltensperger, U., and Prévôt, A. S. H.: Fourteen months of on-line  
683 measurements of the non-refractory submicron aerosol at the Jungfraujoch (3580 m a.s.l.) – chemical composition, origins and



684 organic aerosol sources, *Atmos. Chem. Phys.*, 15, 11373-11398, doi:10.5194/acp-15-11373-2015, 2015.

685 Gautam, S., Edwards, R., Yadav, A., Weltman, R., Pillarsetti, A., Arora, N. K., and Smith, K. R.: Probe-based measurements of  
686 moisture in dung fuel for emissions measurements, *Energy for Sustainable Development*, 35, 1-6,  
687 doi:10.1016/j.esd.2016.09.003, 2016.

688 Ge, X., Zhang, Q., Sun, Y., Ruehl, C. R., and Setyan, A.: Effect of aqueous-phase processing on aerosol chemistry and size  
689 distributions in Fresno, California, during wintertime, *Environ. Chem.*, 9, 221, doi:10.1071/en11168, 2012.

690 Heald, C. L., Kroll, J. H., Jimenez, J. L., Docherty, K. S., DeCarlo, P. F., Aiken, A. C., Chen, Q., Martin, S. T., Farmer, D. K., and  
691 Artaxo, P.: A simplified description of the evolution of organic aerosol composition in the atmosphere, *Geophys. Res. Lett.*, 37,  
692 L08803, doi:10.1029/2010gl042737, 2010.

693 Hou, S., Qin, D., Zhang, D., Kang, S., Mayewski, P. A., and Wake, C. P.: A 154a high-resolution ammonium record from the  
694 Rongbuk Glacier, north slope of Mt. Qomolangma (Everest), Tibet-Himal region, *Atmos. Environ.*, 37, 721-729,  
695 doi:10.1016/S1352-2310(02)00582-4, 2003.

696 Hu, W., Hu, M., Hu, W.-W., Niu, H., Zheng, J., Wu, Y., Chen, W., Chen, C., Li, L., Shao, M., Xie, S., and Zhang, Y.:  
697 Characterization of submicron aerosols influenced by biomass burning at a site in the Sichuan Basin, southwestern China,  
698 *Atmos. Chem. Phys.*, 16, 13213-13230, doi:10.5194/acp-16-13213-2016, 2016.

699 Huang, X. F., He, L. Y., Hu, M., Canagaratna, M. R., Kroll, J. H., Ng, N. L., Zhang, Y. H., Lin, Y., Xue, L., Sun, T. L., Liu, X. G.,  
700 Shao, M., Jayne, J. T., and Worsnop, D. R.: Characterization of submicron aerosols at a rural site in Pearl River Delta of China  
701 using an Aerodyne High-Resolution Aerosol Mass Spectrometer, *Atmos. Chem. Phys.*, 11, 1865-1877, doi:10.5194/acp-11-  
702 1865-2011, 2011.

703 Huang, X. F., He, L. Y., Xue, L., Sun, T. L., Zeng, L. W., Gong, Z. H., Hu, M., and Zhu, T.: Highly time-resolved chemical  
704 characterization of atmospheric fine particles during 2010 Shanghai World Expo, *Atmos. Chem. Phys.*, 12, 4897-4907,  
705 doi:10.5194/acp-12-4897-2012, 2012.

706 Jayne, J. T., Leard, D. C., Zhang, X. F., Davidovits, P., Smith, K. A., Kolb, C. E., and Worsnop, D. R.: Development of an aerosol  
707 mass spectrometer for size and composition analysis of submicron particles, *Aerosol Sci. Technol.*, 33, 49-70,  
708 doi:10.1080/027868200410840, 2000.

709 Jimenez, J. L., Jayne, J. T., Shi, Q., Kolb, C. E., Worsnop, D. R., Yourshaw, I., Seinfeld, J. H., Flagan, R. C., Zhang, X., Smith, K.  
710 A., Morris, J. W., and Davidovits, P.: Ambient aerosol sampling using the Aerodyne Aerosol Mass Spectrometer, *J. Geophys.*  
711 *Res.*, 108, doi:10.1029/2001jd001213, 2003.

712 Jimenez, J. L., Canagaratna, M. R., Donahue, N. M., Prevot, A. S., Zhang, Q., Kroll, J. H., DeCarlo, P. F., Allan, J. D., Coe, H.,  
713 Ng, N. L., Aiken, A. C., Docherty, K. S., Ulbrich, I. M., Grieshop, A. P., Robinson, A. L., Duplissy, J., Smith, J. D., Wilson, K.  
714 R., Lanz, V. A., Hueglin, C., Sun, Y. L., Tian, J., Laaksonen, A., Raatikainen, T., Rautiainen, J., Vaattovaara, P., Ehn, M.,  
715 Kulmala, M., Tomlinson, J. M., Collins, D. R., Cubison, M. J., Dunlea, E. J., Huffman, J. A., Onasch, T. B., Alfarra, M. R.,  
716 Williams, P. I., Bower, K., Kondo, Y., Schneider, J., Drewnick, F., Borrmann, S., Weimer, S., Demerjian, K., Salcedo, D.,  
717 Cottrell, L., Griffin, R., Takami, A., Miyoshi, T., Hatakeyama, S., Shimono, A., Sun, J. Y., Zhang, Y. M., Dzepina, K., Kimmel,  
718 J. R., Sueper, D., Jayne, J. T., Herndon, S. C., Trimborn, A. M., Williams, L. R., Wood, E. C., Middlebrook, A. M., Kolb, C. E.,  
719 Baltensperger, U., and Worsnop, D. R.: Evolution of organic aerosols in the atmosphere, *Science*, 326, 1525-1529,  
720 doi:10.1126/science.1180353, 2009.

721 Kang, S., Xu, Y., You, Q., Flügel, W.-A., Pepin, N., and Yao, T.: Review of climate and cryospheric change in the Tibetan Plateau,  
722 *Environ. Res. Lett.*, 5, 015101, doi:10.1088/1748-9326/5/1/015101, 2010.

723 Laskin, A., Smith, J. S., and Laskin, J.: Molecular Characterization of Nitrogen-Containing Organic Compounds in Biomass  
724 Burning Aerosols Using High-Resolution Mass Spectrometry, *Environ. Sci. Technol.*, 43, 3764-3771, doi:10.1021/es803456n,  
725 2009.

726 Lau, K. M., Kim, M. K., and Kim, K. M.: Asian summer monsoon anomalies induced by aerosol direct forcing: the role of the  
727 Tibetan Plateau, *Climate Dynamics*, 26, 855-864, doi:10.1007/s00382-006-0114-z, 2006.

728 Lau, K. M., Tsay, S. C., Hsu, C., Chin, M., Ramanathan, V., Wu, G. X., Li, Z., Sikka, R., Holben, B., Lu, D., Chen, H., Tartari, G.,  
729 Koudelova, P., Ma, Y., Huang, J., Taniguchi, K., and Zhang, R.: The Joint Aerosol-Monsoon Experiment: A New Challenge  
730 for Monsoon Climate Research, *Bulletin of the American Meteorological Society*, 89, 369-383, doi:10.1175/bams-89-3-369,  
731 2008.

732 Li, C., Bosch, C., Kang, S., Andersson, A., Chen, P., Zhang, Q., Cong, Z., Chen, B., Qin, D., and Gustafsson, O.: Sources of  
733 black carbon to the Himalayan-Tibetan Plateau glaciers, *Nat. Commun.*, 7, 12574, doi:10.1038/ncomms12574, 2016.

734 Li, Y. J., Sun, Y., Zhang, Q., Li, X., Li, M., Zhou, Z., and Chan, C. K.: Real-time chemical characterization of atmospheric  
735 particulate matter in China: A review, *Atmos. Environ.*, 158, 270-304, doi:10.1016/j.atmosenv.2017.02.027, 2017.

736 Liu, B., Cong, Z., Wang, Y., Xin, J., Wan, X., Pan, Y., Liu, Z., Wang, Y., Zhang, G., Wang, Z., Wang, Y., and Kang, S.:  
737 Background aerosol over the Himalayas and Tibetan Plateau: observed characteristics of aerosol mass loading, *Atmos. Chem.*  
738 *Phys.*, 17, 449-463, doi:10.5194/acp-17-449-2017, 2017.

739 Liu, Z., Liu, D., Huang, J., Vaughan, M., Uno, I., Sugimoto, N., Kittaka, C., Trepte, C., Wang, Z., Hostetler, C., and Winker, D.:  
740 Airborne dust distributions over the Tibetan Plateau and surrounding areas derived from the first year of CALIPSO lidar  
741 observations, *Atmos. Chem. Phys.*, 8, 5045-5060, doi:10.5194/acp-8-5045-2008, 2008.

742 Ma, Y., Kang, S., Zhu, L., Xu, B., Tian, L., and Yao, T.: ROOF OF THE WORLD: Tibetan Observation and Research Platform,  
743 Bulletin of the American Meteorological Society, 89, 1487-1492, doi:10.1175/2008bams2545.1, 2008.

744 Marcq, S., Laj, P., Roger, J. C., Villani, P., Sellegri, K., Bonasoni, P., Marinoni, A., Cristofanelli, P., Verza, G. P., and Bergin, M.:  
745 Aerosol optical properties and radiative forcing in the high Himalaya based on measurements at the Nepal Climate  
746 Observatory-Pyramid site (5079 m a.s.l.), Atmos. Chem. Phys., 10, 5859-5872, doi:10.5194/acp-10-5859-2010, 2010.

747 Marinoni, A., Cristofanelli, P., Laj, P., Duchi, R., Putero, D., Calzolari, F., Landi, T. C., Vuillermoz, E., Maione, M., and  
748 Bonasoni, P.: High black carbon and ozone concentrations during pollution transport in the Himalayas: Five years of  
749 continuous observations at NCO-P global GAW station, J. Environ. Sci., 25, 1618-1625, doi:10.1016/S1001-0742(12)60242-3,  
750 2013.

751 Mohr, C., DeCarlo, P. F., Heringa, M. F., Chirico, R., Slowik, J. G., Richter, R., Reche, C., Alastuey, A., Querol, X., Seco, R.,  
752 Peñuelas, J., Jiménez, J. L., Crippa, M., Zimmermann, R., Baltensperger, U., and Prévôt, A. S. H.: Identification and  
753 quantification of organic aerosol from cooking and other sources in Barcelona using aerosol mass spectrometer data, Atmos.  
754 Chem. Phys., 12, 1649-1665, doi:10.5194/acp-12-1649-2012, 2012.

755 Ng, N., Canagaratna, M., Jimenez, J., Zhang, Q., Ulbrich, I., and Worsnop, D.: Real-time methods for estimating organic  
756 component mass concentrations from aerosol mass spectrometer data, Environ. Sci. Technol., 45, 910-916,  
757 doi:10.1021/es102951k, 2011a.

758 Ng, N. L., Canagaratna, M. R., Jimenez, J. L., Chhabra, P. S., Seinfeld, J. H., and Worsnop, D. R.: Changes in organic aerosol  
759 composition with aging inferred from aerosol mass spectra, Atmos. Chem. Phys., 11, 6465-6474, doi:10.5194/acp-11-6465-  
760 2011, 2011b.

761 Paatero, P., and Tapper, U.: Positive matrix factorization: A non-negative factor model with optimal utilization of error estimates  
762 of data values, Environmetrics, 5, 111-126, doi:10.1002/env.3170050203, 1994.

763 Putero, D., Landi, T. C., Cristofanelli, P., Marinoni, A., Laj, P., Duchi, R., Calzolari, F., Verza, G. P., and Bonasoni, P.: Influence  
764 of open vegetation fires on black carbon and ozone variability in the southern Himalayas (NCO-P, 5079 m a.s.l.), Environ.  
765 Pollut., 184, 597-604, doi:10.1016/j.envpol.2013.09.035, 2014.

766 Raatikainen, T., Vaattovaara, P., Tiitta, P., Miettinen, P., Rautiainen, J., Ehn, M., Kulmala, M., Laaksonen, A., and Worsnop, D. R.:  
767 Physicochemical properties and origin of organic groups detected in boreal forest using an aerosol mass spectrometer, Atmos.  
768 Chem. Phys., 10, 2063-2077, doi:10.5194/acp-10-2063-2010, 2010.

769 Ram, K., Sarin, M. M., and Hegde, P.: Long-term record of aerosol optical properties and chemical composition from a high-  
770 altitude site (Manora Peak) in Central Himalaya, Atmos. Chem. Phys., 10, 11791-11803, doi:10.5194/acp-10-11791-2010,  
771 2010.

772 Ramanathan, V., and Carmichael, G.: Global and regional climate changes due to black carbon, Nature Geoscience, 1, 221-227,  
773 doi:10.1038/ngeo156, 2008.

774 Saarikoski, S., Carbone, S., Decesari, S., Giulianelli, L., Angelini, F., Canagaratna, M., Ng, N. L., Trimborn, A., Facchini, M. C.,  
775 Fuzzi, S., Hillamo, R., and Worsnop, D.: Chemical characterization of springtime submicrometer aerosol in Po Valley, Italy,  
776 Atmos. Chem. Phys., 12, 8401-8421, doi:10.5194/acp-12-8401-2012, 2012.

777 Sun, Y., Zhang, Q., Macdonald, A., Hayden, K., Li, S., Liggitto, J., Liu, P., Anlauf, K., Leaitch, W., and Steffen, A.: Size-resolved  
778 aerosol chemistry on Whistler Mountain, Canada with a high-resolution aerosol mass spectrometer during INTEX-B, Atmos.  
779 Chem. Phys., 9, 3095-3111, doi:10.5194/acp-9-3095-2009, 2009.

780 Sun, Y. L., Zhang, Q., Schwab, J. J., Chen, W. N., Bae, M. S., Hung, H. M., Lin, Y. C., Ng, N. L., Jayne, J., Massoli, P., Williams,  
781 L. R., and Demerjian, K. L.: Characterization of near-highway submicron aerosols in New York City with a high-resolution  
782 aerosol mass spectrometer, Atmos. Chem. Phys., 12, 2215-2227, doi:10.5194/acp-12-2215-2012, 2012.

783 Sun, Y., Wang, Z., Fu, P., Jiang, Q., Yang, T., Li, J., and Ge, X.: The impact of relative humidity on aerosol composition and  
784 evolution processes during wintertime in Beijing, China, Atmos. Environ., 77, 927-934, doi:10.1016/j.atmosenv.2013.06.019,  
785 2013.

786 Sun, Y., Du, W., Fu, P., Wang, Q., Li, J., Ge, X., Zhang, Q., Zhu, C., Ren, L., Xu, W., Zhao, J., Han, T., Worsnop, D. R., and  
787 Wang, Z.: Primary and secondary aerosols in Beijing in winter: sources, variations and processes, Atmos. Chem. Phys., 16,  
788 8309-8329, doi:10.5194/acp-16-8309-2016, 2016.

789 Takami, A., Miyoshi, T., Shimono, A., and Hatakeyama, S.: Chemical composition of fine aerosol measured by AMS at Fukue  
790 Island, Japan during APEX period, Atmos. Environ., 39, 4913-4924, doi:10.1016/j.atmosenv.2005.04.038, 2005.

791 Ulbrich, I. M., Canagaratna, M. R., Zhang, Q., Worsnop, D. R., and Jimenez, J. L.: Interpretation of organic components from  
792 Positive Matrix Factorization of aerosol mass spectrometric data, Atmos. Chem. Phys., 9, 2891-2918, doi:10.5194/acp-9-2891-  
793 2009, 2009.

794 Wan, X., Kang, S., Li, Q., Rupakheti, D., Zhang, Q., Guo, J., Chen, P., Tripathi, L., Rupakheti, M., Panday, A. K., Wang, W.,  
795 Kawamura, K., Gao, S., Wu, G., and Cong, Z.: Organic molecular tracers in the atmospheric aerosols from Lumbini, Nepal, in  
796 the northern Indo-Gangetic Plain: influence of biomass burning, Atmos. Chem. Phys., 17, 8867-8885, doi:10.5194/acp-17-  
797 8867-2017, 2017.

798 Wang, J., Ge, X., Chen, Y., Shen, Y., Zhang, Q., Sun, Y., Xu, J., Ge, S., Yu, H., and Chen, M.: Highly time-resolved urban aerosol  
799 characteristics during springtime in Yangtze River Delta, China: insights from soot particle aerosol mass spectrometry, Atmos.

800 Chem. Phys., 16, 9109-9127, doi:10.5194/acp-16-9109-2016, 2016a.

801 Wang, J., Onasch, T. B., Ge, X., Collier, S., Zhang, Q., Sun, Y., Yu, H., Chen, M., Prévôt, A. S. H., and Worsnop, D. R.:  
802 Observation of Fullerene Soot in Eastern China, *Environ. Sci. Technol. Lett.*, 3, 121-126, doi:10.1021/acs.estlett.6b00044,  
803 2016b.

804 Wang, J., Zhang, Q., Chen, M., Collier, S., Zhou, S., Ge, X., Xu, J., Shi, J., Xie, C., Hu, J., Ge, S., Sun, Y., and Coe, H.: First  
805 Chemical Characterization of Refractory Black Carbon Aerosols and Associated Coatings over the Tibetan Plateau (4730 m  
806 a.s.l), *Environ. Sci. Technol.*, 51, 14072-14082, doi:10.1021/acs.est.7b03973, 2017.

807 Wang, Y., Hu, M., Lin, P., Guo, Q., Wu, Z., Li, M., Zeng, L., Song, Y., Zeng, L., Wu, Y., Guo, S., Huang, X., and He, L.:  
808 Molecular Characterization of Nitrogen-Containing Organic Compounds in Humic-like Substances Emitted from Straw  
809 Residue Burning, *Environ. Sci. Technol.*, 51, 5951-5961, doi:10.1021/acs.est.7b00248, 2017.

810 Wu, G., Liu, Y., Zhang, Q., Duan, A., Wang, T., Wan, R., Liu, X., Li, W., Wang, Z., and Liang, X.: The Influence of Mechanical  
811 and Thermal Forcing by the Tibetan Plateau on Asian Climate, *Journal of Hydrometeorology*, 8, 770-789,  
812 doi:10.1175/jhm609.1, 2007.

813 Xia, X., Zong, X., Cong, Z., Chen, H., Kang, S., and Wang, P.: Baseline continental aerosol over the central Tibetan plateau and a  
814 case study of aerosol transport from South Asia, *Atmos. Environ.*, 45, 7370-7378, doi:10.1016/j.atmosenv.2011.07.067, 2011.

815 Xu, B., Cao, J., Hansen, J., Yao, T., Joswita, D. R., Wang, N., Wu, G., Wang, M., Zhao, H., Yang, W., Liu, X., and He, J.: Black  
816 soot and the survival of Tibetan glaciers, *Proc. Natl. Acad. Sci. USA*, 106, 22114-22118, doi:10.1073/pnas.0910444106, 2009.

817 Xu, J., Zhang, Q., Chen, M., Ge, X., Ren, J., and Qin, D.: Chemical composition, sources, and processes of urban aerosols during  
818 summertime in northwest China: insights from high-resolution aerosol mass spectrometry, *Atmos. Chem. Phys.*, 14, 12593-  
819 12611, doi:10.5194/acp-14-12593-2014, 2014.

820 Xu, J., Shi, J., Zhang, Q., Ge, X., Canonaco, F., Prévôt, A. S. H., Vonwiller, M., Szidat, S., Ge, J., Ma, J., An, Y., Kang, S., and  
821 Qin, D.: Wintertime organic and inorganic aerosols in Lanzhou, China: sources, processes, and comparison with the results  
822 during summer, *Atmos. Chem. Phys.*, 16, 14937-14957, doi:10.5194/acp-16-14937-2016, 2016.

823 Xu, J., Zhang, Q., Shi, J., Ge, X., Xie, C., Wang, J., Kang, S., Zhang, R., and Wang, Y.: Chemical characteristics of submicron  
824 particles at the central Tibet Plateau: influence of long-range transport, *Atmos. Chem. Phys. Discuss.*, 1-32, doi:10.5194/acp-  
825 2017-587, 2017.

826 Xu, L., Suresh, S., Guo, H., Weber, R. J., and Ng, N. L.: Aerosol characterization over the southeastern United States using high-  
827 resolution aerosol mass spectrometry: spatial and seasonal variation of aerosol composition and sources with a focus on  
828 organic nitrates, *Atmos. Chem. Phys.*, 15, 7307-7336, doi:10.5194/acp-15-7307-2015, 2015.

829 Yadav, I. C., Devi, N. L., Li, J., Syed, J. H., Zhang, G., and Watanabe, H.: Biomass burning in Indo-China peninsula and its  
830 impacts on regional air quality and global climate change-a review, *Environmental pollution*, 227, 414-427,  
831 doi:10.1016/j.envpol.2017.04.085, 2017.

832 Yang, K., Wu, H., Qin, J., Lin, C., Tang, W., and Chen, Y.: Recent climate changes over the Tibetan Plateau and their impacts on  
833 energy and water cycle: A review, *Global and Planetary Change*, 112, 79-91, doi:10.1016/j.gloplacha.2013.12.001, 2014.

834 Yao, T., Thompson, L., Mosbrugger, V., Zhang, F., Ma, Y., Luo, T., Xu, B., Yang, X., Joswiak, D. R., Wang, W., Joswiak, M. E.,  
835 Devkota, L. P., Tayal, S., Jilani, R., and Fayziev, R.: Third Pole Environment (TPE), *Environmental Development*, 3, 52-64,  
836 doi:10.1016/j.envdev.2012.04.002, 2012a.

837 Yao, T., Thompson, L., Yang, W., Yu, W., Gao, Y., Guo, X., Yang, X., Duan, K., Zhao, H., Xu, B., Pu, J., Lu, A., Xiang, Y., Kattel,  
838 D. B., and Joswiak, D.: Different glacier status with atmospheric circulations in Tibetan Plateau and surroundings, *Nature Clim.  
839 Change*, 2, 663-667, doi:10.1038/nclimate1580, 2012b.

840 Zhang, Q., Alfarra, M. R., Worsnop, D. R., Allan, J. D., Coe, H., Canagaratna, M. R., and Jimenez, J. L.: Deconvolution and  
841 quantification of hydrocarbon-like and oxygenated organic aerosols based on aerosol mass spectrometry, *Environ. Sci.  
842 Technol.*, 39, 4938-4952, doi:10.1021/es048568l, 2005a.

843 Zhang, Q., Canagaratna, M. R., Jayne, J. T., Worsnop, D. R., and Jimenez, J. L.: Time- and size-resolved chemical composition  
844 of submicron particles in Pittsburgh: Implications for aerosol sources and processes, *J. Geophys. Res.*, 110,  
845 doi:10.1029/2004jd004649, 2005b.

846 Zhang, Q., Jimenez, J. L., Canagaratna, M. R., Allan, J. D., Coe, H., Ulbrich, I., Alfarra, M. R., Takami, A., Middlebrook, A. M.,  
847 Sun, Y. L., Dzepina, K., Dunlea, E., Docherty, K., DeCarlo, P. F., Salcedo, D., Onasch, T., Jayne, J. T., Miyoshi, T., Shimo,  
848 A., Hatakeyama, S., Takegawa, N., Kondo, Y., Schneider, J., Drewnick, F., Borrmann, S., Weimer, S., Demerjian, K., Williams,  
849 P., Bower, K., Bahreini, R., Cottrell, L., Griffin, R. J., Rautiainen, J., Sun, J. Y., Zhang, Y. M., and Worsnop, D. R.: Ubiquity  
850 and dominance of oxygenated species in organic aerosols in anthropogenically-influenced Northern Hemisphere midlatitudes,  
851 *Geophys. Res. Lett.*, 34, doi:10.1029/2007gl029979, 2007a.

852 Zhang, Q., Jimenez, J. L., Worsnop, D. R., and Canagaratna, M.: A case study of urban particle acidity and its influence on  
853 secondary organic aerosol, *Environ. Sci. Technol.*, 41, 3213-3219, doi:10.1021/es061812j, 2007b.

854 Zhang, Q., Jimenez, J. L., Canagaratna, M. R., Ulbrich, I. M., Ng, N. L., Worsnop, D. R., and Sun, Y.: Understanding  
855 atmospheric organic aerosols via factor analysis of aerosol mass spectrometry: a review, *Anal. Bioanal. Chem.*, 401, 3045-  
856 3067, doi:10.1007/s00216-011-5355-y, 2011.

857 Zhang, R., Wang, Y., He, Q., Chen, L., Zhang, Y., Qu, H., Smeltzer, C., Li, J., Alvarado, L. M. A., Vrekoussis, M., Richter, A.,

858 Wittrock, F., and Burrows, J. P.: Enhanced trans-Himalaya pollution transport to the Tibetan Plateau by cut-off low systems,  
859 Atmos. Chem. Phys., 17, 3083-3095, doi:10.5194/acp-17-3083-2017, 2017a.

860 Zhang, X., Zhang, Y., Sun, J., Yu, Y., Canonaco, F., Prevot, A. S., and Li, G.: Chemical characterization of submicron aerosol  
861 particles during wintertime in a northwest city of China using an Aerodyne aerosol mass spectrometry, Environ. Pollut., 222,  
862 567-582, doi:10.1016/j.envpol.2016.11.012, 2017b.

863 Zhao, Z., Cao, J., Shen, Z., Xu, B., Zhu, C., Chen, L. W. A., Su, X., Liu, S., Han, Y., Wang, G., and Ho, K.: Aerosol particles at a  
864 high-altitude site on the Southeast Tibetan Plateau, China: Implications for pollution transport from South Asia, J. Geophys.  
865 Res.-Atmos., 118, 11360-11375, doi:10.1002/jgrd.50599, 2013.

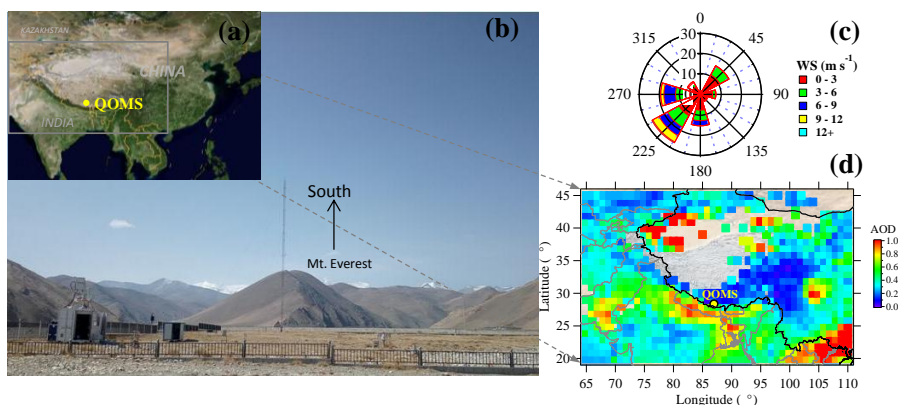
866 Zheng, J., Hu, M., Du, Z., Shang, D., Gong, Z., Qin, Y., Fang, J., Gu, F., Li, M., Peng, J., Li, J., Zhang, Y., Huang, X., He, L., Wu,  
867 Y., and Guo, S.: Influence of biomass burning from South Asia at a high-altitude mountain receptor site in China, Atmos.  
868 Chem. Phys., 17, 6853-6864, doi:10.5194/acp-17-6853-2017, 2017.

869 Zhou, S., Collier, S., Jaffe, D. A., Briggs, N. L., Hee, J., Sedlacek Iii, A. J., Kleinman, L., Onasch, T. B., and Zhang, Q.: Regional  
870 influence of wildfires on aerosol chemistry in the western US and insights into atmospheric aging of biomass burning organic  
871 aerosol, Atmos. Chem. Phys., 17, 2477-2493, doi:10.5194/acp-17-2477-2017, 2017.

872 Zhu, Q., He, L. Y., Huang, X. F., Cao, L. M., Gong, Z. H., Wang, C., Zhuang, X., and Hu, M.: Atmospheric aerosol compositions  
873 and sources at two national background sites in northern and southern China, Atmos. Chem. Phys., 16, 10283-10297,  
874 doi:10.5194/acp-16-10283-2016, 2016.

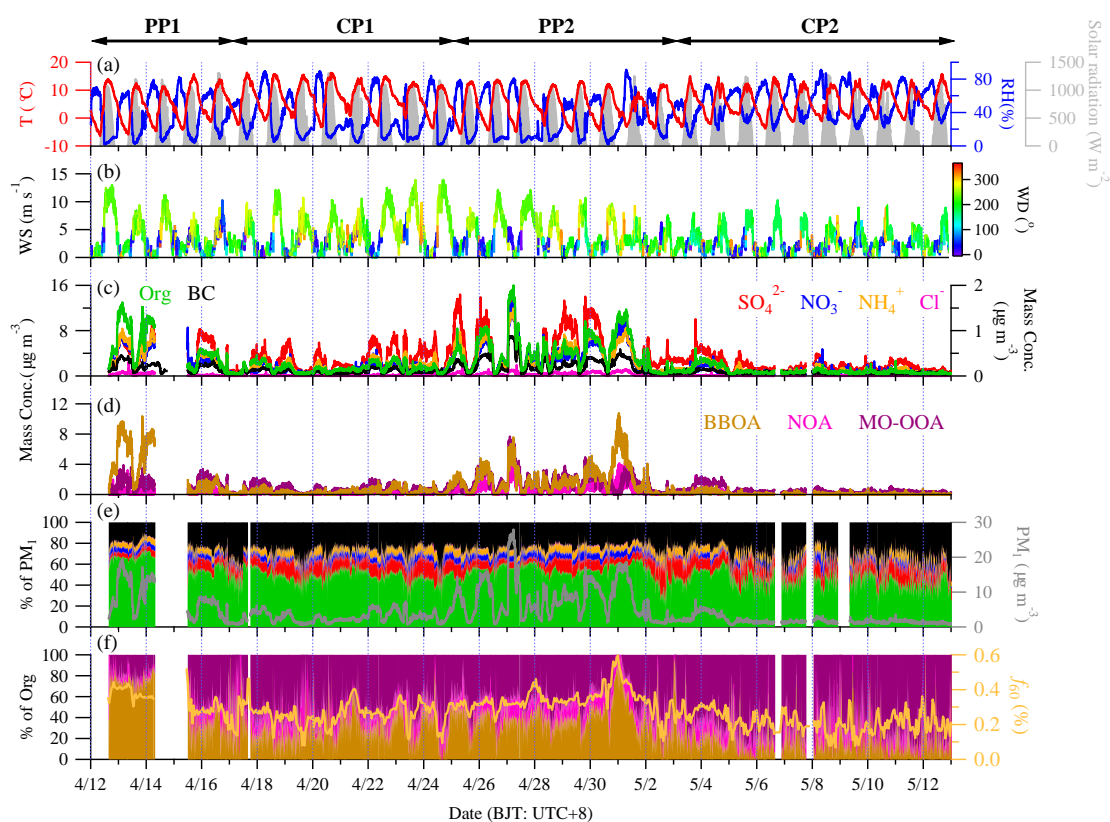
875 Zou, H., Zhou, L., Ma, S., Li, P., Wang, W., Li, A., Jia, J., and Gao, D.: Local wind system in the Rongbuk Valley on the northern  
876 slope of Mt. Everest, Geophys. Res. Lett., 35, doi:10.1029/2008gl033466, 2008.

877



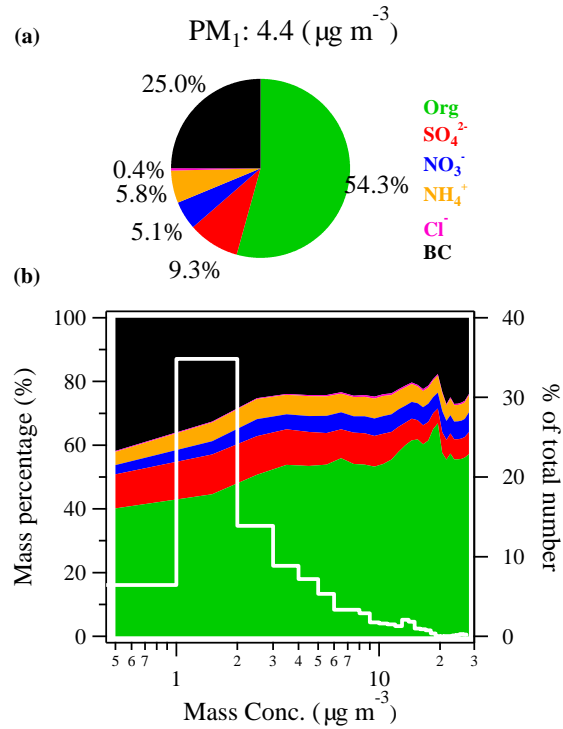
878  
879  
880  
881

**Figure 1.** (a) Location map for the QOMS, (b) picture for the QOMS and its surrounding, (c) wind rose plot colored by wind speed in this study, and (d) distribution of the average aerosol optical depth (AOD) around the QOMS retrieved from Terra MODIS at 550 nm during this study.



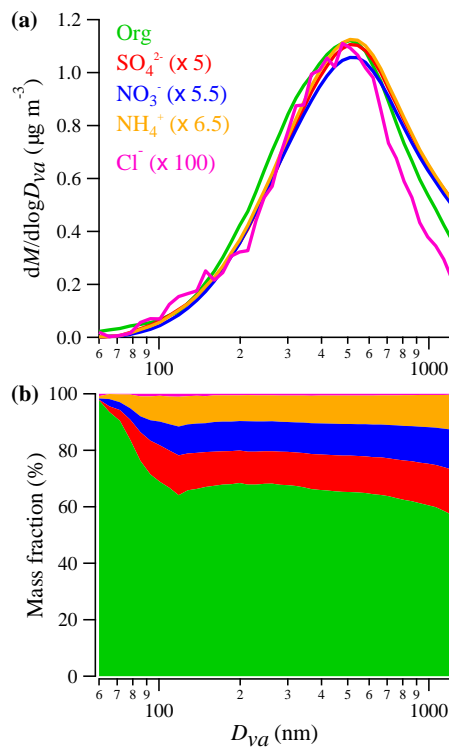
882  
883  
884  
885  
886  
887  
888

**Figure 2.** Summary of meteorological and HR-ToF-AMS data. The 5-min time series of (a) ambient temperature ( $T$ ), relative humidity (RH), and solar radiation, (b) wind speed (WS) colored by wind direction (WD), (c) mass concentrations of  $PM_{10}$  species, (d) mass concentrations of organic components, (e) mass contributions of  $PM_{10}$  species to total  $PM_{10}$  as well as total  $PM_{10}$  mass concentrations, and (f) mass contributions of organic components to organics. The time series of hourly average  $f_{60}$  ( $= C_2H_4O_2^+ / OA$ ) values for the entire period is also showed. The markers of PP1 and PP2 represent the two polluted periods while CP1 and CP2 are clear periods, respectively.



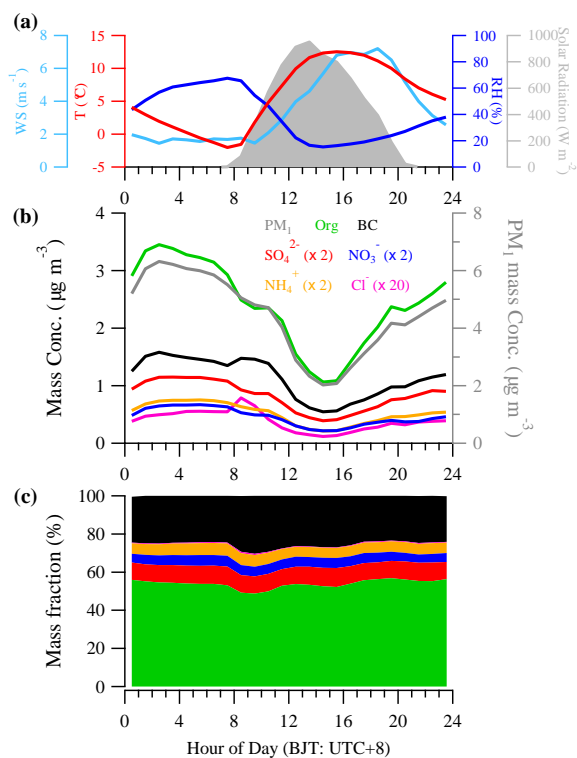
889  
890  
891  
892

**Figure 3.** The average mass contributions of PM<sub>1</sub> (= NR-PM<sub>1</sub>+ BC) species (a) during the entire sampling period and (b) as a function of the total PM<sub>1</sub> mass concentrations. The white solid line in (b) shows the percentage of the data number in each mass bins to the total data number.

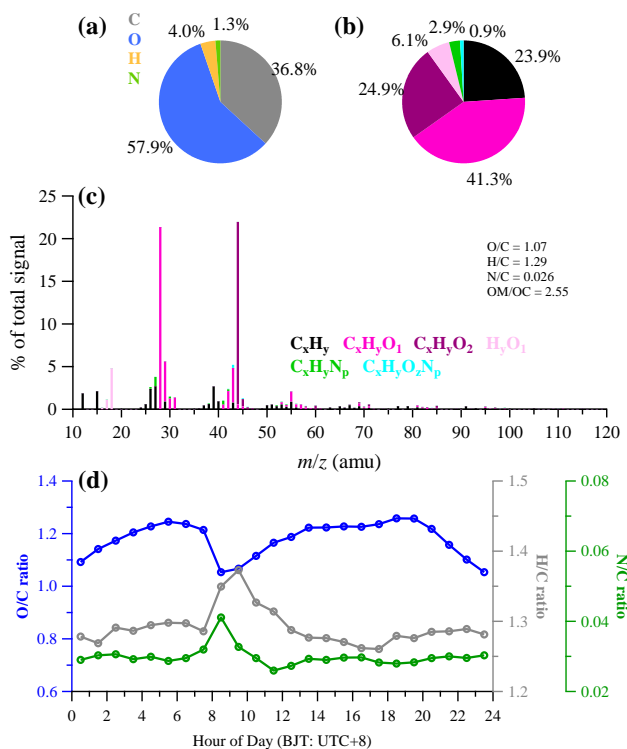


893  
894  
895

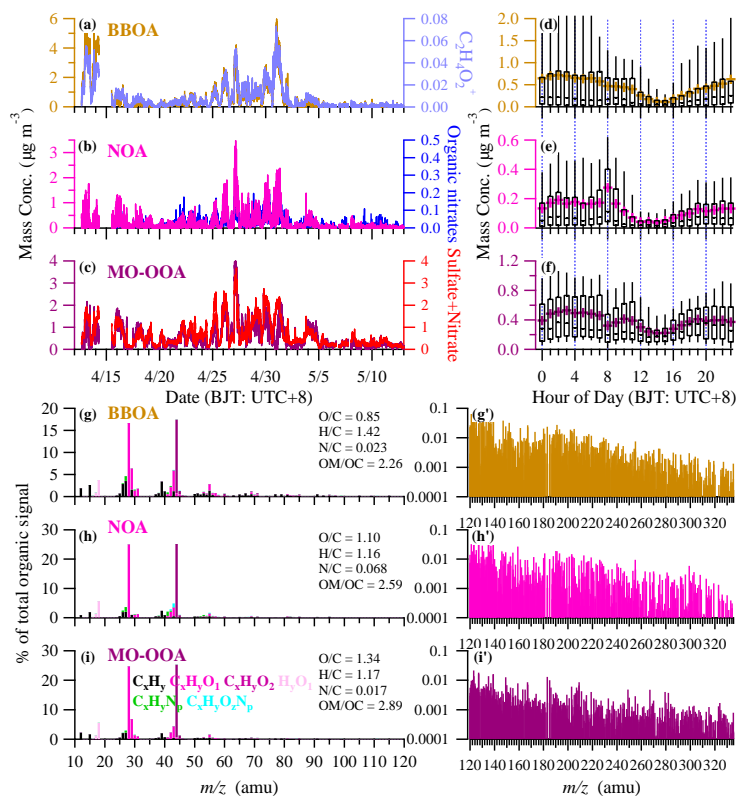
**Figure 4.** The average size distributions of (a) mass concentrations and (b) mass contributions of NR-PM<sub>1</sub> species for the entire study.



896  
897 **Figure 5.** The diurnal cycles of (a) meteorological parameters (temperature, RH, wind speed, and solar radiation), (b) mass  
898 concentrations and (c) mass contributions of PM<sub>1</sub> chemical species for the entire study.

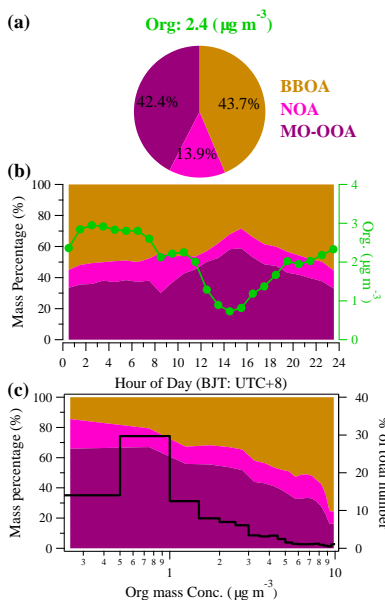


899  
900 **Figure 6.** The average contributions of (a) four elements (C, O, H, and N) and (b) six ion categories (colors as in (c)) to OA for  
901 the entire study; (c) the average high-resolution mass spectrum of OA (colors show six ion categories); (d) the diurnal variations  
902 of O/C, H/C, and N/C ratios.



903  
904  
905  
906  
907  
908

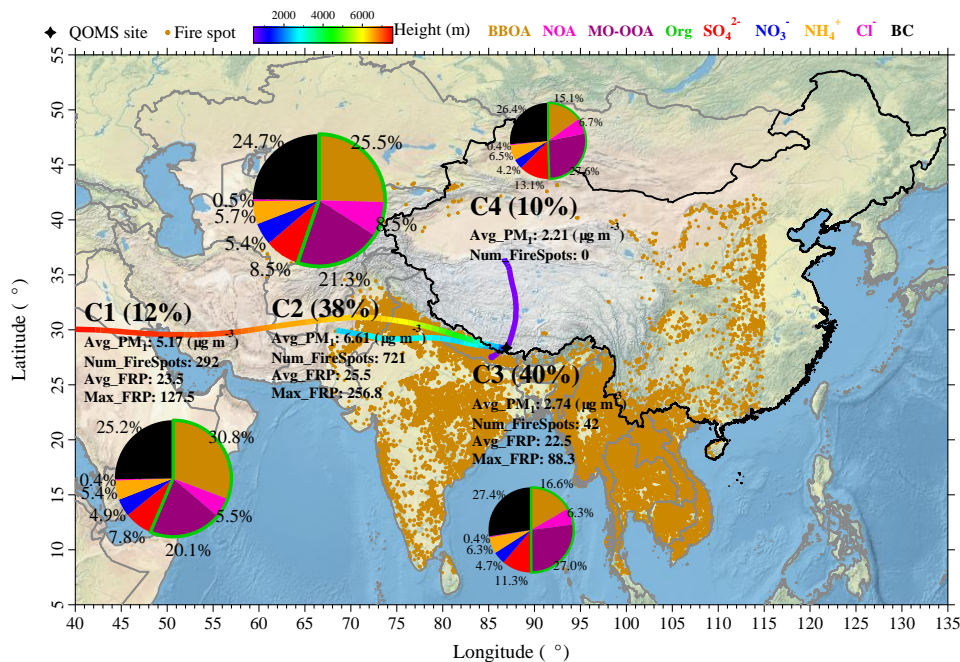
**Figure 7.** The PMF results of (a–c) the time series of three OA factors and corresponding tracer species, (d–f) the diurnal variations of the mass concentrations of the three OA factors (the whiskers above and below the boxes indicate the 90th and 10th percentiles, the upper and lower boundaries respectively indicate the 75th and 25th percentiles, the lines in the boxes indicate the median values, and the cross symbols indicate the mean values), (g–i) high-resolution mass spectra of the three OA factors colored by six ion families at  $m/z < 120$ , and (g'–i') the unit resolution mass spectra at  $m/z > 120$  for each OA factor.



909  
910  
911  
912  
913

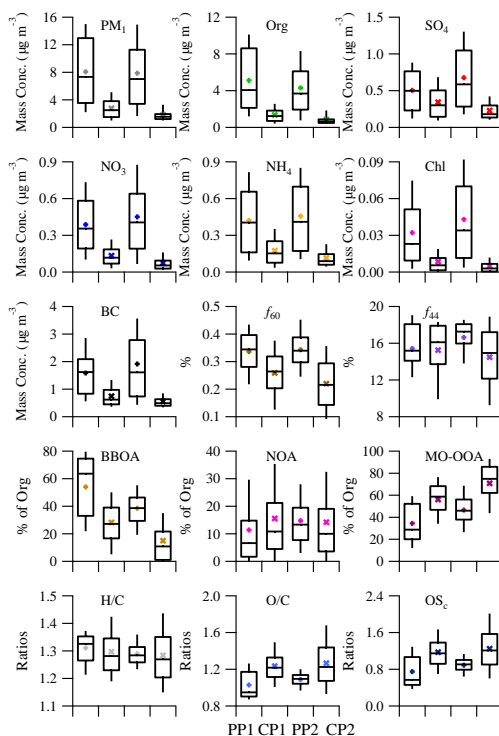
**Figure 8.** (a) The average mass concentration of OA and mass contributions of three OA factors to total OA; (b) the diurnal variations of mass contributions of three OA factors to total OA and the total OA mass concentration; (c) The average mass contributions of three OA factors as a function of total OA mass concentrations. The black solid line in (c) shows the percentage of the data number in each OA mass bins to the total data number.





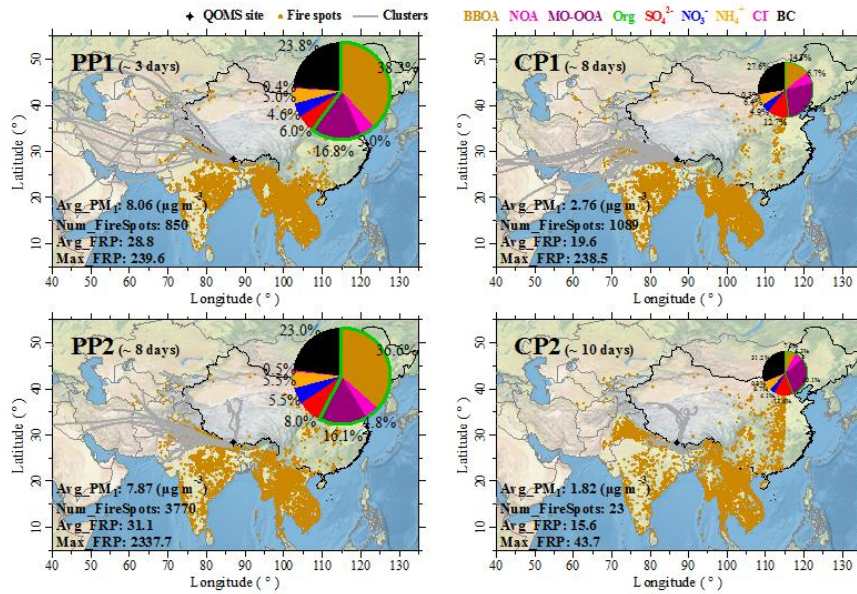
914  
915  
916  
917  
918

**Figure 9.** The average back trajectory clusters during the entire study and the corresponding mass contributions of PM<sub>1</sub> species and OA factors to the total PM<sub>1</sub> mass. The areas of each pie charts are scaled by the corresponding average PM<sub>1</sub> mass concentrations. The average PM<sub>1</sub> mass concentrations, number of fire hotspots as well as the average and maximum fire radiative powers (FRP) belong to each clusters during the entire measurement period are also given.



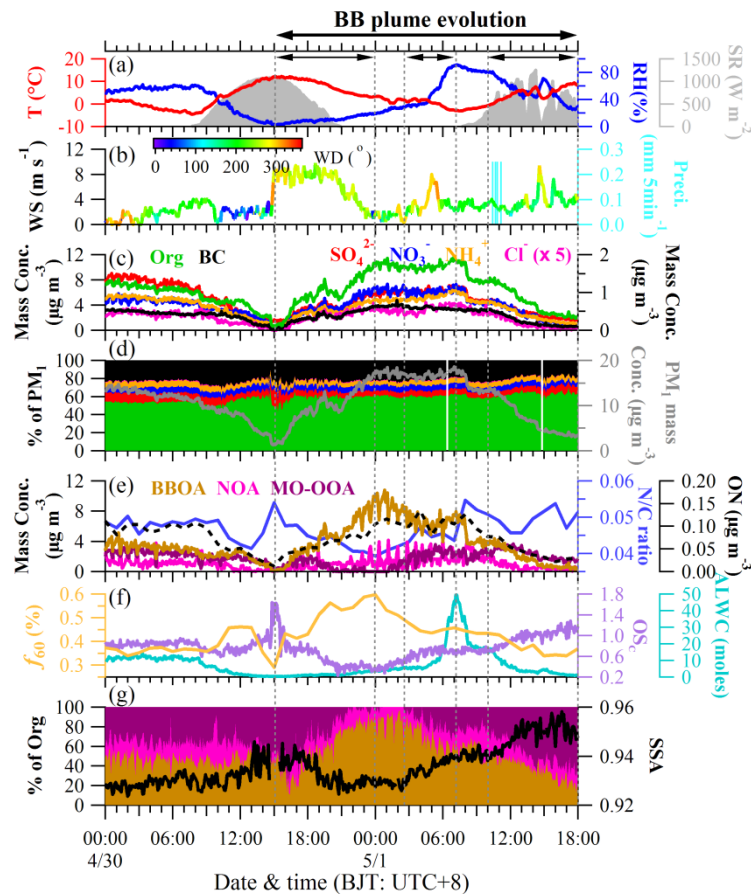
919  
920  
921  
922  
923

**Figure 10.** Box plots of mass concentrations of total PM<sub>1</sub> and its species, *f*<sub>60</sub> and *f*<sub>44</sub> values, mass contribution of three OA components to organics, element ratios (H/C and O/C), and carbon oxidation states (OS<sub>c</sub>) among the four polluted and clear periods. The whiskers indicate the 90th and 10th percentiles, the upper and lower boundaries of boxes indicate the 75th and 25th percentiles, the lines in the boxes indicate the median values, and the markers indicate the mean values.



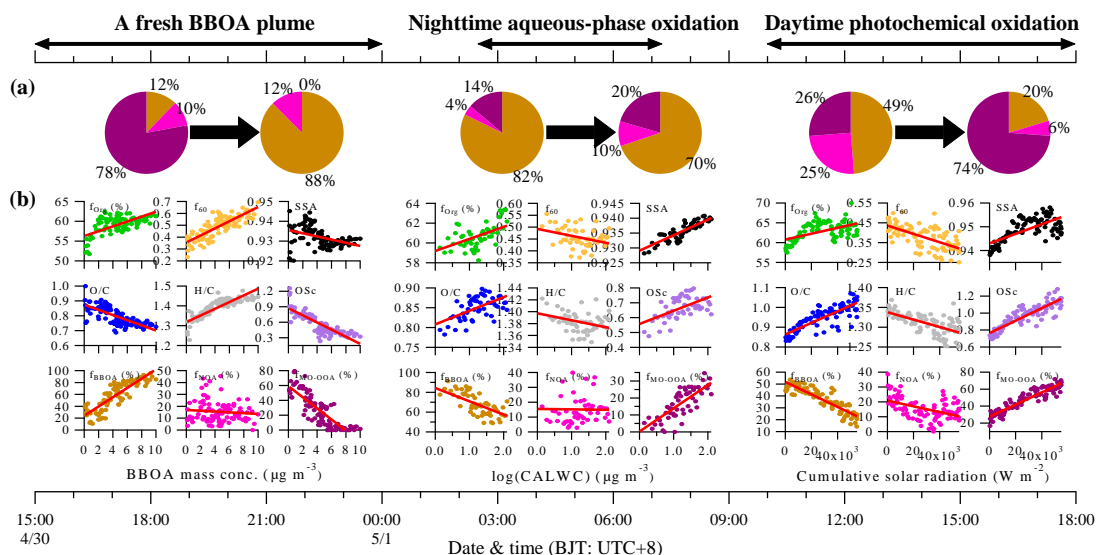
924  
925  
926  
927  
928

**Figure 11.** The 72-h back trajectories (grey solid lines) calculated every 6 h for the different episodes. Pie charts show the average mass contributions of PM<sub>1</sub> species and OA factors to the total PM<sub>1</sub> mass for each episodes (scaled by the corresponding average PM<sub>1</sub> mass concentrations). The average PM<sub>1</sub> mass concentrations, number of fire hotspots as well as the average and maximum fire radiative powers (FRP) belong to all trajectories for the different episodes are also given.



929  
930  
931  
932

**Figure 12.** The temporal variations of meteorological parameters, mass concentrations and mass contributions of each PM<sub>1</sub> species and OA components as well as the N/C ratio,  $f_{60}$  values, carbon oxidation states (OS<sub>c</sub>), aerosol liquid water content (ALWC) and single scattering albedo (SSA) for the case study period from April 30 at 00:00 to May 1 at 18:00.



933  
 934  
 935  
 936  
 937  
 938

**Figure 13.** Case study of chemical evolution of BB plume from April 30 at 15:00 to May 1 at 18:00. The periods marked with arrows are three distinct evolution processes. Pie charts in (a) are the mass contributions of three OA factors to total OA during the beginning and end time for each process, respectively. The scattering plots in (b) are the aerosol chemistry parameters as a function of BBOA mass concentration, logarithmic values of cumulative aerosol liquid water content (CALWC), and cumulative solar radiation for the corresponding process.

# 1 Chemical characterization of long-range transport biomass burning 2 emissions to the Himalayas: insights from high-resolution aerosol 3 mass spectrometry

4 Xinghua Zhang<sup>1,2,3</sup>, Jianzhong Xu<sup>1</sup>, Shichang Kang<sup>1</sup>, Yanmei Liu<sup>1,3</sup>, Qi Zhang<sup>4</sup>

5 <sup>1</sup>State Key Laboratory of Cryospheric Sciences, Northwest Institute of Eco-Environment and  
6 Resources, Chinese Academy of Sciences, Lanzhou 730000, China

7 <sup>2</sup>Key Laboratory of Arid Climatic Change and Reducing Disaster of Gansu Province, Key  
8 Laboratory of Arid Climatic Change and Disaster Reduction of CMA, Institute of Arid  
9 Meteorology, China Meteorological Administration, Lanzhou 730020, China

10 <sup>3</sup>University of Chinese Academy of Sciences, Beijing 100049, China

11 <sup>4</sup>Department of Environmental Toxicology, University of California, Davis, CA 95616, USA

12 Correspondence to: Jianzhong Xu (jzxu@lzb.ac.cn)

## 13 Abstract

14 An intensive field measurement was conducted at a remote, background, and high-altitude site  
15 (Qomolangma station, QOMS, 4276 m a.s.l.) in the northern Himalayas, using an Aerodyne high-  
16 resolution time-of-flight aerosol mass spectrometer (HR-ToF-AMS) along with other collocated  
17 instruments. The field measurement was performed from April 12 to May 12, 2016 to chemically  
18 characterize the high time-resolved submicron particulate matter (PM<sub>1</sub>) and obtain the dynamic  
19 processes (emissions, transport, and chemical evolution) of biomass burning (BB), frequently  
20 transported from South Asia to the Himalayas during pre-monsoon season. Overall, the average ( $\pm$   
21  $1\sigma$ ) PM<sub>1</sub> mass concentration was 4.44 ( $\pm$ 4.54)  $\mu\text{g m}^{-3}$  for the entire study, comparable with those  
22 observed at other remote sites worldwide. Organic aerosol (OA) was the dominant PM<sub>1</sub> species  
23 (accounting for 54.3% of total PM<sub>1</sub> on average) followed by black carbon (BC) (25.0%), sulfate  
24 (9.3%), ammonium (5.8%), nitrate (5.1%), and chloride (0.4%). The average size distributions of  
25 PM<sub>1</sub> species all peaked at an overlapping accumulation mode ( $\sim$  500 nm), suggesting that aerosol  
26 particles were internally well-mixed and aged during long-range transport. Positive matrix  
27 factorization (PMF) analysis on the high-resolution organic mass spectra identified three distinct  
28 OA factors, including a BB-related OA (BBOA, 43.7%), a nitrogen-containing OA (NOA, 13.9%)  
29 and a more-oxidized oxygenated OA (MO-OOA, 42.4%). Two polluted episodes with enhanced  
30 PM<sub>1</sub> mass loadings and elevated BBOA contributions from the west and southwest of QOMS  
31 during the study were observed. A typical BB plume was investigated in detail to illustrate the  
32 chemical evolution of aerosol characteristics under distinct air mass origins, meteorological  
33 conditions and atmospheric oxidation processes.

## 34 1 Introduction

35 The Tibetan Plateau and Himalayas (TPH), generally called the “third pole”, is the highest  
36 (average altitude of more than 4000 m a.s.l.) and largest ( $\sim$  2 500 000 km<sup>2</sup>) plateau in the world.  
37 This region has been recognized as one of the most pristine region in the world due to its high  
38 altitude, sparse population and minor influence of anthropogenic activities (Yao et al., 2012a).

删除的内容: ation

删除的内容: (~

41 Consideration on the intense dynamical and thermal forcing effects, the TPH not only plays a key  
42 role in the formation of Asian monsoon systems, but also impacts the large-scale atmospheric  
43 circulation, hydrological cycle, as well as global climate (Duan and Wu, 2005; Wu et al., 2007).

44 Over the past decades, more attentions have been paid to the environment and climate change in  
45 the TPH since this region is very susceptibility to the global climate change such as fast air  
46 temperature rise and dramatic glacier shrinkage (Xu et al., 2009; Kang et al., 2010; Yao et al.,  
47 2012b; Yang et al., 2014). Atmospheric environment in the TPH, albeit which is one of the most  
48 pristine region in the world, has been thought to be influenced variably due to the worse air  
49 pollution in its surrounding countries (Hou et al., 2003; Lau et al., 2008). For example, polluted air  
50 mass, particularly from South and Southeast Asia regions, had been observed frequently to  
51 transport to the Himalayas (Bonasoni et al., 2010; Cong et al., 2015), heat the aloft air masses over  
52 the TPH (Lau et al., 2006; Ramanathan and Carmichael, 2008) and decline the surface albedo after  
53 its deposition onto snow and glacier (Xu et al., 2009). As a consequence, characterizing the  
54 aerosol physicochemical properties in the TPH, including mass loading, chemical composition,  
55 size distribution and source, are of great importance to better understand the aerosol chemistry,  
56 estimate the aerosol radiative forcing, and finally evaluate the effect of polluted air mass on the  
57 ecology and environment in the TPH region.

58 Numerous aerosol measurements have been conducted in the TPH region in past decades to  
59 characterize the physicochemical properties, sources and transport pathways of ambient aerosol  
60 (Liu et al., 2008; Decesari et al., 2010; Marcq et al., 2010; Marinoni et al., 2013; Putero et al.,  
61 2014; Xu et al., 2017; Zhang et al., 2017a). South and Southeast Asia are two major polluted  
62 regions due to their intense biomass burning (BB) activities from natural forest fires and  
63 traditional human burning activities for residential heating and cooking (Engling et al., 2011;  
64 Yadav et al., 2017). The polluted feature of South and Southeast Asia during April 12 to May 12,  
65 2016 can be further revealed by the distribution of average aerosol optical depth in Fig. 1. During  
66 the pre-monsoon period, atmospheric pollutants associated with BB emissions in South Asia are  
67 generally advected by regional and long-range transport (e.g., westerlies and South Asian  
68 monsoon system) to Himalayas and built up in the southern foothills, then pollutants are lifted up  
69 to high altitude by the Himalayan topography and the typical valley wind circulation (Zhao et al.,  
70 2013; Cong et al., 2015; Liu et al., 2017). However, the chemical properties of aerosol particles  
71 are still not well understood and limited in the Himalayas region due to its remote and harsh  
72 environments, challenging weather conditions and logistic difficulties. In addition, most of the  
73 available studies are mainly based on the off-line filter sampling of ambient aerosol or snow/ice  
74 samples following by laboratory analyses (Decesari et al., 2010; Ram et al., 2010; Li et al., 2016;  
75 Wan et al., 2017). These studies usually had a relatively low-time resolution (days to weeks).  
76 Therefore, real-time consecutive field measurement, especially focusing on the high-resolution  
77 size-resolved chemical characteristics of aerosol particles, is of great importance and necessary to  
78 give insight into the sources and the dynamic chemical evolution of ambient aerosol.

79 Online real-time instrument such as Aerodyne aerosol mass spectrometer (AMS), which can  
80 be used to characterize the chemical properties and sources of submicron aerosol particles with  
81 high time resolution and sensitivity, has been greatly developed and widely implemented  
82 worldwide (Canagaratna et al., 2007; Zhang et al., 2007a; Jimenez et al., 2009; Li et al., 2017).  
83 Although the deployments of the AMS in China have started since 2006, most of these studies in

删除的内容: focused on

删除的内容: region

删除的内容: they are

删除的内容: south

删除的内容: southeast

删除的内容: frequently

删除的内容: southeast

删除的内容: source

删除的内容: south

删除的内容: south

删除的内容: heavily

95 | China are conducted in urban areas, including Beijing–Tianjin–Hebei (Sun et al., 2013; Sun et al.,  
96 | 2016), Yangtze River Delta (Wang et al., 2016a; Wang et al., 2016b), Pearl River Delta regions  
97 | (Huang et al., 2011), and Lanzhou (Xu et al., 2014; Xu et al., 2016; Zhang et al., 2017b) as shown  
98 | in Fig. S1, whereas just few studies deployed in remote sites so far, such as Menyuan (Du et al.,  
99 | 2015), Mt. Yulong (Zheng et al., 2017), and Nam Co (Xu et al., 2017; Wang et al., 2017). In this  
100 | paper, an Aerodyne high-resolution time-of-flight mass spectrometer (HR-ToF-AMS) was  
101 | deployed at the Qomolangma Station for Atmospheric and Environmental Observation and  
102 | Research (QOMS) in the north slope of the Himalayas to fill the vacancy of real-time mass  
103 | spectrometer measurement at high elevation site and evaluate the significant impacts of BBs from  
104 | polluted areas in the South Asia on the TPH aerosol properties during the pre-monsoon season.  
105 | Here, we report an overview of the 5-min real-time chemical and physical characteristics of  
106 | submicron aerosols (PM<sub>1</sub>), including mass loading, composition, size distribution, acidity as well  
107 | as temporal and diurnal variations. The sources of organic aerosols (OA) are also investigated  
108 | using positive matrix factorization analysis on the high-resolution OA mass spectrum. BB  
109 | influence and chemical evolution of aerosols in polluted plume are examined via combining back  
110 | trajectory analysis of air masses and fire hotspots information, respectively.

刪除的內容: and

刪除的內容: south

## 111 | 2 Experimental methods

### 112 | 2.1 Sampling site

113 | The QOMS (28.36°N, 86.95°E, 4276 m a.s.l.; Fig. 1), which is located in the northern slope of  
114 | Mt. Everest (~ 30 km away), was established for atmospheric and environmental observation since  
115 | 2005 (Ma et al., 2008). The geomorphic and climate features around the QOMS are typical alpine  
116 | cold and arid areas covered by sandy soil with sparse vegetation. The QOMS is located in a long  
117 | river valley and isolated from residential areas due to its harsh environment with a small village  
118 | (with a population of ~ 300) to the south (~ 10 km). The closest town, Dingri County, is ~ 100 km  
119 | south from the QOMS. A freeway is located at the front of the QOMS for tourism with increased  
120 | tourist during summer. The measurements were conducted from April 12 to May 12, 2016. Since  
121 | this period was within the typical pre-monsoon season of the TPH, the large-scale atmospheric  
122 | circulation pattern was dominated by westerly or southwesterly winds with limited precipitation.  
123 | Owing to a distinct thermal forcing from the southern mountains and glaciers, the QOMS was  
124 | locally dominated by strongly mountain-valley circulation with down-slope wind prevailing  
125 | during the daytime, especially in the afternoon (Fig. 1c and S2) (Zou et al., 2008), which would  
126 | make the valley as an efficient channel for the down transport of air mass from high-altitude  
127 | troposphere.

刪除的內容: transportation

### 128 | 2.2 Instrumentation

129 | A suite of real-time instruments were co-located to measure the physiochemical properties of fine  
130 | particles at the QOMS, including an Aerodyne HR-ToF-AMS (Aerodyne Research Inc., Billerica,  
131 | MA, USA) for 5-min size-resolved chemical compositions (organics, sulfate, nitrate, ammonium,  
132 | and chloride) of non-refractory submicron particulate matter (NR-PM<sub>1</sub>), a scanning mobility  
133 | particle sizer (SMPS, model 3936, TSI Inc., Shoreview, MN, USA) for 5-min particle number  
134 | concentration and size distribution between 14.6 and 661.2 nm in mobility diameter ( $D_m$ ), and a  
135 | photoacoustic extinctions (PAX, DMT Inc., Boulder, CO, USA) for particle light absorption

139 and scattering coefficient ( $b_{\text{abs}}$  and  $b_{\text{scat}}$ ) at 405 nm and further deriving black carbon (BC) mass  
140 concentration. All instruments were placed in an air-conditioned room with temperature  
141 maintaining at  $\sim 20$  °C. Ambient aerosol particles were introduced through a 0.5 inch copper tube  
142 which stemmed out of the rooftop by about 1.5 m. A PM<sub>2.5</sub> cyclone (model URG-2000-30EH,  
143 URG Corp., Chapel Hill, NC, USA) was used in front of the sampling inlet for removing coarse  
144 particles with size cutoffs of 2.5  $\mu\text{m}$  in aerodynamic diameter ( $D_{\text{va}}$ ). A diffusion dryer was placed  
145 following the cyclone to dry the ambient air and eliminate potential humidity effect on particles.  
146 The total length of the sampling line was about 5 m and the retention time of particles was less  
147 than 2.5 s in the whole inlet. The total air flow rate from the sampling inlet was about 10 L min<sup>-1</sup>,  
148 with part of flow shared by the HR-ToF-AMS and the SMPS while the remaining flow exhausted  
149 by an external pump. The meteorology data including wind speed (WS), wind direction (WD),  
150 relative humidity (RH), temperature ( $T$ ), and solar radiation (SR) during this study were obtained  
151 from a Vantage Pro2 weather station (Davis Instruments Corp., Hayward, CA, USA). Note that all  
152 the date and time used in this study are reported in Beijing Time (BJT: UTC + 8 h).

## 153 **2.3 HR-ToF-AMS operation and data analysis**

### 154 **2.3.1 HR-ToF-AMS operation**

155 A detailed instrumental description of the Aerodyne HR-ToF-AMS can be found elsewhere  
156 (DeCarlo et al., 2006) and only a brief summary is provided here. Briefly, the HR-ToF-AMS  
157 consists of three main parts: an aerosol sampling inlet, a particle sizing vacuum chamber, and a  
158 particle composition detection section (Jimenez et al., 2003). Ambient particles are sampled into  
159 the instrument through a critical orifice (130  $\mu\text{m}$  in this study for enhancing the transmission  
160 efficiency at the high-altitude area) and focus into a concentrated and narrow beam through an  
161 aerodynamic lens. Then particles are accelerated into the sizing vacuum chamber and obtain  
162 different velocities for particles with different sizes due to the supersonic expansion induced by  
163 different pressure between the two chambers. Meanwhile, a mechanical chopper with two radial  
164 slits located 180 °apart is used to intercept the focused particle, and then the time of flight (P-ToF)  
165 from the chopper to the vaporizer is measured to obtain the aerodynamic size of particles. After  
166 passing through the sizing chamber, particles are directed onto a resistively heated surface ( $\sim$   
167 600 °C) under a high vacuum and ionized by a 70 eV electron impact, and finally detect by the  
168 high-resolution time-of-flight mass spectrometer. In this study, the HR-ToF-AMS was only  
169 toggled under the high sensitive V-mode (detection limits  $\sim 10$  ng m<sup>-3</sup>). Under the V-mode  
170 operation, the instrument also switched between the mass spectrum (MS) mode and the particle P-  
171 ToF mode every 15 s, spending 6 and 9 s on each, to obtain the mass concentrations and size  
172 distributions of the non-refractory species, respectively.

173 The HR-ToF-AMS was calibrated for ionization efficiency (IE) and particle sizing at the  
174 beginning, in the middle, and at the end of this study according to the standard protocols (Jayne et  
175 al., 2000). Both the calibrations of IE and particle sizing were performed using mono-dispersed  
176 ammonium nitrate particles with nominal diameters of 70–300 nm. Default relative ionization  
177 efficiency (RIE) values were assumed in this study as 1.1 for nitrate, 1.3 for chloride, and 1.4 for  
178 organics. The RIE values of 3.9 and 4.2 were used for ammonium based on the results of two IE  
179 calibrations at the beginning and in the middle of this study, while RIE values of 1.6 and 1.4 were  
180 determined similarly for sulfate by using mono-dispersed ammonium sulfate particles,

181 respectively.

### 182 2.3.2 HR-ToF-AMS data analysis

183 The mass concentrations and size distributions of NR-PM<sub>1</sub> species and the ion-speciated mass  
184 spectra, composition and elemental composition of organics were determined from the HR-ToF-  
185 AMS data by using the standard ToF-AMS analysis toolkit SQUIRREL (v1.56) and PIKA (v1.15c)  
186 modules written in Igor Pro (Wavemetrics Inc., Lake Oswego, OR, USA). An empirical particle  
187 collection efficiency (CE) of 0.5 was used to compensate for the incomplete transmission and  
188 detection of particles due to particle bouncing at the vaporizer and partial transmission through the  
189 aerodynamic lens, which has been widely used in field studies employing AMS with a dryer  
190 installed in front of the inlet (Xu et al., 2014; Xu et al., 2016). The elemental ratios of oxygen-to-  
191 carbon (O/C), hydrogen-to-carbon (H/C), nitrogen-to-carbon (N/C), and organic mass-to-organic  
192 carbon (OM/OC) for this study were determined using the “improved-ambient” method (referred  
193 as I-A method) (Canagaratna et al., 2015), which increased O/C on average by 34%, H/C on  
194 average by 15%, and OM/OC on average by 17% (Fig. S3) compared with those determined from  
195 the “Aiken ambient” method (referred as A-A method) (Aiken et al., 2008).

196 Positive matrix factorization (PMF) analysis using the PMF2.exe algorithm (v4.2) (Paatero  
197 and Tapper, 1994) in robust mode was conducted on the high resolution mass spectra (HRMS) to  
198 determine distinct OA components in this study. The analysis was performed using an Igor Pro-  
199 based PMF Evaluation Tool (PET, v2.03) (Ulbrich et al., 2009), downloaded from the webpage  
200 ([http://cires.colorado.edu/jimenez-group/wiki/index.php/PMF-AMS\\_Analysis\\_Guide](http://cires.colorado.edu/jimenez-group/wiki/index.php/PMF-AMS_Analysis_Guide)). The data  
201 and error matrices input into the PMF analysis were generated from analyzing the V-mode data via  
202 PIKA fitting. Detailed PMF analysis was thoroughly evaluated following the procedures  
203 summarized in Table 1 of Zhang et al. (2011). Isotopic ions were generally excluded and the four  
204 ions of O<sup>+</sup>, HO<sup>+</sup>, H<sub>2</sub>O<sup>+</sup>, and CO<sup>+</sup> were downweighted in PMF analysis, because they were  
205 determined according to the relationship with CO<sub>2</sub><sup>+</sup> signal (Ulbrich et al., 2009). The “bad” ions  
206 with *S/N* less than 0.2 were removed from the HRMS data and error matrices before PMF analysis,  
207 and “weak” ions with *S/N* between 0.2 and 2 were downweighted by increasing their errors. In  
208 addition, some runs with huge mass loading spikes were also removed from the data and error  
209 matrices. The detailed matrix preparation and data pretreatment can also refer to Xu et al. (2014).

210 A summary of key diagnostic plots of the PMF results for this study is presented in Fig. S4.  
211 Overall, the PMF solutions were investigated for 1 to 8 factors and for the rotational parameter  
212 (fPeak) varying from -1 to 1 with a step of 0.1. Besides examining the model residuals, scaled  
213 residuals, and the Q/Q<sub>exp</sub> contributions for each *m/z* and time following procedures detailed in  
214 Table 1 of Zhang et al. (2011), the optimum solution can also be evaluated via comparing the mass  
215 spectra of individual factors with reference spectra from specific sources or other ambient AMS  
216 measurements, comparing the time series of individual factors with the known external tracers,  
217 and analyzing the diurnal variations of individual factors. Finally, the 3-factor solution with fPeak  
218 = 0 was chosen in this work. The direct comparisons of the mass spectra, time series, and diurnal  
219 variations for 2-factor and 4-factor solution were also shown in Fig. S5 and S6, respectively. The  
220 2-factor solution does not resolve the small, yet distinct nitrogen-containing OA, while the 4-  
221 factor solution shows a splitting factor from the BB OA resolved in the 3-factor solution and  
222 seems just like a simple separation of the two BB polluted episodes.

删除的内容: The detailed

删除的内容: were

删除的内容: (see Fig. 2 and Sect. 3.4 for details)



## 227 2.4 Other relevant data

228 The Hybrid Single Particle Lagrangian Integrated Trajectory (HYSPPLIT4) model developed by  
229 the National Oceanic and Atmospheric Administration (NOAA) (Draxler and Rolph, 2003) was  
230 used to investigate the origins of air masses in this study, using the meteorological data from the  
231 NOAA Global Data Assimilation System (GDAS). The back trajectories were calculated every 6 h  
232 at an ending height of 500 m above ground level at the QOMS during the entire campaign, and  
233 then clustered them according to their similarity in spatial distribution. Finally, a four-cluster  
234 solution was adopted according to its small total spatial variance.

235 Aerosol optical depth (AOD) at 550 nm was derived from the observations made by National  
236 Aeronautics and Space Administration (NASA) Moderate Resolution Imaging Spectroradiometer  
237 (MODIS) onboard the Terra satellite. The distribution of average aerosol optical depth (AOD) in a  
238 large range areas (20°–45°N, 60°–110°E) around the TPH during the entire period of this study is  
239 given in Fig. 1d.

240 Various active fire hotspots were detected over South and Southeast Asia by the Fire  
241 Information for Resource Management System (FIRMS) provided by MODIS satellite  
242 (<https://firms.modaps.eosdis.nasa.gov>), demonstrating the possibility that active wildfires or BBs  
243 from South and Southeast Asia may have significant impacts on the air conditions in the TPH  
244 region.

245 The aerosol liquid water content (ALWC) was estimated with the Extended AIM (E-AIM)  
246 Aerosol Thermodynamics Model (<http://www.aim.env.uea.ac.uk/aim/aim.php>). The input data  
247 included the concentrations of sulfate, nitrate, ammonium, and chloride measured by the HR-ToF-  
248 AMS as well as the relative humidity (RH) and temperature of ambient air.

## 249 3 Results and discussion

### 250 3.1 Overview of the study

#### 251 3.1.1 Meteorological conditions

252 The measurement period in our study was within the typical pre-monsoon season of the TPH. The  
253 meteorological conditions were therefore characterized by a relatively cold, dry and windy  
254 weather, and the westerlies dominated the large-scale atmospheric circulation patterns with little  
255 precipitation, as displayed in Fig. 2. During the study, the averaged diurnal air temperature ranged  
256 from –2.0 to 12.5 °C with an average ( $\pm 1\sigma$ ) of 5.7 ( $\pm 5.0$ ) °C, and the RH ranged from 15.3 to  
257 67.5% with an average of  $39.8 \pm 18.8\%$ . Only two light precipitation events (1 and 0.5 mm d<sup>-1</sup>)  
258 occurred on 1 and 8 May, respectively. The WDs at QOMS were predominantly by southwesterly,  
259 which were mainly associated with the thermally driven mountain-valley winds and glacier winds  
260 (Zou et al., 2008). For the diurnal variation of wind conditions, a nearly calm wind period (hourly  
261 average WS less than 2 m s<sup>-1</sup>) was observed in the early morning time; after sunrise to noon time,  
262 there was a weak up-slope wind period (from the north); the diurnal wind cycles in the rest time  
263 were dominated by the down-slope wind (from the southwest) with the maximum value of hourly  
264 average WS up to 7 m s<sup>-1</sup> (Fig. 2b and S2).

#### 265 3.1.2 Inter-comparisons between different instruments

删除的内容: Air mass trajectories,  
aerosol optical depth, and fire  
hotspots

删除的内容: starting

删除的内容: site

删除的内容: south

删除的内容: southeast

删除的内容: potential

删除的内容: south

删除的内容: southeast

删除的内容: (Fig. 2a)

删除的内容: (Fig. 1c)

278 An inter-comparison of the total PM<sub>1</sub> (NR-PM<sub>1</sub> + BC) mass concentrations measured by the HR-  
279 ToF-AMS (CE = 0.5) and the PAX with particle volumes (assuming spherical particles)  
280 determined from the SMPS is shown in Fig. S7. Overall, the PM<sub>1</sub> mass is closely correlated ( $R^2 =$   
281 0.97) with that of SMPS particle volume during the entire campaign, with a linear regression slope  
282 of 2.86. This slope is significantly higher than the estimated average PM<sub>1</sub> density of 1.44 g cm<sup>-3</sup>,  
283 which is calculated based on the measured particle compositions in this study and the assumed  
284 particle densities of 1.2 for organics, 1.78 for (NH<sub>4</sub>)<sub>2</sub>SO<sub>4</sub>, 1.72 for NH<sub>4</sub>NO<sub>3</sub>, 1.52 for NH<sub>4</sub>Cl and  
285 1.8 g cm<sup>-3</sup> for BC (Zhang et al., 2005b; Xu et al., 2016). This discrepancy is likely introduced by  
286 various factors, including different transmission sizes between HR-ToF-AMS and SMPS (up to ~  
287 1.0 μm in  $D_{va}$  for AMS vs. limited size range of 14.6–661.2 nm in  $D_m$  for SMPS), rough  
288 calculation of PM<sub>1</sub> density using assumed composition densities and spherical shape without  
289 consideration the particle porosity, as well as the using of empirical and constant CE value of 0.5  
290 in this study. This phenomenon was also observed at other sites in previous studies (Ge et al., 2012;  
291 Huang et al., 2012; Xu et al., 2014; Du et al., 2015).

### 292 3.1.3 Mass concentration and chemical composition of PM<sub>1</sub>

293 As shown in Fig. 2, the mass concentrations of PM<sub>1</sub> and all PM<sub>1</sub> species, as well as their mass  
294 fractions in PM<sub>1</sub> varied dynamically throughout this study. Two polluted periods (PP1 and PP2)  
295 were identified according to their high PM<sub>1</sub> mass concentrations (daily average PM<sub>1</sub> mass is larger  
296 than 5 μg m<sup>-3</sup>), high contributions from BBOA and unique back trajectories. The rest periods  
297 characterized by low PM<sub>1</sub> mass concentrations were considered as clear periods (CPI and CP2).  
298 The 5-min total PM<sub>1</sub> mass concentration ranged from 0.18 to 27.97 μg m<sup>-3</sup> for the study, with an  
299 average ( $\pm 1\sigma$ ) value of 4.44  $\pm$  4.54 μg m<sup>-3</sup>. This average value was more than two times lower  
300 than most of the PM<sub>1</sub> mass concentrations measured with Aerodyne AMS or aerosol chemical  
301 speciation monitor (ACSM) instruments at various urban, suburban, rural or background sites in  
302 China (10.9–138.8 μg m<sup>-3</sup>) (Fig. S1), except slightly lower than that at Mt. Yulong (5.7 μg m<sup>-3</sup>)  
303 located at the southeastern edge of the TPH, whereas higher than that at Nam Co Station (2.0 μg  
304 m<sup>-3</sup>) located in the central of the TPH. Moreover, as shown in table S1, the PM<sub>1</sub> mass  
305 concentration in this study was also lower than those measured at the three remote island sites in  
306 Asia which were frequently influenced by outflow from China, Korea and Japan (i.e., 7.9 μg m<sup>-3</sup>  
307 for Okinawa island, 12.0 μg m<sup>-3</sup> for Fukue island in Japan, and 10.7 μg m<sup>-3</sup> for Jeju island in  
308 Korea) (Takami et al., 2005; Jimenez et al., 2009), as well as the PM<sub>1</sub> mass concentration (15.1 μg  
309 m<sup>-3</sup>) obtained at the Bachelor mountain in United States which was heavily impacted by wildfire  
310 smoke plumes (Zhou et al., 2017). However, it was higher than those reported at other coastal,  
311 high elevation, forest or remote background sites in North America and Europe (0.55–2.91 μg m<sup>-3</sup>)  
312 (Zhang et al., 2007a; Sun et al., 2009; Fröhlich et al., 2015). Although these measurements  
313 mentioned above were conducted at various sites worldwide during different seasons, these  
314 comparisons further demonstrate that QOMS is a typical high elevation and remote background  
315 site in Asia.

316 Overall, organics and BC were the two dominant PM<sub>1</sub> species (averagely contributed 54.3%  
317 and 25.0% to the total PM<sub>1</sub> mass, respectively) followed by sulfate (9.3%), ammonium (5.8%),  
318 nitrate (5.1%), and chloride (0.4%) (Fig. 3a). The high contributions of organics and BC at QOMS  
319 were significantly associated with the active BB emissions by long-range transport from polluted

删除的内容: much

删除的内容: .

删除的内容: which

删除的内容: on

删除的内容: southeastern edge and

删除的内容: . respectively

删除的内容: from

327 | [areas in South Asia](#), Organic compounds and BC have been revealed as two dominant components  
328 | of BB aerosols and generally used to identify BB events in previous studies (Bond et al., 2004;  
329 | Bougiatioti et al., 2014). [In addition, biomass burning at high elevation regions of Himalayas and](#)  
330 | [south Asia was more incomplete burning and could emit amount of BC](#). This conclusion can be  
331 | further revealed by their enhanced mass concentrations and contributions, especially for organics,  
332 | during the two distinct polluted episodes influenced by active BB plumes. Figure 3b showed the  
333 | mass contributions of PM<sub>1</sub> species as a function of total PM<sub>1</sub> mass concentrations. The PM<sub>1</sub> mass  
334 | loadings in this study were mostly below 6 μg m<sup>-3</sup> (accounted for ~ 77%); The mass contribution  
335 | of organics increased significantly with the increase of total PM<sub>1</sub> mass loading whereas the rest  
336 | species showed relatively stable or decrease trends, suggesting the dominant contributions of  
337 | organics in the polluted episodes at QOMS.

删除的内容: ation

删除的内容: (Fig. 2 and Sect. 3.4)

### 338 | 3.1.4 Acidity and size distributions of submicron aerosols

339 | To evaluate the bulk acidity of NR-PM<sub>1</sub> in this study, [we calculated the NH<sub>4</sub><sup>+</sup> concentration](#)  
340 | [\(NH<sub>4</sub><sup>+</sup><sub>calc</sub>\)](#) based on the mass concentrations of sulfate, nitrate and chloride measured by the HR-  
341 | ToF-AMS and assumed full neutralization of these anions by ammonium (Zhang et al., 2007b).  
342 | The scatter plot of the measured NH<sub>4</sub><sup>+</sup> (NH<sub>4</sub><sup>+</sup><sub>meas</sub>) concentration versus the NH<sub>4</sub><sup>+</sup><sub>calc</sub> concentration  
343 | for the entire campaign was shown in Fig. S7. A tight correlation ( $R^2 = 0.97$ ) existed between  
344 | NH<sub>4</sub><sup>+</sup><sub>meas</sub> and NH<sub>4</sub><sup>+</sup><sub>calc</sub> with a linear regression slope of 1.2, indicating that there were excess of  
345 | ammonium in the submicron particle. This slightly high NH<sub>4</sub><sup>+</sup><sub>meas</sub>/NH<sub>4</sub><sup>+</sup><sub>calc</sub> ratio was quite different  
346 | with those results from various urban and rural sites in China, where bulk aerosols were overall  
347 | neutralized or acidic due to the enrich gaseous precursors of SO<sub>2</sub> and NO<sub>x</sub> that could be further  
348 | oxidized to sulfate and nitrate (Sun et al., 2013; Xu et al., 2014; Du et al., 2015; Zhang et al.,  
349 | 2017b). The excess ammonium at QOMS might relate to the important contributions of organic  
350 | acids in this area (Cong et al., 2015), which could underestimate the NH<sub>4</sub><sup>+</sup><sub>calc</sub> due to the neglect of  
351 | organic acids in the ion-balance calculation, and the non-negligible contributions of nitrogen-  
352 | containing organic compounds to NH<sub>x</sub><sup>+</sup> which finally overestimated the NH<sub>4</sub><sup>+</sup><sub>meas</sub> (Sun et al., 2009;  
353 | Ge et al., 2012). As mentioned above, atmospheric aerosols in the TPH region were significantly  
354 | influenced by BB emissions from [South Asia](#) during the sampling periods. BBs would emit large  
355 | amounts of nitrogen-containing organic compounds (Fleming et al., 2017; Zhou et al., 2017) and  
356 | as discussed in section 3.2.

删除的内容: predicted

删除的内容: pred

删除的内容: concentration was  
calculated

删除的内容: pred

删除的内容: pred

删除的内容: pred

删除的内容: pred

删除的内容: south

357 | Figure 4 shows the average size distributions of NR-PM<sub>1</sub> species and their mass contributions  
358 | as the function of size distribution. Overall, all chemical species showed a nearly consistent but  
359 | narrow accumulation mode peaking at ~ 500 nm in  $D_{va}$ , indicating the well internal-mixed and  
360 | aged aerosol particles at QOMS. Ultrafine particles (particles with diameter less than 100 nm)  
361 | were dominated by organics (more than 70%), while the mass contributions of chemical species at  
362 | the major peak (~ 500 nm) were organics (~ 65%), sulfate (~ 13%), nitrate (~ 11%), ammonium  
363 | (~ 10%), and chloride (~ 1%). The contribution of organics decreased with the increase of size  
364 | mode, while the contributions of three major inorganic species (sulfate, nitrate and ammonium)  
365 | slightly increased with the increasing sizes (Fig. 4b).

### 366 | 3.1.5 Diurnal variations of chemical species

367 | The average diurnal cycles of meteorological parameters as well as the PM<sub>1</sub> species and their mass  
368 | fractions for the entire campaign were shown in Fig. 5. All PM<sub>1</sub> species presented a similar diurnal

380 pattern with lower concentrations in the daytime whereas higher concentrations in the nighttime.  
381 The mass concentrations reached the minimum values at around 15:00. This pattern was  
382 accompanied with the enhanced wind speed and the increased air temperature in the afternoon  
383 which could related with the dynamics of planetary boundary layer (PBL). After that, the mass  
384 concentrations began to build up and reached to high levels in the nighttime. Note that the mass  
385 concentrations of chloride and BC also existed a slight peak during the early morning, which  
386 corresponded with the calm wind conditions and the lowest air temperature of the day and could  
387 associated with the enhanced local emissions at QOMS in the morning. The diurnal cycles of mass  
388 contributions of each PM<sub>1</sub> species were relatively stable for the entire campaign, besides the slight  
389 increase of BC from 24% at ~ 08:00 to 30% at ~ 10:00. Overall, organics dominated PM<sub>1</sub>  
390 throughout the day (49–57%), followed by BC (23–30%), sulfate (9–10%), ammonium (5–6%),  
391 nitrate (4–6%), and chloride (0.3–0.8%).

### 392 3.2 Bulk characteristics of OA

393 Figure 6a and b showed the average mass contributions of the four elements and the six ion  
394 categories to total organics, respectively. The organic mass was on average composed of 36.8%  
395 carbon, 57.9% oxygen, 4.0% hydrogen, and 1.3% nitrogen. For ionic categories, C<sub>x</sub>H<sub>y</sub>O<sub>1</sub><sup>+</sup> ions  
396 dominated the total OA accounting for 41.3%, followed by C<sub>x</sub>H<sub>y</sub>O<sub>2</sub><sup>+</sup> (24.9%), C<sub>x</sub>H<sub>y</sub><sup>+</sup> (23.9%),  
397 H<sub>y</sub>O<sub>1</sub><sup>+</sup> (6.1%), C<sub>x</sub>H<sub>y</sub>N<sub>p</sub><sup>+</sup> (2.9%) and C<sub>x</sub>H<sub>y</sub>O<sub>z</sub>N<sub>p</sub><sup>+</sup> (0.9%). The contributions of oxygen and the two  
398 major oxygenated ion fragments (C<sub>x</sub>H<sub>y</sub>O<sub>z</sub><sup>+</sup> = C<sub>x</sub>H<sub>y</sub>O<sub>1</sub><sup>+</sup>+C<sub>x</sub>H<sub>y</sub>O<sub>2</sub><sup>+</sup>) at QOMS were quite higher than  
399 those obtained at other urban or rural sites in China, whereas carbon and C<sub>x</sub>H<sub>y</sub><sup>+</sup> ions had relative  
400 | lower contributions, e.g., 38% of C<sub>x</sub>H<sub>y</sub>O<sub>z</sub><sup>+</sup> and 21% of oxygen versus 56% of C<sub>x</sub>H<sub>y</sub><sup>+</sup> and 70% of  
401 carbon in urban Lanzhou (Xu et al., 2014), and 37.4% of C<sub>x</sub>H<sub>y</sub>O<sub>z</sub><sup>+</sup> versus 51.2% of C<sub>x</sub>H<sub>y</sub><sup>+</sup> in urban  
402 | Nanjing (Wang et al., 2016a), suggesting that OA at QOMS were highly aged. Correspondingly,  
403 the average high-resolution OA mass spectrum (Fig. 6c) also showed significantly high  
404 contribution (~ 25%) at *m/z* 44 signal (one of the most reliable marker of oxygenated OA)  
405 compared with other ion fragments, e.g., 5% at *m/z* 43 (indicator for less oxidized compounds),  
406 1.7% at *m/z* 55 (important COA fragment), and 0.4% at *m/z* 57 (tracer for traffic-related emission)  
407 (Alfarra et al., 2004; Zhang et al., 2005a). The average O/C ratio was 1.07 during this study, which  
408 was much higher than those observed at various urban and rural sites in China using the I-A  
409 method, e.g., 0.37 in Beijing (Sun et al., 2016), 0.36 in Lanzhou (Xu et al., 2016), 0.35 in Nanjing  
410 | (Wang et al., 2016a), and 0.65 in Ziyang (Hu et al., 2016)). Moreover, the average O/C ratio was  
411 even higher than that of 0.98 at the background site of Mt. Wuzhi in southern China (Zhu et al.,  
412 | 2016), indicating that OA at QOMS was more oxidized and aged during long-range transport. The  
413 average H/C, N/C and OM/OC ratios were on average 1.29, 0.026 and 2.55 in this study,  
414 determined a nominal chemical formula of OA as C<sub>1</sub>H<sub>1.29</sub>O<sub>1.07</sub>N<sub>0.026</sub>.

415 For the diurnal cycles, O/C ratio had two peaks in the early morning and late afternoon, likely  
416 related to the production of secondary organic aerosol (SOA) via aqueous-phase reactions or  
417 photochemical oxidation processes during these two periods. H/C and N/C ratios yet showed  
418 inverse diurnal cycles with that of O/C, namely peaked at around 08:00–10:00 in the morning.  
419 The Van Krevelen diagram (H/C versus O/C), which had been used widely to probe the oxidation  
420 reaction mechanisms for bulk OA (Heald et al., 2010), showed an apparent anticorrelation ( $R^2 =$   
421 | 0.57) with a slope of -0.48 at QOMS (Fig. S8). Ng et al. (2011b) have suggested that a slope of –

删除的内容: higher

删除的内容: transportation

删除的内容: S11

425 0.5 indicate a net change in chemical composition from the addition of both acid and  
426 alcohol/peroxide functional groups without fragmentation, and/or carboxylic acid groups with  
427 fragmentation.

### 428 3.3 Organic aerosol source apportionment

429 Source apportionment via PMF analysis on the high-resolution OA mass spectrum identified three  
430 distinct factors in this campaign according to their unique temporary variations, mass spectrum  
431 (MS) profiles, element ratios, correlations with tracers, and diurnal patterns, i.e., a BB-related OA  
432 (BBOA), a nitrogen-containing OA (NOA) and a more-oxidized oxygenated OA (MO-OOA).  
433 Detailed discussion on each factor is given in the following subsections.

#### 434 3.3.1 BBOA

435 Although significant high contribution at  $m/z$  44 (mostly  $\text{CO}_2^+$ ) was found in all of the three OA  
436 components, the BBOA MS was also characterized by contributions at  $m/z$  60 (mainly  $\text{C}_2\text{H}_4\text{O}_2^+$ )  
437 and tiny  $m/z$  73 (mainly  $\text{C}_3\text{H}_5\text{O}_2^+$ ) (Fig. 7g), which were generally regarded as well-known tracers  
438 for BB emissions (Alfarra et al., 2007). The average fraction of the signal at  $m/z$  60 (referred as  $f_{60}$ )  
439 in the BBOA mass spectrum was 0.61%, which was higher than the typical value of  $\sim 0.3\%$  in the  
440 absence of BB impacts (Cubison et al., 2011). The time series of BBOA correlated tightly with  
441 those of  $\text{C}_2\text{H}_4\text{O}_2^+$  ( $R^2 = 0.91$ ) and  $\text{C}_3\text{H}_5\text{O}_2^+$  ( $R^2 = 0.87$ ) as well as BC ( $R^2 = 0.72$ ) and nitrate ( $R^2 =$   
442  $0.75$ ) (Fig. 7a and Table S2). If ignoring the influence of high contribution at  $m/z$  44, the BBOA  
443 mass spectrum in this study correlated well ( $R^2 = 0.5\text{--}0.9$ ) with those BBOA mass spectrum  
444 identified at other sites worldwide (Ng et al., 2011a; Mohr et al., 2012; Saarikoski et al., 2012;  
445 Crippa et al., 2013; Crippa et al., 2014; Xu et al., 2016), as shown in Fig. S9. The average mass  
446 concentration of BBOA was  $1.05 \mu\text{g m}^{-3}$  for the entire study and contributed a large fraction  
447 (43.7%) of the total OA mass on average (Fig. 8a), indicating that BBOA was an important  
448 component of OA during the pre-monsoon season at the QOMS. The diurnal cycle of BBOA  
449 showed high concentrations during nighttime whereas relatively low concentrations during  
450 daytime (Fig. 7d). Correspondingly, the mass contributions of BBOA to total OA mass decreased  
451 distinctly from  $\sim 55\%$  at 00:00 to 28% at 15:00 (Fig. 8b). In addition, higher mass concentrations  
452 and contributions of BBOA were found during the two polluted episodes (PP1 and PP2) than those  
453 during the clear periods, further indicating the important contribution of BBOA to OA in this  
454 region. Figure 8c showed the mass fractions of the three OA components as a function of total OA  
455 mass during the entire campaign. A continuously increased trend was found for the BBOA  
456 contributions with the increasing OA mass, which contributed  $\sim 15\%$  when the total OA mass was  
457 less than  $0.3 \mu\text{g m}^{-3}$ , whereas it reached up to more than 75% with the OA mass increased to  $9 \mu\text{g}$   
458  $\text{m}^{-3}$ . This dominant contribution of BBOA during the polluted periods was consistent with those  
459 results in previous studies that BB emission were an important source of aerosol to the southern  
460 TPH (Engling et al., 2011; Xia et al., 2011; Putero et al., 2014; Cong et al., 2015). The O/C ratio  
461 (0.85) of BBOA in this study was quite higher than those BBOA factors identified at other  
462 urban/rural sites in previous studies (Aiken et al., 2009; Huang et al., 2011; Mohr et al., 2012; Sun  
463 et al., 2016; Xu et al., 2016), suggesting its long-range transport feature. This aged BBOA feature  
464 was similar with those obtained at other remote sites worldwide, such as a remote forest site in  
465 Finland (Raatikainen et al., 2010), a remote background site in Greece (Bougiatioti et al., 2014),

删除的内容: S10

删除的内容: site

删除的内容: ; see details in Sect. 3.4.2

删除的内容: (Fig. 2 and S13)

470 and a national air quality background sites in southern China (Zhu et al., 2016), where OA were  
471 generally highly oxidized.

### 472 3.3.2 NOA

473 Besides the two highest signals at  $m/z$  43.99 ( $\text{CO}_2^+$ ) and 27.995 ( $\text{CO}^+$ ) which together contributed  
474 half of the total NOA signal due to the highly aged OA nature at QOMS, the NOA MS was also  
475 characterized by some nitrogen-containing fragments, such as  $m/z$  27.011 ( $\text{CHN}^+$ ), 41.027  
476 ( $\text{C}_2\text{H}_3\text{N}^+$ ), and 43.006 ( $\text{CHON}^+$ ). In total, these three fragments could comprise nearly half of the  
477 nitrogen-containing signals in the NOA factor and finally contributed 5% of the total NOA signal.  
478 The average O/C ratio of NOA for the entire campaign was 1.10 with the highest N/C ratio (0.068)  
479 among the three OA components. This high N/C ratio at QOMS was comparable with those  
480 nitrogen-containing OA factor identified in previous studies, such as 0.06 in Mexico City (Aiken  
481 et al., 2009), 0.078 in Po Valley, Italy (Saarikoski et al., 2012), and 0.053 in New York (Sun et al.,  
482 2012). The time series of NOA showed tightly correlation ( $R^2 = 0.62$ ) with that of estimated  
483 organic nitrates, whereas relatively weak correlations with  $\text{PM}_{10}$  species and OA ions (Table S2). In  
484 addition, the  $f_{60}$  value ( $\sim 0.37\%$ ) was also slightly higher than the background  $f_{60}$  (0.3%) of BB  
485 aerosols (Fig. 7h). These results together suggested that this oxygenated OA factor was likely a  
486 nitrogen-containing OA and might be related to the aged BB emissions, consistent with the results  
487 in previous studies that large amounts of nitrogen-containing organic compounds were found from  
488 BB aerosols (Laskin et al., 2009; Gautam et al., 2016; Wang et al., 2017). In recently, Fleming et  
489 al. (2017) found dung burning, a very popular activities in Himalayas and India for residential  
490 cooking and heating, could emit much more nitrogen-containing OA than wood burning. Our filter  
491 samples during high BBOA period analyzed by Fourier Transform Ion Cyclotron Resonance Mass  
492 Spectrometry (FTICR-MS) also found amount of ON molecular (in preparation). As shown in Fig.  
493 7e and 8b, both the diurnal cycles of mass concentrations and fractions of NOA had distinct  
494 increase in the morning, similar with the diurnal patterns of chloride, element ratios of H/C and  
495 N/C, and the estimated organic nitrates. This diurnal feature of NOA at QOMS was quite  
496 consistent with those NOA factors identified in Po Valley, Italy (Saarikoski et al., 2012) and in  
497 Mexico City (Aiken et al., 2009), or less-oxidized oxygenated OA (LO-OOA) in southeastern  
498 USA (Xu et al., 2015) where have active BB emissions. NOA contributed  $\sim 14\%$  of the total OA  
499 mass on average, with an average mass concentration of  $0.34 \mu\text{g m}^{-3}$  for the entire study (Fig. 8a).

### 500 3.3.3 MO-OOA

501 An obvious more oxygenated OA factor was also identified in this study according to its  
502 significant high signal at  $m/z$  44 ( $\sim 25\%$ ) and the high average O/C ratio of 1.34 (Fig. 7i). The time  
503 series of MO-OOA correlated closely ( $R^2 = 0.7$ ) with sulfate and nitrate (Fig. 7c and Table S2).  
504 Moreover, the mass spectrum of MO-OOA in this study resembled tightly to those more aged and  
505 low-volatility oxygenated OA (LV-OOA) observed using AMS instruments at various sites  
506 worldwide (Fig. S9), e.g., with  $R^2$  of 0.89 and 0.97 to those in Lanzhou, China (Xu et al., 2014;  
507 Zhang et al., 2017b), 0.96 to that in Paris, France (Crippa et al., 2013), 0.95 to that in Barcelona,  
508 Spain (Mohr et al., 2012), as well as 0.70 and 0.71 to the standard LV-OOA mass spectrums  
509 obtained from abundant AMS data sets by Ng et al. (2011a) and Crippa et al. (2014). The diurnal  
510 variation of MO-OOA was mainly driven by the dynamic of PBL height, with high concentrations  
511 during the nighttime yet relatively low concentrations during the daytime (Fig. 7f). This pattern

删除的内容: (the details could be found in Text S1, Fig. S8 and S9 in Supplement)

删除的内容: (Fig. 5)

删除的内容: (Fig. 6)

删除的内容: (Fig. S9)

删除的内容: S10

519 was quite different with those observed in previous studies that LV-OOA generally showed  
520 elevated concentrations during the afternoon in accordance with strong photochemical activities,  
521 suggesting that SOA at QOMS were mainly oxidized and aged during the long-range transport. On  
522 average, MO-OOA contributed by 42.4% of the total OA mass, with an average mass  
523 concentration of  $1.02 \mu\text{g m}^{-3}$  for the entire study (Fig. 8a). As shown in Fig. 2f and 8c, MO-OOA  
524 also displayed enhanced mass contributions during the clear periods, especially for period after  
525 May 2 when the average mass fraction of MO-OOA increased up to  $\sim 68\%$  of the total OA mass.

删除的内容: transportation

### 526 3.4 Impact of BB emissions on aerosol characteristics

#### 527 3.4.1 Sources of BB aerosols

528 In order to understand the transport pathways and the potential source areas of aerosol, 3-day back  
529 trajectories of air mass were calculated at an ending height of 500 m above ground level every 6 h  
530 at the QOMS from April 12 to May 12, 2016. A four-cluster solution and the wildfire hotspots  
531 around the QOMS during the entire measurement period were presented in Fig. 9. Cluster 1 and 2  
532 (C1 and C2), which originated from the west of the QOMS and passed over many hotspot areas  
533 (e.g., Indo-Gangetic Plain and Nepal), represented two polluted clusters. On the contrary, C3 and  
534 C4, which accounted for half of the total back trajectories, were identified as clear clusters. C3  
535 traveled a short distance from the southwest of the QOMS, whereas C4 was from the north of the  
536 QOMS and passed over the inland of the TPH. The average  $\text{PM}_{10}$  mass concentrations for C1 and  
537 C2 were  $5.17$  and  $6.61 \mu\text{g m}^{-3}$ , respectively, which were 2–3 times higher than those for the two  
538 clear clusters ( $2.74$  and  $2.21 \mu\text{g m}^{-3}$ ). The mass contributions of OA and BBOA during C1 and C2  
539 were up to more than 55% and 25% of the total  $\text{PM}_{10}$  mass on average, whereas weak contributions  
540 were found for the clear clusters (C3 and C4), indicating the significant impacts of BB emissions  
541 from South Asia on aerosol loadings at QOMS.

删除的内容: starting

#### 542 3.4.2 Comparison of aerosol characteristics and air mass origins during different episodes

543 As shown in Fig. 2, the mass concentrations and compositions of  $\text{PM}_{10}$  varied dynamically during  
544 the entire sampling period. Two polluted periods (PP1 and PP2) and two clear periods (CP1 and  
545 CP2) were identified. The comparisons of average mass concentrations and other indicators for the  
546 four different episodes were presented in box plots in Fig. 10, whereas the corresponding back  
547 trajectories of air masses and MODIS fire hotspots belong to each episode period were given in  
548 Fig. 11, respectively.

删除的内容: south

549 During the two polluted periods,  $\text{PM}_{10}$  mass concentrations were much higher than those in  
550 clear periods ( $8.06$  and  $7.87 \mu\text{g m}^{-3}$  for PP1 and PP2 vs.  $2.76$  and  $1.82 \mu\text{g m}^{-3}$  for CP1 and CP2;  
551 similarly hereinafter), with higher contributions from OA (60.1% and 57.5% vs. 48.1% and 43.9%)  
552 and BBOA (38.3% and 36.6% vs. 14.3% and 7.5%) (Fig. 10 and 11). In addition,  $f_{60}$  were also  
553 higher during polluted periods than those for clear periods (0.34% and 0.34% vs. 0.26% and 0.22%  
554 on average) (Fig. 10). Air masses during PP1 and PP2 generally originated from long-range  
555 transport to the west of the QOMS, which would pass through intense wildfires areas in South  
556 Asia (e.g., Indo-Gangetic Plain and Nepal where showed high AOD values in Fig. 1d and active  
557 fire hotspots in Fig. 9 and 11). The fire hotspot number around the air mass trajectories during PP2  
558 was more than three times higher than those during other periods. Although the hotspot number  
559 around the air mass trajectories during PP1 was not as abundant as that during PP2 and even

删除的内容: according to their high  $\text{PM}_{10}$  mass concentrations (daily average  $\text{PM}_{10}$  mass is larger than  $5 \mu\text{g m}^{-3}$ ; Fig. S12), high contributions from BBOA and unique back trajectories. The rest periods characterized by low  $\text{PM}_{10}$  mass concentrations were considered as clear periods (CP1 and CP2), as marked in Fig. 2

删除的内容: transportation

删除的内容: south

574 slightly lower than that during CP1, it was just collected within 3 days for PP1 whereas 8-10 days  
575 for another periods. Hence, the BB activities were also more frequent and intense during the short  
576 PP1 and finally resulted in the highest average  $PM_1$  mass concentration among these periods.  
577 Back trajectories in CP1 also originated from the west of QOMS and passed over the northern  
578 India and Nepal, however, both the intensity of fire hotspot number (1089 hotspots in ~ 8 days)  
579 and average FRP (19.6) were obvious lower than that in PP2. CP2 was the most clear period, of  
580 which average  $PM_1$  mass concentration was more than four times lower than those in polluted  
581 periods. Back trajectories during CP2 period were from either the north of QOMS, which passed  
582 over inland areas of the TPH or the south of QOMS with quite short distance and low WS. These  
583 results together suggested the significant roles of air mass sources and BB emissions to aerosol  
584 characteristics at QOMS.

删除的内容: site

### 585 3.4.3 Case study on the chemical evolution of BB emission aerosols

586 In order to examine how atmospheric aging affects the aerosol chemistry characteristics at QOMS,  
587 a typical evolution process of BB aerosol plume (referred as BB evolution case) was analyzed  
588 from April 30 at 15:00 when a fresh BB plume occurred to May 1 at 18:00 when the BB plume  
589 was highly aged after undergoing various atmospheric oxidation processes. The temporal  
590 variations of meteorological parameters, mass concentrations and mass contributions of each  $PM_1$   
591 species and OA components as well as other chemistry parameters before and during this BB  
592 evolution case were all shown in Fig. 12.

593 Before the BB evolution case, all the mass concentrations decreased slowly and synchronously  
594 from 00:00 to 10:00 on April 30, which were consistent with the nearly stable trends of mass  
595 contributions and other chemistry parameters, indicating the relatively unified air mass sources,  
596 and stable atmospheric conditions. After that, the wind circulations changed from the thermally-  
597 driven down-slope winds (mostly southwest) to the weak up-slope winds (northeast). In this  
598 period, BBOA and  $f_{60}$  values kept relatively stable in contrast to other species likely due to the  
599 weak of air dilution and local sources. All the species reached the minimum at around 15:00 due to  
600 the lift of PBL.

删除的内容: (Fig. S13)

601 The BB evolution case in this study was further divided into three different situations (as  
602 marked with arrows in Fig. 12 and 13), including the arriving of the fresh BBOA plume (from  
603 15:00 to 24:00 on April 30), followed by the aqueous-phase oxidation in the nighttime (from 2:30  
604 to 7:10 on May 1) and photochemical oxidation in the daytime (from 10:00 to 18:00 on May 1).  
605 All the mass concentrations began to increase from 15:00 and finally reached the maximum  $PM_1$   
606 mass loading of  $18.4 \mu g m^{-3}$  at 24:00, which was about four times higher than the average  $PM_1$   
607 mass during the entire campaign. Thus continuous increase was mainly dominated by the dramatic  
608 increase of BBOA, which reached up to  $10.8 \mu g m^{-3}$  and contributed 88% of the total OA mass  
609 and 50% of the total  $PM_1$  at 24:00 (Fig. 13a), suggesting a distinct presence of BB emissions  
610 during this period. In contrast, the total OA mass was comprised by 78% of MO-OOA and 12% of  
611 BBOA at 15:00. Similar continuous increase trend could also be found for the mass concentration  
612 of calculated organic nitrate in this stage. In addition, nine aerosol chemistry parameters were  
613 presented as a function of BBOA mass concentrations during this period (Fig. 13b). The mass  
614 contributions of OA to  $PM_1$  ( $f_{Org}$ ) and BBOA to total OA ( $f_{BBOA}$ ),  $f_{60}$ , and H/C ratio were all  
615 increased with the increasing BBOA mass, whereas the mass contribution of MO-OOA to total



618 OA ( $f_{\text{MO-OOA}}$ ), O/C ratio, carbon oxidation state ( $\text{OS}_c = 2 \times \text{O/C} - \text{H/C}$ ) of OA, and aerosol single  
619 scattering albedo (SSA) were decreased obviously, indicating the fresh nature of this BB plume.  
620 The significant impacts of fresh BB plume during this period was mainly associated with the  
621 unique wind circulation and the long-range transport of air masses. As displayed in Fig. 12b, the  
622 wind circulation changed from the weak up-slope winds to the strong down-slope glacier winds on  
623 April 30 at 15:00, with the WS increased from  $\sim 2$  to  $8 \text{ m s}^{-1}$ . Meanwhile, the back trajectories in  
624 this period also presented that the long-range transport of air masses passed over the northern  
625 India and Nepal where active wildfires occurred, then air masses would accumulate and uplift to  
626 cross the Himalayas and finally downward to QOMS with the strong glacier winds.

627 A distinct aqueous-phase oxidation process was found in the nighttime from 02:30 to 07:10 on  
628 May 1. Although the total  $\text{PM}_{10}$  and its species showed nearly stable mass concentrations during  
629 this period, the BBOA mass decreased gradually (from 82% to 70%) whereas MO-OOA increased  
630 constantly (from 14% to 20%) with the significant increase of RH (up to 91%) and aerosol liquid  
631 water content (ALWC) (Fig. 12). The scattering plots of the aerosol chemistry parameters versus  
632 the logarithmic values of cumulative ALWC, which could be used for the aqueous-phase oxidation  
633 during transport, also showed apparent increase trends for  $f_{\text{MO-OOA}}$ , O/C ratio,  $\text{OS}_c$ , and SSA that  
634 generally indicated the aerosol aging extent. All of these together suggested a distinct aqueous-  
635 phase oxidation of BBOA in the nighttime.

636 Since sunrise, all the mass concentrations decreased gradually, mainly related to the increasing  
637 PBL height and the clear air mass dilution. The back trajectories indicated that air masses during  
638 this period firstly went into the inland of the north of QOMS where had rare wildfires. Moreover,  
639 the BB plume would further undergo strong photochemical oxidation in the daytime due to the  
640 strong solar radiation. MO-OOA just contributed 26% of the total OA mass at 10:00, but it could  
641 increase to 74% at 18:00 after long-time photochemical oxidation. In contrast, BBOA mass  
642 contribution decreased from 49% to 20%. The cumulative solar radiation, which denoted the total  
643 amount of solar radiation that the plumes were exposed to during transport, could be used as an  
644 indicator for the extent of photochemical aging in the daytime (Zhou et al., 2017). Clear increased  
645 trend were found for  $f_{\text{MO-OOA}}$ , O/C ratio,  $\text{OS}_c$ , and SSA values with the increasing of cumulative  
646 solar radiation, whereas decreased trend in  $f_{\text{BBOA}}$ ,  $f_{\text{NOA}}$ , H/C ratio, and  $f_{60}$  values, suggesting a  
647 possible oxidation mechanism that the relatively fresh BBOA and NOA oxidized to aged MO-  
648 OOA in the daytime. Another interesting phenomenon was the continuous increase of SSA during  
649 both the aqueous-phase and photochemical oxidation periods on May 1 (Fig. 12e and 13b),  
650 indicating the potential influence of atmospheric aging to aerosol optical property at QOMS.

#### 651 4 Conclusions

652 A comprehensive characterization of submicron aerosol chemical compositions and sources was  
653 investigated at the QOMS during the pre-monsoon season in 2016. The average mass  
654 concentration of  $\text{PM}_{10}$  (NR- $\text{PM}_{10}$  + BC) was  $4.44 (\pm 4.54) \mu\text{g m}^{-3}$  for the entire study, which was  
655 much lower than those observed in various sites in China. OA was the dominant  $\text{PM}_{10}$  species  
656 (accounted for 54.3% of the total mass on average) and its contributions increased with the  
657 increase  $\text{PM}_{10}$  mass loading. The average size distributions of all  $\text{PM}_{10}$  species displayed an  
658 overlapping and narrow accumulation mode at  $\sim 500 \text{ nm}$ , indicating the internally well-mixed and  
659 aged aerosol particles at QOMS. All species presented similar diurnal cycles, with lower

删除的内容: transportation

删除的内容: would

删除的内容: (Fig. S13)

删除的内容: d

删除的内容: ed

删除的内容: Noting the N/C ratio also displayed constantly increased trend at night, probably associated with nitrate radical oxidation.

669 concentrations in the daytime whereas higher concentrations at the nighttime, mainly attributed to  
670 the dynamic variations of PBL height. Three OA factors were identified by PMF analysis on the  
671 high-resolution OA mass spectrum, including a relatively fresh BB-related OA (BBOA), a  
672 nitrogen-containing OA (NOA) and a more-oxidized oxygenated OA (MO-OOA). BBOA and  
673 MO-OOA could respectively account for 43.7% and 42.4% of OA mass on average, however,  
674 their contributions to OA showed completely opposite variation trends with the increase of OA  
675 mass. A continuously increased trend could be found for BBOA with the increasing OA,  
676 suggesting the key role of BBOA during polluted periods when frequent and intense wildfires  
677 were observed in South Asia. The significant impact of BB emissions on aerosol characteristics at  
678 QOMS have been also illustrated for different air mass origins and periods, respectively. Elevated  
679 PM<sub>1</sub> mass concentrations and high contributions of BBOA were found for both polluted clusters  
680 and polluted periods. A case study of typical evolution process of BB aerosol plume was  
681 investigated in detail to illustrate the chemical evolution of aerosol characteristics at QOMS. The  
682 fresh BB plume occurred in the afternoon on April 30 and finally resulted in highly PM<sub>1</sub> mass  
683 loading of 18.4 μg m<sup>-3</sup>, which was about four times higher than the average PM<sub>1</sub> mass during the  
684 entire campaign. Obvious aqueous-phase oxidation and photochemical oxidation processes were  
685 analyzed in the nighttime and daytime on May 1, respectively, both suggesting the oxidation  
686 mechanism that fresh BBOA to aged MO-OOA. The continuous increase of SSA during the two  
687 oxidation periods suggested the potential influence of atmospheric aging to aerosol optical  
688 property at QOMS.

689 *Acknowledgements.* This research was supported by grants from the National Natural Science Foundation of China  
690 (41771079, 41421061), the Key Laboratory of Cryospheric Sciences Scientific Research Foundation (SKLCS-ZZ-  
691 2017-01), and the Chinese Academy of Sciences Hundred Talents Program. The authors thank the colleagues for  
692 continuing support and discussion, and thank the NOAA Air Resources Laboratory, NASA MODIS and FIRMS  
693 teams for providing the HYSPLIT trajectory model, AOD and fire hotspots datasets.

## 694 **References**

- 695 Aiken, A. C., DeCarlo, P. F., Kroll, J. H., Worsnop, D. R., Huffman, J. A., Docherty, K. S., Ulbrich, I. M., Mohr, C., Kimmel, J.  
696 R., Sueper, D., Sun, Y., Zhang, Q., Trimborn, A., Northway, M., Ziemann, P. J., Canagaratna, M. R., Onasch, T. B., Alfarra, M.  
697 R., Prevot, A. S. H., Dommen, J., Duplissy, J., Metzger, A., Baltensperger, U., and Jimenez, J. L.: O/C and OM/OC ratios of  
698 primary, secondary, and ambient organic aerosols with high-resolution time-of-flight aerosol mass spectrometry, *Environ. Sci.*  
699 *Technol.*, 42, 4478-4485, doi:10.1021/es703009q, 2008.
- 700 Aiken, A. C., Salcedo, D., Cubison, M. J., Huffman, J. A., DeCarlo, P. F., Ulbrich, I. M., Docherty, K. S., Sueper, D., Kimmel, J.  
701 R., Worsnop, D. R., Trimborn, A., Northway, M., Stone, E. A., Schauer, J. J., Volkamer, R. M., Fortner, E., de Foy, B., Wang, J.,  
702 Laskin, A., Shutthanandan, V., Zheng, J., Zhang, R., Gaffney, J., Marley, N. A., Paredes-Miranda, G., Arnott, W. P., Molina, L.  
703 T., Sosa, G., and Jimenez, J. L.: Mexico City aerosol analysis during MILAGRO using high resolution aerosol mass  
704 spectrometry at the urban supersite (T0)–Part 1: Fine particle composition and organic source apportionment, *Atmos. Chem.*  
705 *Phys.*, 9, 6633-6653, doi:10.5194/acp-9-6633-2009, 2009.
- 706 Alfarra, M. R., Coe, H., Allan, J. D., Bower, K. N., Boudries, H., Canagaratna, M. R., Jimenez, J. L., Jayne, J. T., Garforth, A. A.,  
707 Li, S.-M., and Worsnop, D. R.: Characterization of urban and rural organic particulate in the Lower Fraser Valley using two  
708 Aerodyne Aerosol Mass Spectrometers, *Atmos. Environ.*, 38, 5745-5758, doi:10.1016/j.atmosenv.2004.01.054, 2004.
- 709 Alfarra, M. R., Prevot, A. S. H., Szidat, S., Sandradewi, J., Weimer, S., Lanz, V. A., Schreiber, D., Mohr, M., and Baltensperger,  
710 U.: Identification of the Mass Spectral Signature of Organic Aerosols from Wood Burning Emissions, *Environ. Sci. Technol.*,  
711 41, 5770-5777, doi:10.1021/es062289b, 2007.
- 712 Bonasoni, P., Laj, P., Marinoni, A., Sprenger, M., Angelini, F., Arduini, J., Bonafè U., Calzolari, F., Colombo, T., Decesari, S., Di  
713 Biagio, C., di Sarra, A. G., Evangelisti, F., Duchi, R., Facchini, M. C., Fuzzi, S., Gobbi, G. P., Maione, M., Panday, A., Roccatò,  
714 F., Sellegri, K., Venzac, H., Verza, G. P., Villani, P., Vuillermoz, E., and Cristofanelli, P.: Atmospheric Brown Clouds in the

715 Himalayas: first two years of continuous observations at the Nepal Climate Observatory-Pyramid (5079 m), *Atmos. Chem.*  
716 *Phys.*, 10, 7515-7531, doi:10.5194/acp-10-7515-2010, 2010.

717 Bond, T. C., Streets, D. G., Yarber, K. F., Nelson, S. M., Woo, J.-H., and Klimont, Z.: A technology-based global inventory of  
718 black and organic carbon emissions from combustion, *J. Geophys. Res.*, 109, doi:10.1029/2003jd003697, 2004.

719 Bougiatioti, A., Stavroulas, I., Kostenidou, E., Zarnpas, P., Theodosi, C., Kouvarakis, G., Canonaco, F., Prévôt, A. S. H., Nenes,  
720 A., Pandis, S. N., and Mihalopoulos, N.: Processing of biomass-burning aerosol in the eastern Mediterranean during  
721 summertime, *Atmos. Chem. Phys.*, 14, 4793-4807, doi:10.5194/acp-14-4793-2014, 2014.

722 Canagaratna, M. R., Jayne, J. T., Jimenez, J. L., Allan, J. D., Alfarra, M. R., Zhang, Q., Onasch, T. B., Drewnick, F., Coe, H.,  
723 Middlebrook, A., Delia, A., Williams, L. R., Trimborn, A. M., Northway, M. J., DeCarlo, P. F., Kolb, C. E., Davidovits, P., and  
724 Worsnop, D. R.: Chemical and microphysical characterization of ambient aerosols with the aerodyne aerosol mass  
725 spectrometer, *Mass Spectrom. Rev.*, 26, 185-222, doi:10.1002/mas.20115, 2007.

726 Canagaratna, M. R., Jimenez, J. L., Kroll, J. H., Chen, Q., Kessler, S. H., Massoli, P., Hildebrandt Ruiz, L., Fortner, E., Williams,  
727 L. R., Wilson, K. R., Surratt, J. D., Donahue, N. M., Jayne, J. T., and Worsnop, D. R.: Elemental ratio measurements of organic  
728 compounds using aerosol mass spectrometry: characterization, improved calibration, and implications, *Atmos. Chem. Phys.*,  
729 15, 253-272, doi:10.5194/acp-15-253-2015, 2015.

730 Cong, Z., Kang, S., Kawamura, K., Liu, B., Wan, X., Wang, Z., Gao, S., and Fu, P.: Carbonaceous aerosols on the south edge of  
731 the Tibetan Plateau: concentrations, seasonality and sources, *Atmos. Chem. Phys.*, 15, 1573-1584, doi:10.5194/acp-15-1573-  
732 2015, 2015.

733 Crippa, M., DeCarlo, P. F., Slowik, J. G., Mohr, C., Heringa, M. F., Chirico, R., Poulain, L., Freutel, F., Sciare, J., Cozic, J., Di  
734 Marco, C. F., Elsasser, M., Nicolas, J. B., Marchand, N., Abidi, E., Wiedensohler, A., Drewnick, F., Schneider, J., Borrmann, S.,  
735 Nemitz, E., Zimmermann, R., Jaffrezo, J. L., Prévôt, A. S. H., and Baltensperger, U.: Wintertime aerosol chemical composition  
736 and source apportionment of the organic fraction in the metropolitan area of Paris, *Atmos. Chem. Phys.*, 13, 961-981,  
737 doi:10.5194/acp-13-961-2013, 2013.

738 Crippa, M., Canonaco, F., Lanz, V. A., Äijälä M., Allan, J. D., Carbone, S., Capes, G., Ceburnis, D., Dall'Osto, M., Day, D. A.,  
739 DeCarlo, P. F., Ehn, M., Eriksson, A., Freney, E., Hildebrandt Ruiz, L., Hillamo, R., Jimenez, J. L., Junninen, H., Kiendler-  
740 Scharr, A., Kortelainen, A. M., Kulmala, M., Laaksonen, A., Mensah, A. A., Mohr, C., Nemitz, E., O'Dowd, C., Ovadnevaite,  
741 J., Pandis, S. N., Petäjä T., Poulain, L., Saarikoski, S., Sellegri, K., Swietlicki, E., Tiitta, P., Worsnop, D. R., Baltensperger, U.,  
742 and Prévôt, A. S. H.: Organic aerosol components derived from 25 AMS data sets across Europe using a consistent ME-2  
743 based source apportionment approach, *Atmos. Chem. Phys.*, 14, 6159-6176, doi:10.5194/acp-14-6159-2014, 2014.

744 Cubison, M. J., Ortega, A. M., Hayes, P. L., Farmer, D. K., Day, D., Lechner, M. J., Brune, W. H., Apel, E., Diskin, G. S., Fisher,  
745 J. A., Fuelberg, H. E., Hecobian, A., Knapp, D. J., Mikoviny, T., Riemer, D., Sachse, G. W., Sessions, W., Weber, R. J.,  
746 Weinheimer, A. J., Wisthaler, A., and Jimenez, J. L.: Effects of aging on organic aerosol from open biomass burning smoke in  
747 aircraft and laboratory studies, *Atmos. Chem. Phys.*, 11, 12049-12064, doi:10.5194/acp-11-12049-2011, 2011.

748 DeCarlo, P. F., Kimmel, J. R., Trimborn, A., Northway, M. J., Jayne, J. T., Aiken, A. C., Gonin, M., Fuhrer, K., Horvath, T.,  
749 Docherty, K. S., Worsnop, D. R., and Jimenez, J. L.: Field-Deployable, High-Resolution, Time-of-Flight Aerosol Mass  
750 Spectrometer, *Anal. Chem.*, 78, 8281-8289, doi:10.1021/ac061249n, 2006.

751 Decesari, S., Facchini, M. C., Carbone, C., Giulianelli, L., Rinaldi, M., Finessi, E., Fuzzi, S., Marinoni, A., Cristofanelli, P.,  
752 Duchi, R., Bonasoni, P., Vuillermoz, E., Cozic, J., Jaffrezo, J. L., and Laj, P.: Chemical composition of PM10 and PM1 at the  
753 high-altitude Himalayan station Nepal Climate Observatory-Pyramid (NCO-P) (5079 m a.s.l.), *Atmos. Chem. Phys.*, 10, 4583-  
754 4596, doi:10.5194/acp-10-4583-2010, 2010.

755 Draxler, R. R., and Rolph, G. D.: HYSPLIT (HYbrid Single-Particle Lagrangian Integrated Trajectory) model access via NOAA  
756 ARL READY website (<http://www.arl.noaa.gov/ready/hysplit4.html>). NOAA Air Resources Laboratory, Silver Spring, MD,  
757 USA, 2003.

758 Du, W., Sun, Y. L., Xu, Y. S., Jiang, Q., Wang, Q. Q., Yang, W., Wang, F., Bai, Z. P., Zhao, X. D., and Yang, Y. C.: Chemical  
759 characterization of submicron aerosol and particle growth events at a national background site (3295 m a.s.l.) on the Tibetan  
760 Plateau, *Atmos. Chem. Phys.*, 15, 10811-10824, doi:10.5194/acp-15-10811-2015, 2015.

761 Duan, A. M., and Wu, G. X.: Role of the Tibetan Plateau thermal forcing in the summer climate patterns over subtropical Asia,  
762 *Climate Dynamics*, 24, 793-807, doi:10.1007/s00382-004-0488-8, 2005.

763 Engling, G., Zhang, Y. N., Chan, C. Y., Sang, X. F., Lin, M., Ho, K. F., Li, Y. S., Lin, C. Y., and Lee, J. J.: Characterization and  
764 sources of aerosol particles over the southeastern Tibetan Plateau during the Southeast Asia biomass-burning season, *Tellus B*,  
765 63, 117-128, doi:10.1111/j.1600-0889.2010.00512.x, 2011.

766 Fleming, L. T., Lin, P., Laskin, A., Laskin, J., Weltman, R., Edwards, R. D., Arora, N. K., Yadav, A., Meinardi, S., Blake, D. R.,  
767 Pillarisetti, A., Smith, K. R., and Nizkorodov, S. A.: Molecular Composition of Particulate Matter Emissions from Dung and  
768 Brushwood Burning Household Cookstoves in Haryana, India, *Atmos. Chem. Phys. Discuss.*, 1-35, doi:10.5194/acp-2017-784,  
769 2017.

770 Fröhlich, R., Cubison, M. J., Slowik, J. G., Bukowiecki, N., Canonaco, F., Croteau, P. L., Gysel, M., Henne, S., Herrmann, E.,  
771 Jayne, J. T., Steinbacher, M., Worsnop, D. R., Baltensperger, U., and Prévôt, A. S. H.: Fourteen months of on-line  
772 measurements of the non-refractory submicron aerosol at the Jungfraujoch (3580 m a.s.l.) – chemical composition, origins and

773 organic aerosol sources, *Atmos. Chem. Phys.*, 15, 11373-11398, doi:10.5194/acp-15-11373-2015, 2015.

774 Gautam, S., Edwards, R., Yadav, A., Weltman, R., Pillarsetti, A., Arora, N. K., and Smith, K. R.: Probe-based measurements of  
775 moisture in dung fuel for emissions measurements, *Energy for Sustainable Development*, 35, 1-6,  
776 doi:10.1016/j.esd.2016.09.003, 2016.

777 Ge, X., Zhang, Q., Sun, Y., Ruehl, C. R., and Setyan, A.: Effect of aqueous-phase processing on aerosol chemistry and size  
778 distributions in Fresno, California, during wintertime, *Environ. Chem.*, 9, 221, doi:10.1071/en11168, 2012.

779 Heald, C. L., Kroll, J. H., Jimenez, J. L., Docherty, K. S., DeCarlo, P. F., Aiken, A. C., Chen, Q., Martin, S. T., Farmer, D. K., and  
780 Artaxo, P.: A simplified description of the evolution of organic aerosol composition in the atmosphere, *Geophys. Res. Lett.*, 37,  
781 L08803, doi:10.1029/2010gl042737, 2010.

782 Hou, S., Qin, D., Zhang, D., Kang, S., Mayewski, P. A., and Wake, C. P.: A 154a high-resolution ammonium record from the  
783 Rongbuk Glacier, north slope of Mt. Qomolangma (Everest), Tibet-Himal region, *Atmos. Environ.*, 37, 721-729,  
784 doi:10.1016/S1352-2310(02)00582-4, 2003.

785 Hu, W., Hu, M., Hu, W.-W., Niu, H., Zheng, J., Wu, Y., Chen, W., Chen, C., Li, L., Shao, M., Xie, S., and Zhang, Y.:  
786 Characterization of submicron aerosols influenced by biomass burning at a site in the Sichuan Basin, southwestern China,  
787 *Atmos. Chem. Phys.*, 16, 13213-13230, doi:10.5194/acp-16-13213-2016, 2016.

788 Huang, X. F., He, L. Y., Hu, M., Canagaratna, M. R., Kroll, J. H., Ng, N. L., Zhang, Y. H., Lin, Y., Xue, L., Sun, T. L., Liu, X. G.,  
789 Shao, M., Jayne, J. T., and Worsnop, D. R.: Characterization of submicron aerosols at a rural site in Pearl River Delta of China  
790 using an Aerodyne High-Resolution Aerosol Mass Spectrometer, *Atmos. Chem. Phys.*, 11, 1865-1877, doi:10.5194/acp-11-  
791 1865-2011, 2011.

792 Huang, X. F., He, L. Y., Xue, L., Sun, T. L., Zeng, L. W., Gong, Z. H., Hu, M., and Zhu, T.: Highly time-resolved chemical  
793 characterization of atmospheric fine particles during 2010 Shanghai World Expo, *Atmos. Chem. Phys.*, 12, 4897-4907,  
794 doi:10.5194/acp-12-4897-2012, 2012.

795 Jayne, J. T., Leard, D. C., Zhang, X. F., Davidovits, P., Smith, K. A., Kolb, C. E., and Worsnop, D. R.: Development of an aerosol  
796 mass spectrometer for size and composition analysis of submicron particles, *Aerosol Sci. Technol.*, 33, 49-70,  
797 doi:10.1080/027868200410840, 2000.

798 Jimenez, J. L., Jayne, J. T., Shi, Q., Kolb, C. E., Worsnop, D. R., Yourshaw, I., Seinfeld, J. H., Flagan, R. C., Zhang, X., Smith, K.  
799 A., Morris, J. W., and Davidovits, P.: Ambient aerosol sampling using the Aerodyne Aerosol Mass Spectrometer, *J. Geophys.*  
800 *Res.*, 108, doi:10.1029/2001jd001213, 2003.

801 Jimenez, J. L., Canagaratna, M. R., Donahue, N. M., Prevot, A. S., Zhang, Q., Kroll, J. H., DeCarlo, P. F., Allan, J. D., Coe, H.,  
802 Ng, N. L., Aiken, A. C., Docherty, K. S., Ulbrich, I. M., Grieshop, A. P., Robinson, A. L., Duplissy, J., Smith, J. D., Wilson, K.  
803 R., Lanz, V. A., Hueglin, C., Sun, Y. L., Tian, J., Laaksonen, A., Raatikainen, T., Rautiainen, J., Vaattovaara, P., Ehn, M.,  
804 Kulmala, M., Tomlinson, J. M., Collins, D. R., Cubison, M. J., Dunlea, E. J., Huffman, J. A., Onasch, T. B., Alfarra, M. R.,  
805 Williams, P. I., Bower, K., Kondo, Y., Schneider, J., Drewnick, F., Borrmann, S., Weimer, S., Demerjian, K., Salcedo, D.,  
806 Cottrell, L., Griffin, R., Takami, A., Miyoshi, T., Hatakeyama, S., Shimono, A., Sun, J. Y., Zhang, Y. M., Dzepina, K., Kimmel,  
807 J. R., Sueper, D., Jayne, J. T., Herndon, S. C., Trimborn, A. M., Williams, L. R., Wood, E. C., Middlebrook, A. M., Kolb, C. E.,  
808 Baltensperger, U., and Worsnop, D. R.: Evolution of organic aerosols in the atmosphere, *Science*, 326, 1525-1529,  
809 doi:10.1126/science.1180353, 2009.

810 Kang, S., Xu, Y., You, Q., Flügel, W.-A., Pepin, N., and Yao, T.: Review of climate and cryospheric change in the Tibetan Plateau,  
811 *Environ. Res. Lett.*, 5, 015101, doi:10.1088/1748-9326/5/1/015101, 2010.

812 Laskin, A., Smith, J. S., and Laskin, J.: Molecular Characterization of Nitrogen-Containing Organic Compounds in Biomass  
813 Burning Aerosols Using High-Resolution Mass Spectrometry, *Environ. Sci. Technol.*, 43, 3764-3771, doi:10.1021/es803456n,  
814 2009.

815 Lau, K. M., Kim, M. K., and Kim, K. M.: Asian summer monsoon anomalies induced by aerosol direct forcing: the role of the  
816 Tibetan Plateau, *Climate Dynamics*, 26, 855-864, doi:10.1007/s00382-006-0114-z, 2006.

817 Lau, K. M., Tsay, S. C., Hsu, C., Chin, M., Ramanathan, V., Wu, G. X., Li, Z., Sikka, R., Holben, B., Lu, D., Chen, H., Tartari, G.,  
818 Koudeleva, P., Ma, Y., Huang, J., Taniguchi, K., and Zhang, R.: The Joint Aerosol-Monsoon Experiment: A New Challenge  
819 for Monsoon Climate Research, *Bulletin of the American Meteorological Society*, 89, 369-383, doi:10.1175/bams-89-3-369,  
820 2008.

821 Li, C., Bosch, C., Kang, S., Andersson, A., Chen, P., Zhang, Q., Cong, Z., Chen, B., Qin, D., and Gustafsson, O.: Sources of  
822 black carbon to the Himalayan-Tibetan Plateau glaciers, *Nat. Commun.*, 7, 12574, doi:10.1038/ncomms12574, 2016.

823 [Li, Y. J., Sun, Y., Zhang, Q., Li, X., Li, M., Zhou, Z., and Chan, C. K.: Real-time chemical characterization of atmospheric  
824 particulate matter in China: A review, \*Atmos. Environ.\*, 158, 270-304, doi:10.1016/j.atmosenv.2017.02.027, 2017.](#)

825 Liu, B., Cong, Z., Wang, Y., Xin, J., Wan, X., Pan, Y., Liu, Z., Wang, Y., Zhang, G., Wang, Z., Wang, Y., and Kang, S.:  
826 Background aerosol over the Himalayas and Tibetan Plateau: observed characteristics of aerosol mass loading, *Atmos. Chem.*  
827 *Phys.*, 17, 449-463, doi:10.5194/acp-17-449-2017, 2017.

828 Liu, Z., Liu, D., Huang, J., Vaughan, M., Uno, I., Sugimoto, N., Kittaka, C., Trepte, C., Wang, Z., Hostetler, C., and Winker, D.:  
829 Airborne dust distributions over the Tibetan Plateau and surrounding areas derived from the first year of CALIPSO lidar  
830 observations, *Atmos. Chem. Phys.*, 8, 5045-5060, doi:10.5194/acp-8-5045-2008, 2008.

831 Ma, Y., Kang, S., Zhu, L., Xu, B., Tian, L., and Yao, T.: ROOF OF THE WORLD: Tibetan Observation and Research Platform,  
832 Bulletin of the American Meteorological Society, 89, 1487-1492, doi:10.1175/2008bams2545.1, 2008.

833 Marcq, S., Laj, P., Roger, J. C., Villani, P., Sellegri, K., Bonasoni, P., Marinoni, A., Cristofanelli, P., Verza, G. P., and Bergin, M.:  
834 Aerosol optical properties and radiative forcing in the high Himalaya based on measurements at the Nepal Climate  
835 Observatory-Pyramid site (5079 m a.s.l.), Atmos. Chem. Phys., 10, 5859-5872, doi:10.5194/acp-10-5859-2010, 2010.

836 Marinoni, A., Cristofanelli, P., Laj, P., Duchi, R., Putero, D., Calzolari, F., Landi, T. C., Vuillermoz, E., Maione, M., and  
837 Bonasoni, P.: High black carbon and ozone concentrations during pollution transport in the Himalayas: Five years of  
838 continuous observations at NCO-P global GAW station, J. Environ. Sci., 25, 1618-1625, doi:10.1016/S1001-0742(12)60242-3,  
839 2013.

840 Mohr, C., DeCarlo, P. F., Heringa, M. F., Chirico, R., Slowik, J. G., Richter, R., Reche, C., Alastuey, A., Querol, X., Seco, R.,  
841 Peñuelas, J., Jiménez, J. L., Crippa, M., Zimmermann, R., Baltensperger, U., and Prévôt, A. S. H.: Identification and  
842 quantification of organic aerosol from cooking and other sources in Barcelona using aerosol mass spectrometer data, Atmos.  
843 Chem. Phys., 12, 1649-1665, doi:10.5194/acp-12-1649-2012, 2012.

844 Ng, N., Canagaratna, M., Jimenez, J., Zhang, Q., Ulbrich, I., and Worsnop, D.: Real-time methods for estimating organic  
845 component mass concentrations from aerosol mass spectrometer data, Environ. Sci. Technol., 45, 910-916,  
846 doi:10.1021/es102951k, 2011a.

847 Ng, N. L., Canagaratna, M. R., Jimenez, J. L., Chhabra, P. S., Seinfeld, J. H., and Worsnop, D. R.: Changes in organic aerosol  
848 composition with aging inferred from aerosol mass spectra, Atmos. Chem. Phys., 11, 6465-6474, doi:10.5194/acp-11-6465-  
849 2011, 2011b.

850 Paatero, P., and Tapper, U.: Positive matrix factorization: A non-negative factor model with optimal utilization of error estimates  
851 of data values, Environmetrics, 5, 111-126, doi:10.1002/env.3170050203, 1994.

852 Putero, D., Landi, T. C., Cristofanelli, P., Marinoni, A., Laj, P., Duchi, R., Calzolari, F., Verza, G. P., and Bonasoni, P.: Influence  
853 of open vegetation fires on black carbon and ozone variability in the southern Himalayas (NCO-P, 5079 m a.s.l.), Environ.  
854 Pollut., 184, 597-604, doi:10.1016/j.envpol.2013.09.035, 2014.

855 Raatikainen, T., Vaattovaara, P., Tiitta, P., Miettinen, P., Rautiainen, J., Ehn, M., Kulmala, M., Laaksonen, A., and Worsnop, D. R.:  
856 Physicochemical properties and origin of organic groups detected in boreal forest using an aerosol mass spectrometer, Atmos.  
857 Chem. Phys., 10, 2063-2077, doi:10.5194/acp-10-2063-2010, 2010.

858 Ram, K., Sarin, M. M., and Hegde, P.: Long-term record of aerosol optical properties and chemical composition from a high-  
859 altitude site (Manora Peak) in Central Himalaya, Atmos. Chem. Phys., 10, 11791-11803, doi:10.5194/acp-10-11791-2010,  
860 2010.

861 Ramanathan, V., and Carmichael, G.: Global and regional climate changes due to black carbon, Nature Geoscience, 1, 221-227,  
862 doi:10.1038/ngeo156, 2008.

863 Saarikoski, S., Carbone, S., Decesari, S., Giulianelli, L., Angelini, F., Canagaratna, M., Ng, N. L., Trimborn, A., Facchini, M. C.,  
864 Fuzzi, S., Hillamo, R., and Worsnop, D.: Chemical characterization of springtime submicrometer aerosol in Po Valley, Italy,  
865 Atmos. Chem. Phys., 12, 8401-8421, doi:10.5194/acp-12-8401-2012, 2012.

866 Sun, Y., Zhang, Q., Macdonald, A., Hayden, K., Li, S., Liggio, J., Liu, P., Anlauf, K., Leaitch, W., and Steffen, A.: Size-resolved  
867 aerosol chemistry on Whistler Mountain, Canada with a high-resolution aerosol mass spectrometer during INTEX-B, Atmos.  
868 Chem. Phys., 9, 3095-3111, doi:10.5194/acp-9-3095-2009, 2009.

869 Sun, Y. L., Zhang, Q., Schwab, J. J., Chen, W. N., Bae, M. S., Hung, H. M., Lin, Y. C., Ng, N. L., Jayne, J., Massoli, P., Williams,  
870 L. R., and Demerjian, K. L.: Characterization of near-highway submicron aerosols in New York City with a high-resolution  
871 aerosol mass spectrometer, Atmos. Chem. Phys., 12, 2215-2227, doi:10.5194/acp-12-2215-2012, 2012.

872 Sun, Y., Wang, Z., Fu, P., Jiang, Q., Yang, T., Li, J., and Ge, X.: The impact of relative humidity on aerosol composition and  
873 evolution processes during wintertime in Beijing, China, Atmos. Environ., 77, 927-934, doi:10.1016/j.atmosenv.2013.06.019,  
874 2013.

875 Sun, Y., Du, W., Fu, P., Wang, Q., Li, J., Ge, X., Zhang, Q., Zhu, C., Ren, L., Xu, W., Zhao, J., Han, T., Worsnop, D. R., and  
876 Wang, Z.: Primary and secondary aerosols in Beijing in winter: sources, variations and processes, Atmos. Chem. Phys., 16,  
877 8309-8329, doi:10.5194/acp-16-8309-2016, 2016.

878 Takami, A., Miyoshi, T., Shimono, A., and Hatakeyama, S.: Chemical composition of fine aerosol measured by AMS at Fukue  
879 Island, Japan during APEX period, Atmos. Environ., 39, 4913-4924, doi:10.1016/j.atmosenv.2005.04.038, 2005.

880 Ulbrich, I. M., Canagaratna, M. R., Zhang, Q., Worsnop, D. R., and Jimenez, J. L.: Interpretation of organic components from  
881 Positive Matrix Factorization of aerosol mass spectrometric data, Atmos. Chem. Phys., 9, 2891-2918, doi:10.5194/acp-9-2891-  
882 2009, 2009.

883 Wan, X., Kang, S., Li, Q., Rupakheti, D., Zhang, Q., Guo, J., Chen, P., Tripathee, L., Rupakheti, M., Panday, A. K., Wang, W.,  
884 Kawamura, K., Gao, S., Wu, G., and Cong, Z.: Organic molecular tracers in the atmospheric aerosols from Lumbini, Nepal, in  
885 the northern Indo-Gangetic Plain: influence of biomass burning, Atmos. Chem. Phys., 17, 8867-8885, doi:10.5194/acp-17-  
886 8867-2017, 2017.

887 Wang, J., Ge, X., Chen, Y., Shen, Y., Zhang, Q., Sun, Y., Xu, J., Ge, S., Yu, H., and Chen, M.: Highly time-resolved urban aerosol  
888 characteristics during springtime in Yangtze River Delta, China: insights from soot particle aerosol mass spectrometry, Atmos.

889 Chem. Phys., 16, 9109-9127, doi:10.5194/acp-16-9109-2016, 2016a.

890 [Wang, J., Onasch, T. B., Ge, X., Collier, S., Zhang, Q., Sun, Y., Yu, H., Chen, M., Prévôt, A. S. H., and Worsnop, D. R.:](#)  
891 [Observation of Fullerene Soot in Eastern China, Environ. Sci. Technol. Lett., 3, 121-126, doi:10.1021/acs.estlett.6b00044,](#)  
892 [2016b.](#)

893 [Wang, J., Zhang, Q., Chen, M., Collier, S., Zhou, S., Ge, X., Xu, J., Shi, J., Xie, C., Hu, J., Ge, S., Sun, Y., and Coe, H.: First](#)  
894 [Chemical Characterization of Refractory Black Carbon Aerosols and Associated Coatings over the Tibetan Plateau \(4730 m](#)  
895 [a.s.l.\), Environ. Sci. Technol., 51, 14072-14082, doi:10.1021/acs.est.7b03973, 2017.](#)

896 Wang, Y., Hu, M., Lin, P., Guo, Q., Wu, Z., Li, M., Zeng, L., Song, Y., Zeng, L., Wu, Y., Guo, S., Huang, X., and He, L.:  
897 Molecular Characterization of Nitrogen-Containing Organic Compounds in Humic-like Substances Emitted from Straw  
898 Residue Burning, Environ. Sci. Technol., 51, 5951-5961, doi:10.1021/acs.est.7b00248, 2017.

899 Wu, G., Liu, Y., Zhang, Q., Duan, A., Wang, T., Wan, R., Liu, X., Li, W., Wang, Z., and Liang, X.: The Influence of Mechanical  
900 and Thermal Forcing by the Tibetan Plateau on Asian Climate, Journal of Hydrometeorology, 8, 770-789,  
901 doi:10.1175/jhm609.1, 2007.

902 Xia, X., Zong, X., Cong, Z., Chen, H., Kang, S., and Wang, P.: Baseline continental aerosol over the central Tibetan plateau and a  
903 case study of aerosol transport from South Asia, Atmos. Environ., 45, 7370-7378, doi:10.1016/j.atmosenv.2011.07.067, 2011.

904 Xu, B., Cao, J., Hansen, J., Yao, T., Joswila, D. R., Wang, N., Wu, G., Wang, M., Zhao, H., Yang, W., Liu, X., and He, J.: Black  
905 soot and the survival of Tibetan glaciers, Proc. Natl. Acad. Sci. USA, 106, 22114-22118, doi:10.1073/pnas.0910444106, 2009.

906 Xu, J., Zhang, Q., Chen, M., Ge, X., Ren, J., and Qin, D.: Chemical composition, sources, and processes of urban aerosols during  
907 summertime in northwest China: insights from high-resolution aerosol mass spectrometry, Atmos. Chem. Phys., 14, 12593-  
908 12611, doi:10.5194/acp-14-12593-2014, 2014.

909 Xu, J., Shi, J., Zhang, Q., Ge, X., Canonaco, F., Prévôt, A. S. H., Vonwiller, M., Szidat, S., Ge, J., Ma, J., An, Y., Kang, S., and  
910 Qin, D.: Wintertime organic and inorganic aerosols in Lanzhou, China: sources, processes, and comparison with the results  
911 during summer, Atmos. Chem. Phys., 16, 14937-14957, doi:10.5194/acp-16-14937-2016, 2016.

912 Xu, J., Zhang, Q., Shi, J., Ge, X., Xie, C., Wang, J., Kang, S., Zhang, R., and Wang, Y.: Chemical characteristics of submicron  
913 particles at the central Tibet Plateau: influence of long-range transport, Atmos. Chem. Phys. Discuss., 1-32, doi:10.5194/acp-  
914 2017-587, 2017.

915 Xu, L., Suresh, S., Guo, H., Weber, R. J., and Ng, N. L.: Aerosol characterization over the southeastern United States using high-  
916 resolution aerosol mass spectrometry: spatial and seasonal variation of aerosol composition and sources with a focus on  
917 organic nitrates, Atmos. Chem. Phys., 15, 7307-7336, doi:10.5194/acp-15-7307-2015, 2015.

918 Yadav, I. C., Devi, N. L., Li, J., Syed, J. H., Zhang, G., and Watanabe, H.: Biomass burning in Indo-China peninsula and its  
919 impacts on regional air quality and global climate change-a review, Environmental pollution, 227, 414-427,  
920 doi:10.1016/j.envpol.2017.04.085, 2017.

921 Yang, K., Wu, H., Qin, J., Lin, C., Tang, W., and Chen, Y.: Recent climate changes over the Tibetan Plateau and their impacts on  
922 energy and water cycle: A review, Global and Planetary Change, 112, 79-91, doi:10.1016/j.gloplacha.2013.12.001, 2014.

923 Yao, T., Thompson, L., Mosbrugger, V., Zhang, F., Ma, Y., Luo, T., Xu, B., Yang, X., Joswiak, D. R., Wang, W., Joswiak, M. E.,  
924 Devkota, L. P., Tayal, S., Jilani, R., and Fayziev, R.: Third Pole Environment (TPE), Environmental Development, 3, 52-64,  
925 doi:10.1016/j.envdev.2012.04.002, 2012a.

926 Yao, T., Thompson, L., Yang, W., Yu, W., Gao, Y., Guo, X., Yang, X., Duan, K., Zhao, H., Xu, B., Pu, J., Lu, A., Xiang, Y., Kattel,  
927 D. B., and Joswiak, D.: Different glacier status with atmospheric circulations in Tibetan Plateau and surroundings, Nature Clim.  
928 Change, 2, 663-667, doi:10.1038/nclimate1580, 2012b.

929 Zhang, Q., Alfarra, M. R., Worsnop, D. R., Allan, J. D., Coe, H., Canagaratna, M. R., and Jimenez, J. L.: Deconvolution and  
930 quantification of hydrocarbon-like and oxygenated organic aerosols based on aerosol mass spectrometry, Environ. Sci.  
931 Technol., 39, 4938-4952, doi:10.1021/es048568l, 2005a.

932 Zhang, Q., Canagaratna, M. R., Jayne, J. T., Worsnop, D. R., and Jimenez, J. L.: Time- and size-resolved chemical composition  
933 of submicron particles in Pittsburgh: Implications for aerosol sources and processes, J. Geophys. Res., 110,  
934 doi:10.1029/2004jd004649, 2005b.

935 Zhang, Q., Jimenez, J. L., Canagaratna, M. R., Allan, J. D., Coe, H., Ulbrich, I., Alfarra, M. R., Takami, A., Middlebrook, A. M.,  
936 Sun, Y. L., Dzepina, K., Dunlea, E., Docherty, K., DeCarlo, P. F., Salcedo, D., Onasch, T., Jayne, J. T., Miyoshi, T., Shimo,  
937 A., Hatakeyama, S., Takegawa, N., Kondo, Y., Schneider, J., Drewnick, F., Borrmann, S., Weimer, S., Demerjian, K., Williams,  
938 P., Bower, K., Bahreini, R., Cottrell, L., Griffin, R. J., Rautiainen, J., Sun, J. Y., Zhang, Y. M., and Worsnop, D. R.: Ubiquity  
939 and dominance of oxygenated species in organic aerosols in anthropogenically-influenced Northern Hemisphere midlatitudes,  
940 Geophys. Res. Lett., 34, doi:10.1029/2007gl029979, 2007a.

941 Zhang, Q., Jimenez, J. L., Worsnop, D. R., and Canagaratna, M.: A case study of urban particle acidity and its influence on  
942 secondary organic aerosol, Environ. Sci. Technol., 41, 3213-3219, doi:10.1021/es061812j, 2007b.

943 Zhang, Q., Jimenez, J. L., Canagaratna, M. R., Ulbrich, I. M., Ng, N. L., Worsnop, D. R., and Sun, Y.: Understanding  
944 atmospheric organic aerosols via factor analysis of aerosol mass spectrometry: a review, Anal. Bioanal. Chem., 401, 3045-  
945 3067, doi:10.1007/s00216-011-5355-y, 2011.

946 Zhang, R., Wang, Y., He, Q., Chen, L., Zhang, Y., Qu, H., Smeltzer, C., Li, J., Alvarado, L. M. A., Vrekoussis, M., Richter, A.,

947 Wittrock, F., and Burrows, J. P.: Enhanced trans-Himalaya pollution transport to the Tibetan Plateau by cut-off low systems,  
948 *Atmos. Chem. Phys.*, 17, 3083-3095, doi:10.5194/acp-17-3083-2017, 2017a.

949 Zhang, X., Zhang, Y., Sun, J., Yu, Y., Canonaco, F., Prevot, A. S., and Li, G.: Chemical characterization of submicron aerosol  
950 particles during wintertime in a northwest city of China using an Aerodyne aerosol mass spectrometry, *Environ. Pollut.*, 222,  
951 567-582, doi:10.1016/j.envpol.2016.11.012, 2017b.

952 Zhao, Z., Cao, J., Shen, Z., Xu, B., Zhu, C., Chen, L. W. A., Su, X., Liu, S., Han, Y., Wang, G., and Ho, K.: Aerosol particles at a  
953 high-altitude site on the Southeast Tibetan Plateau, China: Implications for pollution transport from South Asia, *J. Geophys.*  
954 *Res.-Atmos.*, 118, 11360-11375, doi:10.1002/jgrd.50599, 2013.

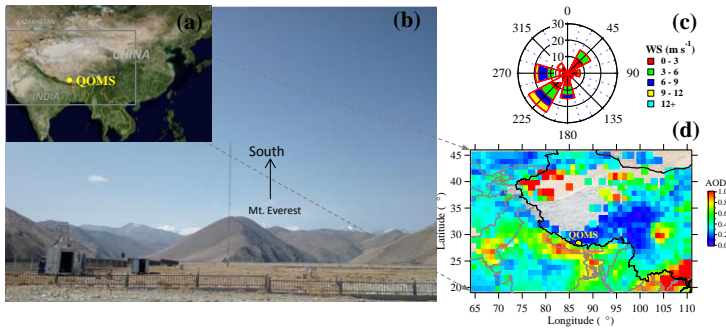
955 Zheng, J., Hu, M., Du, Z., Shang, D., Gong, Z., Qin, Y., Fang, J., Gu, F., Li, M., Peng, J., Li, J., Zhang, Y., Huang, X., He, L., Wu,  
956 Y., and Guo, S.: Influence of biomass burning from South Asia at a high-altitude mountain receptor site in China, *Atmos.*  
957 *Chem. Phys.*, 17, 6853-6864, doi:10.5194/acp-17-6853-2017, 2017.

958 Zhou, S., Collier, S., Jaffe, D. A., Briggs, N. L., Hee, J., Sedlacek Iii, A. J., Kleinman, L., Onasch, T. B., and Zhang, Q.: Regional  
959 influence of wildfires on aerosol chemistry in the western US and insights into atmospheric aging of biomass burning organic  
960 aerosol, *Atmos. Chem. Phys.*, 17, 2477-2493, doi:10.5194/acp-17-2477-2017, 2017.

961 Zhu, Q., He, L. Y., Huang, X. F., Cao, L. M., Gong, Z. H., Wang, C., Zhuang, X., and Hu, M.: Atmospheric aerosol compositions  
962 and sources at two national background sites in northern and southern China, *Atmos. Chem. Phys.*, 16, 10283-10297,  
963 doi:10.5194/acp-16-10283-2016, 2016.

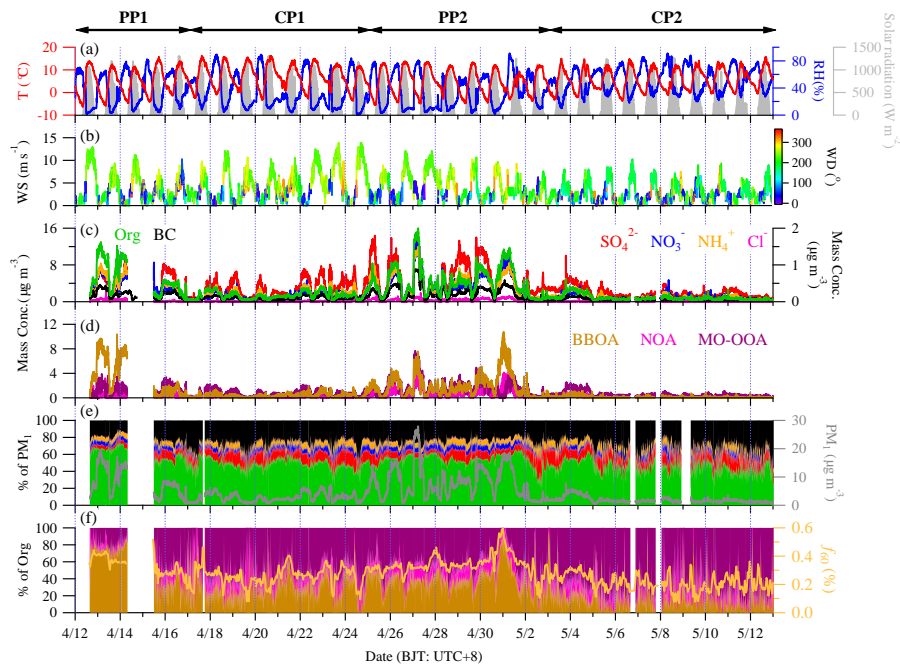
964 Zou, H., Zhou, L., Ma, S., Li, P., Wang, W., Li, A., Jia, J., and Gao, D.: Local wind system in the Rongbuk Valley on the northern  
965 slope of Mt. Everest, *Geophys. Res. Lett.*, 35, doi:10.1029/2008gl033466, 2008.

966



967  
968  
969  
970

**Figure 1.** (a) Location map for the QOMS, (b) picture for the QOMS and its surrounding, (c) wind rose plot colored by wind speed in this study, and (d) distribution of the average aerosol optical depth (AOD) around the QOMS retrieved from Terra MODIS at 550 nm during this study.

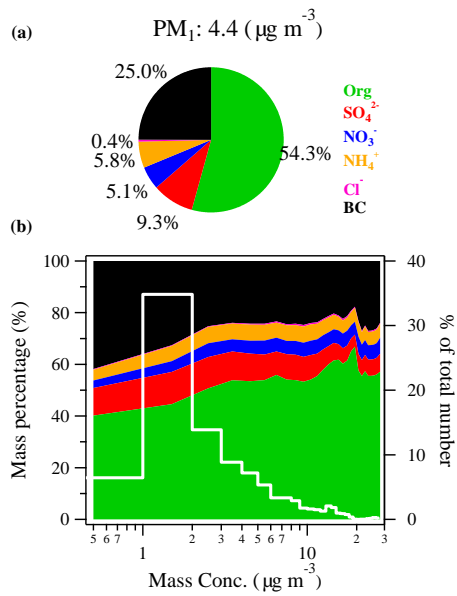


971  
972  
973  
974  
975  
976  
977

**Figure 2.** Summary of meteorological and HR-ToF-AMS data. The 5-min time series of (a) ambient temperature ( $T$ ), relative humidity (RH), and solar radiation, (b) wind speed (WS) colored by wind direction (WD), (c) mass concentrations of  $PM_1$  species, (d) mass concentrations of organic components, (e) mass contributions of  $PM_1$  species to total  $PM_1$  as well as total  $PM_1$  mass concentrations, and (f) mass contributions of organic components to organics. The time series of hourly average  $f_{60}$  ( $= C_2H_4O_2^+ / OA$ ) values for the entire period is also showed. The markers of PP1 and PP2 represent the two polluted periods while CP1 and CP2 are clear periods, respectively.

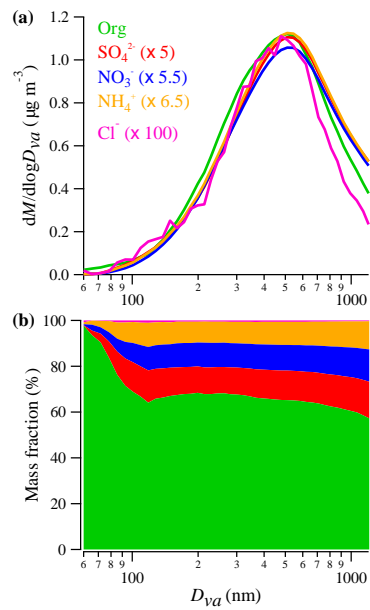
删除的内容: and





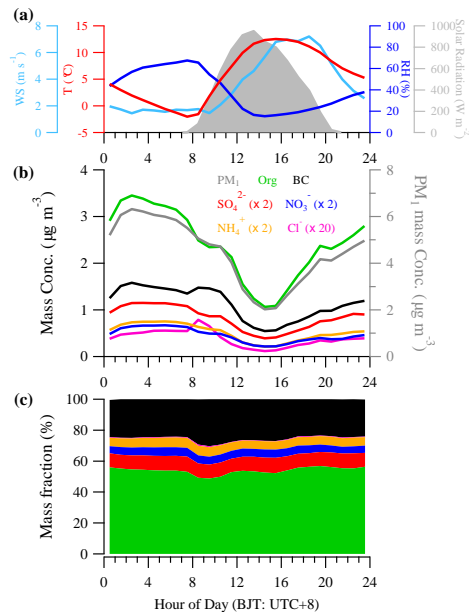
979  
980  
981  
982

**Figure 3.** The average mass contributions of PM<sub>1</sub> (= NR-PM<sub>1</sub>+ BC) species (a) during the entire sampling period and (b) as a function of the total PM<sub>1</sub> mass concentrations. The white solid line in (b) shows the percentage of the data number in each mass bins to the total data number.

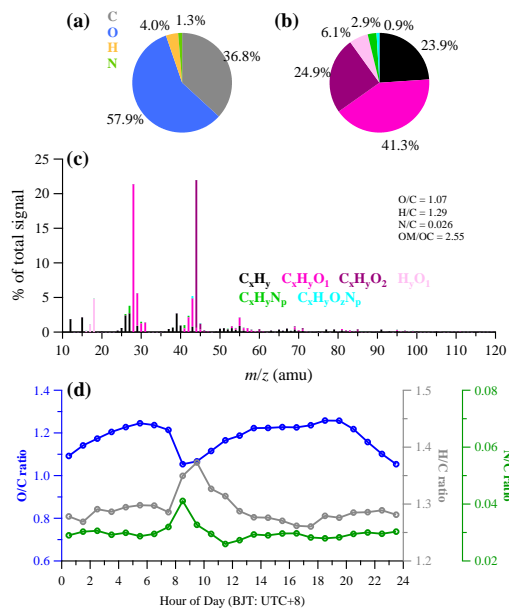


983  
984  
985

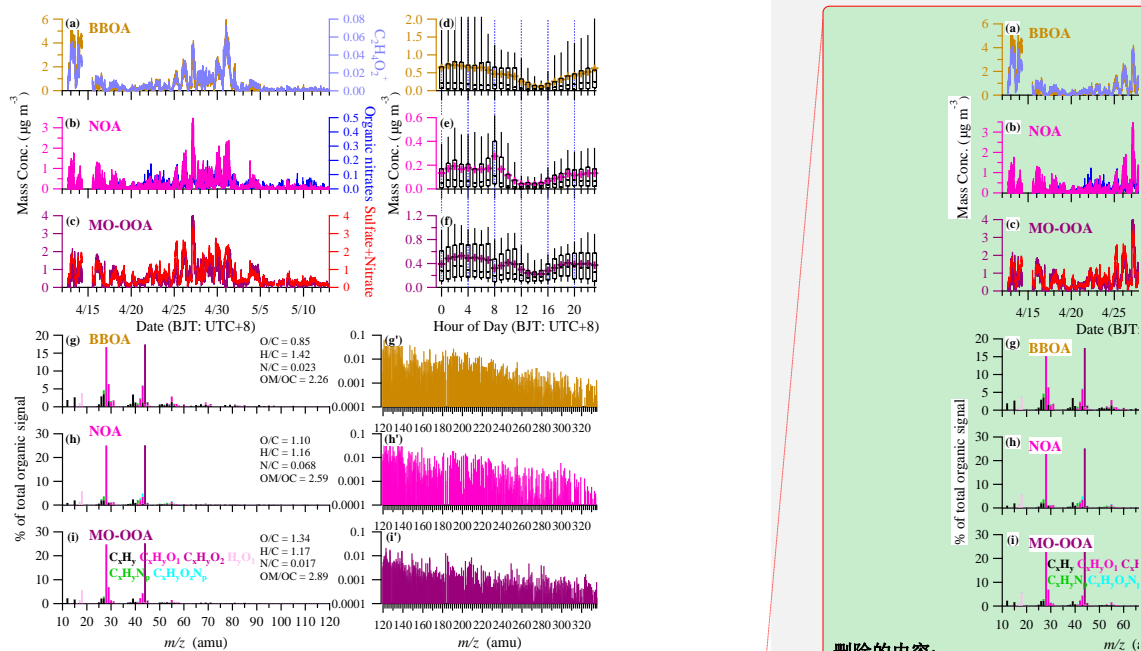
**Figure 4.** The average size distributions of (a) mass concentrations and (b) mass contributions of NR-PM<sub>1</sub> species for the entire study.



986 **Figure 5.** The diurnal cycles of (a) meteorological parameters (temperature, RH, wind speed, and solar radiation), (b) mass  
 987 concentrations and (c) mass contributions of PM<sub>1</sub> chemical species for the entire study.  
 988



989 **Figure 6.** The average contributions of (a) four elements (C, O, H, and N) and (b) six ion categories (colors as in (c)) to OA for  
 990 the entire study; (c) the average high-resolution mass spectrum of OA (colors show six ion categories); (d) the diurnal variations  
 991 of O/C, H/C, and N/C ratios.  
 992

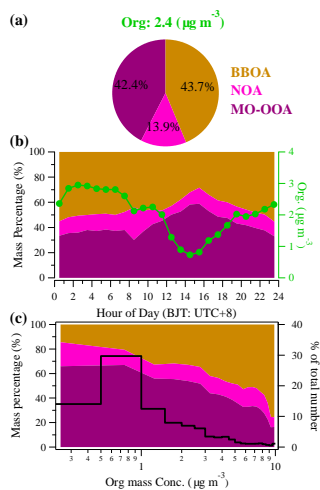


993  
994  
995  
996  
997  
998

**Figure 7.** The PMF results of (a–c) the time series of three OA factors and corresponding tracer species, (d–f) the diurnal variations of the mass concentrations of the three OA factors (the whiskers above and below the boxes indicate the 90th and 10th percentiles, the upper and lower boundaries respectively indicate the 75th and 25th percentiles, the lines in the boxes indicate the median values, and the cross symbols indicate the mean values), (g–i) high-resolution mass spectra of the three OA factors colored by six ion families at  $m/z < 120$ , and (g'–i') the unit resolution mass spectra at  $m/z > 120$  for each OA factor.

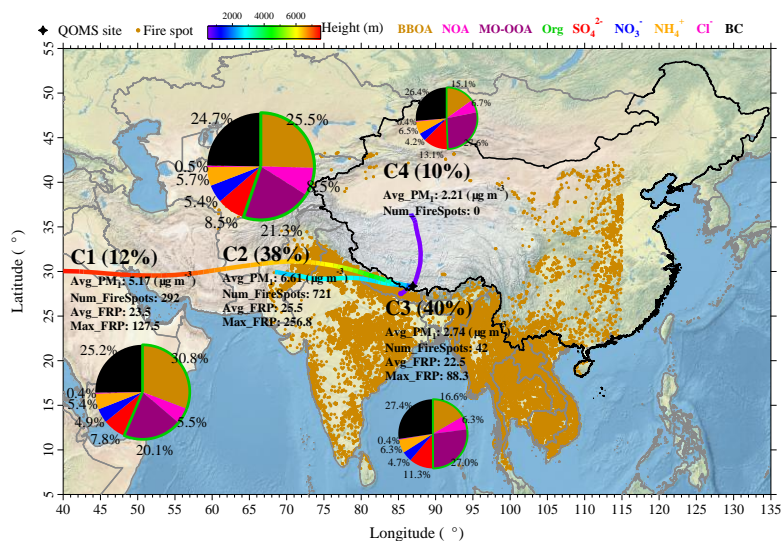
删除的内容:

带格式的: 字体: (默认) Times  
New Roman, 小五



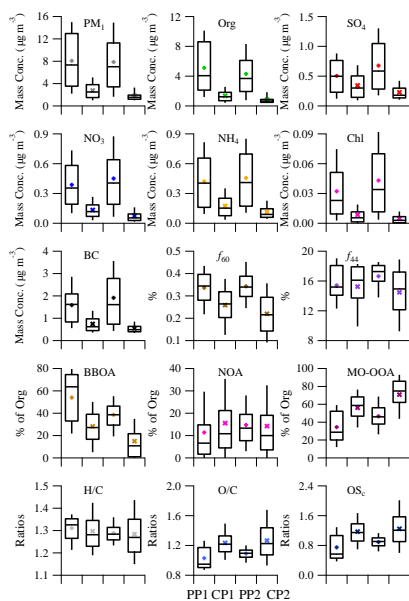
999  
1000  
1001  
1002  
1003

**Figure 8.** (a) The average mass concentration of OA and mass contributions of three OA factors to total OA; (b) the diurnal variations of mass contributions of three OA factors to total OA and the total OA mass concentration; (c) The average mass contributions of three OA factors as a function of total OA mass concentration. The black solid line in (c) shows the percentage of the data number in each OA mass bins to the total data number.



1005  
1006  
1007  
1008  
1009

**Figure 9.** The average back trajectory clusters during the entire study and the corresponding mass contributions of PM<sub>1</sub> species and OA factors to the total PM<sub>1</sub> mass. The areas of each pie charts are scaled by the corresponding average PM<sub>1</sub> mass concentrations. The average PM<sub>1</sub> mass concentrations, number of fire hotspots as well as the average and maximum fire radiative powers (FRP) belong to each clusters during the entire measurement period are also given.



1010  
1011  
1012  
1013  
1014

**Figure 10.** Box plots of mass concentrations of total PM<sub>1</sub> and its species,  $f_{60}$  and  $f_{44}$  values, mass contribution of three OA components to organics, element ratios (H/C and O/C), and carbon oxidation states ( $OS_c$ ) among the four polluted and clear periods. The whiskers indicate the 90th and 10th percentiles, the upper and lower boundaries of boxes indicate the 75th and 25th percentiles, the lines in the boxes indicate the median values, and the markers indicate the mean values.

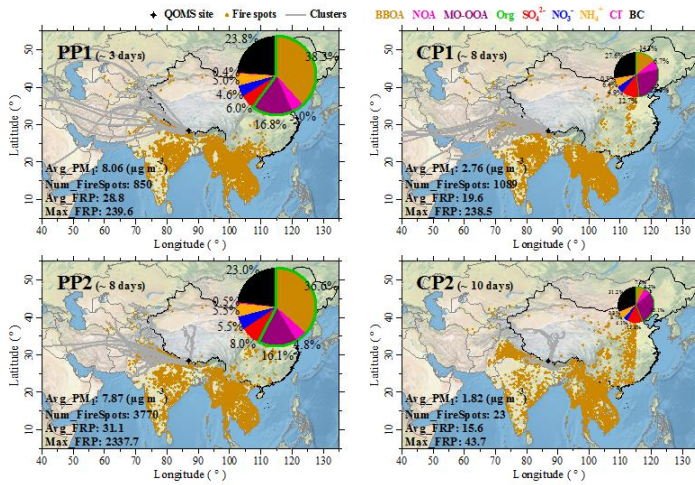


**Figure 11.** The 72-h back trajectories (grey solid lines) calculated every 6 h for the different episodes. Pie charts show the average mass contributions of PM<sub>1</sub> species and OA factors to the total PM<sub>1</sub> mass for each episodes (scaled by the corresponding average PM<sub>1</sub> mass concentrations). The average PM<sub>1</sub> mass concentrations, number of fire hotspots as well as the average and maximum fire radiative powers (FRP) belong to all trajectories for the different CPI episodes are also given.

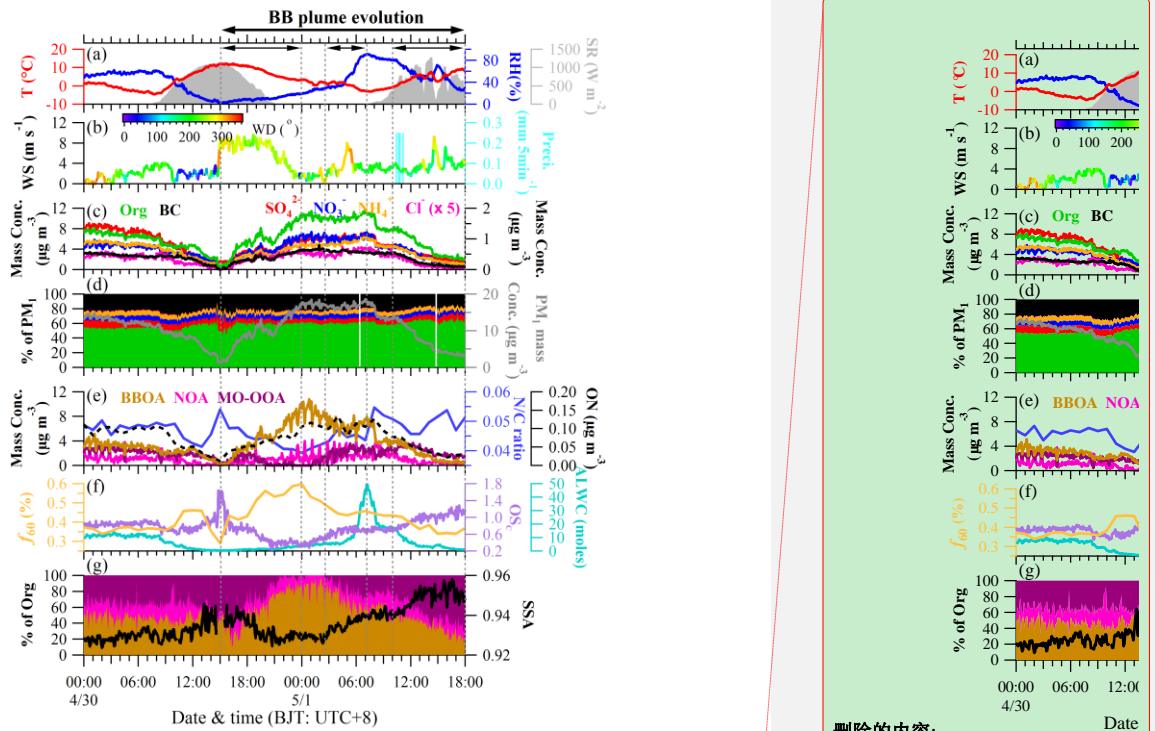
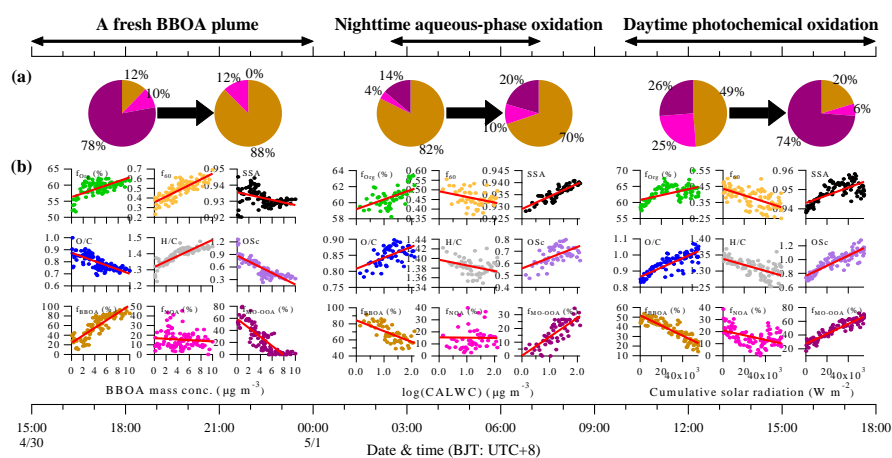


**Figure 12.** The temporal variations of meteorological parameters, mass concentrations and mass contributions of each PM<sub>1</sub> species and OA components as well as the N/C ratio,  $f_{60}$  values, carbon oxidation states (OS), aerosol liquid water content (ALWC) and single scattering albedo (SSA) for the case study period from April 30 at 00:00 to May 1 at 18:00.

删除的内容:

带格式的: 字体: (默认) Times New Roman



1025  
1026  
1027  
1028  
1029  
1030

**Figure 13.** Case study of chemical evolution of BB plume from April 30 at 15:00 to May 1 at 18:00. The periods marked with arrows are three distinct evolution processes. Pie charts in (a) are the mass contributions of three OA factors to total OA during the beginning and end time for each process, respectively. The scattering plots in (b) are the aerosol chemistry parameters as a function of BBOA mass concentration, logarithmic values of cumulative aerosol liquid water content (CALWC), and cumulative solar radiation for the corresponding process.